Density Functional Theory of Ultrafast and Ultra Long-Range Phenomena

Dissertation

zur Erlangung des
Doktorgrades der Naturwissenschaften (Dr. rer. nat.)

der

Naturwissenschaftlichen Fakultät II
Chemie, Physik und Mathematik

der Martin-Luther-Universität
Halle-Wittenberg,

vorgelegt von

Herr Tristan Müller
geb. am 07.08.1991 in Simmern/Hunsrück

Datum der Verteidigung: 02. November 2021

Gutachter: Prof. Dr. Eberhard K. U. Groß, Prof. Dr. Ingrid Mertig,
Prof. Dr. Stefan Blügel

Notation

Symbol	**Meaning**
a	A scalar (normal font)
$\boldsymbol{a}$	A 3-dimensional vector (bold font)
$\underline{\underline{\mathrm{a}}}$	A matrix (double underlined)
$\underline{\underline{\vec{a}}}^{(2)}$	A third rank tensor (vector arrow with an additional (2))
∂_a	Derivative with respect to a, $\partial_a \equiv \frac{\partial}{\partial a}$
$\hat{A}$	A quantum mechanical operator
$\underline{\varphi}\left(\boldsymbol{r}\right)$	A two component spinor, $\underline{\varphi}\left(\boldsymbol{r}\right) = \begin{pmatrix} \varphi^{\uparrow}\left(\boldsymbol{r}\right) \\ \varphi^{\downarrow}\left(\boldsymbol{r}\right) \end{pmatrix}$
$\Theta_{\boldsymbol{a}}$	$\Theta_{\boldsymbol{a}} \equiv \Theta\left(\boldsymbol{a}^2 - k_f^2\right)$, where Θ is the Heaviside step function and k_f is the Fermi wave vector
$\Theta^*_{\boldsymbol{a}}$	$\Theta^*_{\boldsymbol{a}} \equiv \Theta\left(k_f^2 - \boldsymbol{a}^2\right)$, where Θ is the Heaviside step function and k_f is the Fermi wave vector

General

- Throughout this work, all quantities, unless otherwise stated, are given in atomic units (a.u.), i.e. $\hbar = |e| = m_{\mathrm{e}} = 1$. The vacuum speed of light is then equal to the inverse of the fine-structure constant, $c \approx 137$. The Bohr magneton is simply given by $\mu_{\mathrm{B}} = \frac{1}{2c}$.
- We use the CGS system alongside with atomic units for all quantities from electrodynamics. Therefore $\epsilon_0 = \frac{1}{4\pi}, \mu_0 = \frac{4\pi}{c}$.

Abbreviations

ALDA	Adiabatic LDA
ALSDA	Adiabatic LSDA
APW	Augmented plane wave
C	Correlation
CDW	Charge-density wave
DFT	Density functional theory
DOS	Density of states
EMW	Electromagnetic wave
FWHM	Full width at half-maximum
HK	Hohenberg-Kohn
IR	Interstitial region
KS	Kohn-Sham
LDA	Local density approximation
LSDA	Local spin-density approximation
MDI	Magnetic dipole interaction
ML	Monolayer
MOKE	Magneto-optic Kerr effect
MSHG	Magnetic second harmonic generation
MT	Muffin-tin
RG	Runge-Gross
SC	Supercell
SDFT	Spin-DFT
SDW	Spin-density wave
SOC	Spin-orbit coupling
TDDFT	Time-dependent DFT
TDSDFT	Time-dependent SDFT
UC	Ultracell
UFD	Ultrafast demagnetization
ULR	Ultra long-range
X	Exchange
XC	Exchange-correlation

Contents

1 Introduction **1**

2 Many-electron systems **3**
- 2.1 The many-body problem . . . 3
- 2.2 Density functional theory . . . 6
  - 2.2.1 The Hohenberg-Kohn Theorem . . . 6
  - 2.2.2 The Kohn-Sham equations . . . 7
  - 2.2.3 Extensions of DFT . . . 10
  - 2.2.4 Approximate functionals . . . 12
- 2.3 Time-dependent density functional theory . . . 15
  - 2.3.1 Fundamental Theorems . . . 15
  - 2.3.2 Time-dependent Kohn-Sham equations . . . 17
  - 2.3.3 Extensions to TDDFT . . . 17
  - 2.3.4 Time-dependent functionals . . . 18
- 2.4 Relativistic effects . . . 19
- 2.5 Numerical implementation . . . 21

3 Ultrafast demagnetization **25**
- 3.1 First observation and suggested explanations . . . 25
- 3.2 Ultrafast magneto-optics . . . 26
  - 3.2.1 Ultrashort laser pulses . . . 26
  - 3.2.2 Laser pulses in magnetic materials - The Faraday effect . . . 30
  - 3.2.3 Reflection from surfaces - The magneto-optic Kerr effect . . . 32
  - 3.2.4 Magnetic second harmonic generation . . . 33
- 3.3 Ab-initio treatment of ultrafast demagnetization . . . 34
  - 3.3.1 Time-dependent Kohn-Sham system . . . 35
  - 3.3.2 Spin-orbit coupling for radial potentials . . . 36
  - 3.3.3 Classical vector potential and the dipole approximation . . . 36
  - 3.3.4 The time propagation . . . 38
- 3.4 Spin flips versus spin transport in optically excited transition metals . 39
- 3.5 Competing spin transfer and dissipation at Co/Cu(001) interfaces . . 43

4 Density functional theory for ultra long-range phenomena 51
4.1 The magnetic dipole interaction and magnetic domains 52
4.2 Ultra long-range ansatz 54
  4.2.1 Wave function and densities 54
  4.2.2 Ultra long-range Hamiltonian 57
  4.2.3 Hamiltonian Matrix Elements 58
4.3 Numerical implementation 60
  4.3.1 Self-consistent solution 60
  4.3.2 Efficient k-space grids 61
  4.3.3 Computation of the Hartree and dipole interaction 62
4.4 Ultra long-range results 62
  4.4.1 Sawtooth potential in Silicon 63
  4.4.2 “Planck” potential in Lithium 65
  4.4.3 Spin-spirals in γ-Iron 67
  4.4.4 Spin-density wave in Chromium 68
4.5 Time-dependent ultra long-range systems 69
4.6 Limits of the ultra long-range method 71

5 Exchange functional for the magnetic dipole interaction 73
5.1 Exchange energy of the homogeneous electron gas 74
5.2 Perturbative exchange functional 76
  5.2.1 Functional form 76
  5.2.2 Second order Goldstone Diagrams 77
  5.2.3 Spin Summation 79
  5.2.4 Symmetric energy diagram 82
  5.2.5 Asymmetric energy diagram 85
  5.2.6 Yin-Yang and frog energy diagrams 87
  5.2.7 Exact numerical and semi-analytical solution 87
5.3 Correlation energy and higher orders 91
5.4 Spin-contact interaction 95

6 Conclusion 99

A Perturbative Energy diagrams 101
A.1 Goldstone diagram evaluation rules 101

1. Introduction

Magnetism is a fascinating and seemingly contradictory phenomenon. While the first recorded observations of magnetism were already made at around 600 BC by Thales of Miletus (the word “Magnet” even means “rock from Magnesia”, a Greek region), a detailed understanding of the origin of magnetism was only achieved in the 20th century - almost two and a half millennia later. The main reason is that, despite being macroscopically measurable, magnetism cannot be explained without invoking quantum mechanics. Even after the advent of quantum mechanics the interest in magnetism did not decrease but, on the contrary, increased even further. Nowadays, magnetism is a highly active field of research and new magnetic shapes and effects are continuously discovered. Besides the fundamental interest, a large driving factor for this is the crucial importance magnetic materials have on key future technologies such as turbines, electric engines and data storage. Stating that, since its first observation, magnetism has never been more technologically relevant than today is not a bold claim.

In this thesis, we are mostly interested in magnetic effects relevant for data storage. A classic example for magnetic data storage are hard disk drives, in which the information is stored via magnetic domains. The magnetization inside a magnetic domain points along a preferred direction, with different directions representing different bits of information. Hard disk drives, however, suffer from being intrinsically slow, as it is necessary to mechanically move the disk and the reading head. This of course raises the question whether different, faster mechanisms exist for reading or writing magnetic memory. A breakthrough discovery was made in the late 1990s [1–3], where it was found that exciting a magnetic material with a laser leads to an ultrafast ($\lesssim 100\,\mathrm{fs}$) reduction of the magnetic moment of the material, suggesting the possibility of ultrafast magnetic devices. However, despite extensive experimental and theoretical research, there is no consensus on the driving mechanism behind ultrafast demagnetization. Another recently suggested idea for faster and denser magnetic memory is racetrack memory [4], where instead of a reading head the magnetic domains themselves are moving, alleviating the problems caused by mechanical parts. Unfortunately, theoretical insight into magnetic domains is limited, as they are very large and can extend up to the low micron regime. This makes a full quantum mechanical treatment computationally impossible and one has to resort to semi-classical approaches, such as the Landau-Lifshitz-Gilbert equation[5].

In this work, we aim at achieving both, a better microscopic understanding of ultrafast demagnetization as well as developing a theoretical method for tackling large-scale quantum systems, such as magnetic domains. This work is organized as follows: In chapter 2 we give a detailed introduction into density-functional theory and its extensions. Furthermore we will introduce the relevant relativistic effects and the basics of the numerical implementation we use. We study ultrafast demagnetization in chapter 3. We will revisit previously suggested explanations for ultrafast demagnetization and discuss common techniques for measuring ultrafast magnetic signals. We will then proceed with presenting our time-dependent density functional theory approach, which is based on the work by Krieger [6]. In two joint experimental-theoretical studies we are able to unravel the most important microscopic contributions to ultrafast demagnetization at early times ($t < 100\,\mathrm{fs}$). In our first study, we manage to explain the different temporal behavior in the demagnetization of bulk Ni and Co and attribute it to intrinsically different spin-orbit coupling time scales. In our second study we consider a Co/Cu(001) interface and are able to distinguish all relevant microscopic processes. We obtain the best quantitative agreement between experiment and theory reported so far. In chapter 4 we introduce a novel numerical technique that will allow us to apply density functional theory to ultra long-range phenomena. Our approach relies on a length-scale separation in reciprocal space, based on which we derive a set of generalized, long-ranged Kohn-Sham equations. This enables us to compute large, extended systems involving thousands of atoms efficiently. We also explicitly include the magnetic dipole interaction in our approach as it is expected to be essential for the formation of magnetic domains. Finally, in chapter 5, we derive an exchange functional for the magnetic dipole interaction to be used with the system presented in ch. 4. This functional will aid in the ab-initio calculation of large-scale magnetic structures.

2. Many-electron systems

We will start off with introducing the basic formalism which is used to describe systems of many interacting particles. We will show that such systems are extremely difficult to compute with a direct approach. Density functional theory and its extensions are a computationally feasible, formally exact method for treating such systems. We will outline some elementary concepts of density functional theory. This chapter is partially based on the book by Engel and Dreizler [7].

2.1 The many-body problem

The most used equation when describing atoms, molecules and solids is the Schrödinger equation. The Schrödinger equation is a non-relativistic equation of motion for treating systems of electrons and nuclei. The Schrödinger equation for the coupled electron-nucleus system reads

$$i\partial_t \left|\Psi\left(t\right)\right\rangle = \hat{H} \left|\Psi\left(t\right)\right\rangle \tag{2.1}$$

where $\left|\Psi\left(t\right)\right\rangle$ is the quantum mechanical state of the system and $\hat{H}$ is the Hamiltonian given by

$$\hat{H} = \hat{T}_n + \hat{T}_e + \hat{W}_{n-n} + \hat{W}_{e-e} + \hat{W}_{e-n} + \hat{V}_{n-ext} + \hat{V}_{e-ext} \tag{2.2}$$

$\hat{T}_n, \hat{T}_e$ are the kinetic energy operators for the nuclei and the electrons and are given by:

$$\hat{T}_n = \sum_\alpha \frac{\left(-i\nabla_\alpha\right)^2}{2M_\alpha}, \quad \hat{T}_e = \sum_j \frac{\left(-i\nabla_j\right)^2}{2}, \tag{2.3}$$

where ∇_α acts on the Cartesian coordinates $\boldsymbol{R}_\alpha$ of nucleus α which has the mass M_α. Similarly, ∇_i acts on the coordinate $\boldsymbol{r}_j$ of electron j.

The electrostatic interactions between particles are represented by $\hat{W}_{n-n}$, $\hat{W}_{e-e}$, $\hat{W}_{e-n}$ corresponding to a repulsive nuclei-nuclei interaction, a repulsive electron-electron interaction and an attractive electron-nuclei interaction:

$$\hat{W}_{n-n} = \sum_{\alpha<\beta} \frac{Z_\alpha Z_\beta}{\left|\boldsymbol{R}_\alpha - \boldsymbol{R}_\beta\right|}, \hat{W}_{e-e} = \sum_{j<j'} \frac{1}{\left|\boldsymbol{r}_j - \boldsymbol{r}_{j'}\right|}, \hat{W}_{n-e} = -\sum_{\alpha,j} \frac{Z_\alpha}{\left|\boldsymbol{R}_\alpha - \boldsymbol{r}_j\right|} \tag{2.4}$$

Finally, both electrons and nuclei may couple to an external, electromagnetic field:

$$\hat{V}_{\text{n}-\text{ext}} = \sum_{\alpha} \Big[Z_\alpha \Phi_{\text{ext}}\left(\boldsymbol{R}_\alpha, t\right) + i\frac{Z_\alpha}{M_\alpha c}\boldsymbol{A}_{\text{ext}}\left(\boldsymbol{R}_\alpha, t\right)\cdot\nabla_\alpha + \frac{Z_\alpha^2}{2c^2}A^2_{\text{ext}}\left(\boldsymbol{R}_\alpha, t\right) - \boldsymbol{I}_\alpha \cdot \boldsymbol{B}_{\text{ext}}\left(\boldsymbol{R}_\alpha, t\right)\Big] \tag{2.5}$$

$$\hat{V}_{\text{e}-\text{ext}} = \sum_{j} \big[-\Phi_{\text{ext}}\left(\boldsymbol{r}_j, t\right) - 2i\mu_{\text{B}}\boldsymbol{A}_{\text{ext}}\left(\boldsymbol{r}_j, t\right)\cdot\nabla_j + 2\mu_{\text{B}}^2 A^2_{\text{ext}}\left(\boldsymbol{r}_j, t\right) + \mu_{\text{B}}\boldsymbol{\sigma}_j \cdot \boldsymbol{B}_{\text{ext}}\left(\boldsymbol{r}_j, t\right)\big] \tag{2.6}$$

Here, $\Phi_{\text{ext}}, \boldsymbol{A}_{\text{ext}}$ are a scalar and a vector potential corresponding to the electromagnetic fields

$$\boldsymbol{E}_{\text{ext}} = -\nabla\Phi_{\text{ext}}\left(\boldsymbol{r}, t\right) - \frac{1}{c}\partial_t \boldsymbol{A}_{\text{ext}}\left(\boldsymbol{r}, t\right) \tag{2.7}$$

$$\boldsymbol{B}_{\text{ext}}\left(\boldsymbol{r}, t\right) = \nabla \times \boldsymbol{A}_{\text{ext}}\left(\boldsymbol{r}, t\right) \tag{2.8}$$

$\boldsymbol{I}_\alpha$ is the magnetic moment of nucleus α, μ_{B} is the Bohr magneton and $\boldsymbol{\sigma}_i$ is a vector of Pauli matrices.

The simplest case consists of a single atom without any external field. In such a system, one can make a transformation into the center-of-mass frame and obtain decoupled equations of motion for the motion of the whole atom and the motion of individual electrons around the nucleus. Due to the nucleus being much heavier than the electrons, the center-of-mass essentially coincides with the nuclear position. It is therefore sufficient to solve a purely electronic problem where the nucleus enters as a static external field.

If the system, however, involves multiple atoms, this decoupling is no longer possible. It then becomes necessary to treat the coupled electron-nuclei system:

$$\begin{aligned} &i\partial_t \Psi_a\left(\boldsymbol{R}_1 I_1, \ldots, \boldsymbol{R}_K I_K; \boldsymbol{r}_1 s_1, \ldots, \boldsymbol{r}_N s_N; t\right) \\ &\quad = \hat{H}\Psi_a\left(\boldsymbol{R}_1 I_1, \ldots, \boldsymbol{R}_K I_K; \boldsymbol{r}_1 s_1, \ldots, \boldsymbol{r}_N s_N; t\right) \end{aligned} \tag{2.9}$$

where I_i, s_i denote the spin-degree of freedom of nucleus/electron i. In the absence of explicitly time-dependent external fields, a single phase factor accounts for the time-dependence, i.e.

$$\Psi_a\left(t\right) = \Psi_a e^{iE_a t}, \tag{2.10}$$

solves the time-dependent Schrödinger equation (eq. 2.1), provided that the initial state for the time-propagation is an eigenstate of the stationary Schrödinger equation:

$$\begin{aligned} &\hat{H}\Psi_a\left(\boldsymbol{R}_1 I_1, \ldots, \boldsymbol{R}_K I_K; \boldsymbol{r}_1 s_1, \ldots, \boldsymbol{r}_N s_N\right) \\ &\quad = E_a\Psi_a\left(\boldsymbol{R}_1 I_1, \ldots, \boldsymbol{R}_K I_K; \boldsymbol{r}_1 s_1, \ldots, \boldsymbol{r}_N s_N\right) \end{aligned} \tag{2.11}$$

Even solving only the stationary Schrödinger equation is exceedingly hard and not computationally possible for most relevant applications. A common first step when tackling this problem is a partial decoupling of the electrons from the nuclear motion. This is achieved by the "Born-Oppenheimer approximation", which employs the fact that the electrons are much lighter than the nuclei. The resulting assumption is that the nuclei are stationary during typical electronic processes. We can then factorize the wave function:

$$\begin{aligned}&\Psi_{a\equiv ik}\left(\boldsymbol{R}_1 I_1,\ldots,\boldsymbol{R}_K I_K;\boldsymbol{r}_1 s_1,\ldots,\boldsymbol{r}_n s_n\right)\\&\quad=\Psi^n_{ik}\left(\boldsymbol{R}_1 I_1,\ldots,\boldsymbol{R}_K I_K\right)\Psi^e_k\left(\boldsymbol{R}_1 I_1,\ldots,\boldsymbol{R}_K I_K;\boldsymbol{r}_1 s_1,\ldots,\boldsymbol{r}_N s_N\right)\end{aligned}\tag{2.12}$$

The electronic wave function now depends parametrically on the the position of the nuclei. It satisfies the Schrödinger equation

$$\begin{aligned}&\hat{H}_e\Psi^e_k\left(\boldsymbol{R}_1 I_1,\ldots,\boldsymbol{R}_K I_K;\boldsymbol{r}_1 s_1,\ldots,\boldsymbol{r}_N s_N\right)\\&\quad=E_k\left(\boldsymbol{R}_1 I_1,\ldots,\boldsymbol{R}_K I_K\right)\Psi^e_k\left(\boldsymbol{R}_1 I_1,\ldots,\boldsymbol{R}_K I_K;\boldsymbol{r}_1 s_1,\ldots,\boldsymbol{r}_N s_N\right)\end{aligned}\tag{2.13}$$

with the electronic Hamiltonian:

$$\hat{H}_e=\hat{T}_e+\hat{W}_{e-e}+\hat{V}_{ext}\tag{2.14}$$

where we have "absorbed" the electron-nuclear interaction $\hat{W}_{n-e}$ in the external potential $\hat{V}_{\text{ext}}\left(\boldsymbol{R}_1 I_1\ldots,\boldsymbol{R}_K I_K\right)$. This is a stationary eigenvalue problem for any set of nuclear coordinates $\boldsymbol{R}_\alpha$. The eigenvalues $E_k\left(\boldsymbol{R}_1 I_1,\ldots,\boldsymbol{R}_K I_K\right)$ together with $\hat{V}_{n-n}$ (eq. 2.4) in turn act as potentials in which the nuclei are moving. We will assume for the remainder of this thesis that the nuclear positions are known, either by a previous energy minimization or from experimental values. We emphasize that this is by no means a trivial step and generally very computationally demanding. However, the systems treated in this thesis are relatively simple solids which are known to exist and to be stable. In this case, we can drop the nuclear coordinates:

$$\hat{H}_e\Psi^e_k\left(\boldsymbol{r}_1 s_1,\ldots,\boldsymbol{r}_N s_N\right)=E_k\Psi^e_k\left(\boldsymbol{r}_1 s_1,\ldots,\boldsymbol{r}_N s_N\right)\tag{2.15}$$

or, if the external potential $\hat{V}_{ext}$ is explicitly time-dependent:

$$i\partial_t\Psi^e_k\left(\boldsymbol{r}_1 s_1,\ldots,\boldsymbol{r}_N s_N;t\right)=\hat{H}_e\Psi^e_k\left(\boldsymbol{r}_1 s_1,\ldots,\boldsymbol{r}_N s_N;t\right)\tag{2.16}$$

Solving eqs. 2.15, 2.16 remains a formidable task. Storing the wave function Ψ requires storing the probability density in all space for every particle. While doing so is feasible for a small number of particles, the required memory to store the wave function increases exponentially with the number of particles. Solving the Schrödinger equation with the full wave function equation for solids, molecules or even for atoms of moderate size is currently impossible. While approximations for the wave function of a given system exist, such as Hartree-Fock, we will take a different route for solving eqs. 2.15, 2.16 by making use of density functional theory.

2.2 Density functional theory

The main origin of the complexity of eq. 2.15 is the electron-electron interaction $\hat{W}_{e-e}$, which leads to a mixture of electronic states and thus subsequently to the exponential wall encountered in computations. A major realization was made in 1964 by Hohenberg and Kohn [8]. They proved that all observables of an interacting non-degenerate many-body electron state can be derived from the electronic ground-state density alone. Together with the proof that the electronic density can be derived without knowledge of the electronic wave function, this became later known as the Hohenberg-Kohn theorem. It is remarkable because knowledge of the full electronic wave function is no longer mandatory to describe a system, thus reducing the necessary degrees of freedom considerably. The Hohenberg-Kohn theorem is the foundation of **d**ensity **f**unctional **t**heory (DFT). For all following considerations, we consider the purely electronic Hamiltonian

$$\hat{H} = \hat{T} + \hat{W} + \hat{V}_{\text{ext}}. \tag{2.17}$$

Here $\hat{V}_{\text{ext}}$ is now any external electrostatic potential (e.g. the potential of fixed nuclei).

2.2.1 The Hohenberg-Kohn Theorem

In their seminal paper Hohenberg and Kohn proved that it is sufficient to describe a many-electron system solely through the electronic ground state density [8], which for any quantum state $|\Psi\rangle$ is given by:

$$n_0(\boldsymbol{r}) = \langle\Psi|\,\hat{n}(\boldsymbol{r})\,|\Psi\rangle\,, \quad \hat{n}(\boldsymbol{r}) = \sum_{i=1}^{N}\delta(\boldsymbol{r}-\boldsymbol{r}_i)\,. \tag{2.18}$$

It is easy to see that the electronic density is determined by the external potential:

$$v_{\text{ext}}(\boldsymbol{r}) \xrightarrow{(2.15)} |\Psi\rangle \xrightarrow{(2.18)} n_0(\boldsymbol{r})\,. \tag{2.19}$$

The proof by Hohenberg and Kohn now shows that this map is invertible, up to a constant, for non-degenerate ground states:

$$v_{\text{ext}}(\boldsymbol{r}) \xleftrightarrow{\text{HK}} n_0(\boldsymbol{r})\,. \tag{2.20}$$

This proof was later shown to hold even for degenerate ground states [9]. A direct consequence is that, in principle, every external potential can be written as a functional of the ground state density, i.e. $v_{\text{ext}}[n](\boldsymbol{r})$. With the Schrödinger equation (eq. 2.15) follows then that the ground state wave function (for non-degenerate systems) is also a functional of the electron density, i.e. $|\Psi_0[n_0]\rangle$. It thus follows that every observable of a non-degenerate, many-electron system can, in principle, be expressed by the ground state density:

$$\left\langle\hat{O}\right\rangle = \langle\Psi_0[n_0]|\,\hat{O}\,|\Psi_0[n_0]\rangle = O[n_0]\,. \tag{2.21}$$

Specifically, the ground state energy is then also a functional of the electron density (even in the case of degenerate systems):

$$E_0\left[n_0\right] = \langle\Psi_0|\,\hat{T}+\hat{W}+\hat{V}_{\text{ext}}\,|\Psi_0\rangle = T\left[n_0\right]+W\left[n_0\right]+\int \mathrm{d}\boldsymbol{r}\; v_{\text{ext}}\left(\boldsymbol{r}\right) n_0\left(\boldsymbol{r}\right), \quad (2.22)$$

where we defined the kinetic energy functional $T\left[n\right]$ and the electron-electron interaction functional $W\left[n\right]$. By applying the Rayleigh-Ritz variational principle to eq. 2.22, Hohenberg and Kohn managed to show that:

$$E_0\left[n_0\right] < E_0\left[n\right],\ \forall\ n\left(\boldsymbol{r}\right) \neq n_0\left(\boldsymbol{r}\right). \quad (2.23)$$

Thus the ground state density n_0 is that density which minimizes the ground state energy functional $E_0\left[n\right]$ for a given external potential $v_{\text{ext}}\left(\boldsymbol{r}\right)$. It is instructive to rewrite eq. 2.22 as

$$\begin{aligned} &E_0\left[n_0\right] = F_{\text{HK}}\left[n_0\right]+\int \mathrm{d}\boldsymbol{r}\; v_{\text{ext}}\left(\boldsymbol{r}\right) n_0\left(\boldsymbol{r}\right), \quad (2.24)\\ &\text{with } F_{\text{HK}}\left[n_0\right] = T\left[n_0\right]+W\left[n_0\right]. \end{aligned}$$

$F_{\text{HK}}\left[n_0\right]$ is a universal functional, as it is the same functional for any interacting electronic system, be it atoms, molecules or solids. The three concepts of invertibility, variational access and universality are the central statements of the Hohenberg-Kohn(HK) theorem.

It is worth noting that specifying the explicit form of $\hat{W}$ is not necessary for the proof of the HK theorem, it thus holds for any general two-particle interaction. While solving for the density variationally is a formally exact approach to the many-body system, the exact form of $T\left[n\right]$ and $W\left[n\right]$ is unknown and must be approximated. A typical calculation of the ground state density proceeds via the so-called Kohn-Sham equations, which simplify finding a good approximation for $T\left[n\right]$.

2.2.2 The Kohn-Sham equations

The **K**ohn-**S**ham (KS) equations were first introduced in 1965 [9]. They describe an auxiliary system of non-interacting particles which will produce the same ground state density as a corresponding interacting system. The equations are given by

$$\left[-\frac{\nabla^2}{2}+v_s\left(\boldsymbol{r}\right)\right]\varphi_j\left(\boldsymbol{r}\right) = \epsilon_i\varphi_j\left(\boldsymbol{r}\right), \quad n_s\left(\boldsymbol{r}\right) = \sum_{j=1}^{N}\left|\varphi_j\left(\boldsymbol{r}\right)\right|^2, \quad (2.25)$$

where $\varphi_j, j = \{1,\dots,N\}$ are the so-called KS orbitals, with N being the number of electrons. $v_s\left(\boldsymbol{r}\right)$ is the KS potential, an auxiliary single-particle potential which has the property that the corresponding density $n_s\left(\boldsymbol{r}\right)$ matches the ground state density of the interacting system, i.e. $n_s\left(\boldsymbol{r}\right) = n_0\left(\boldsymbol{r}\right)$. As the HK theorem is valid for any general two-particle interaction, the ground state density of the KS system is that density which minimizes the KS energy:

$$E_s\left[n\right] = T_s\left[n\right] + \int \mathrm{d}\boldsymbol{r}\; v_s\left(\boldsymbol{r}\right) n\left(\boldsymbol{r}\right), \tag{2.26}$$

where T_s is the KS kinetic energy which is given by:

$$T_s\left[n\right] = \frac{1}{2}\sum_{i=1}^{N} \int \mathrm{d}\boldsymbol{r}\; \varphi_j^*\left(\boldsymbol{r}\right) \nabla^2 \varphi_j\left(\boldsymbol{r}\right). \tag{2.27}$$

We will use the remainder of this section to sketch the derivation of the form of $v_s\left(\boldsymbol{r}\right)$. For a more in-depth derivation, the reader is referred to the book by Dreizler and Gross [10]. We start by rewriting eq. 2.24 as

$$\begin{aligned} E_0\left[n\right] =& T_s\left[n\right] + \int \mathrm{d}\boldsymbol{r}\; v_{\mathrm{ext}}\left(\boldsymbol{r}\right) n\left(\boldsymbol{r}\right) \\ &+ \frac{1}{2}\int\int \mathrm{d}\boldsymbol{r}\,\mathrm{d}\boldsymbol{r'}\; n\left(\boldsymbol{r}\right) w\left(\boldsymbol{r},\boldsymbol{r'}\right) n\left(\boldsymbol{r'}\right) + E_{\mathrm{xc}}\left[n\right]. \end{aligned} \tag{2.28}$$

$w\left(\boldsymbol{r},\boldsymbol{r'}\right)$ is any two-particle interaction and the exchange-correlation (XC) functional $E_{\mathrm{xc}}\left[n\right]$ is formally defined as

$$E_{\mathrm{xc}}\left[n\right] = F_{\mathrm{HK}}\left[n\right] - \frac{1}{2}\int\int \mathrm{d}\boldsymbol{r}\,\mathrm{d}\boldsymbol{r'}\; n\left(\boldsymbol{r}\right) w\left(\boldsymbol{r},\boldsymbol{r'}\right) n\left(\boldsymbol{r'}\right) - T_s\left[n\right], \tag{2.29}$$

with F_{HK} given by eq. 2.24. Due to the HK variational principle (eq. 2.23), $E_0\left[n\right]$ is stationary around the minimum density $n_0\left(\boldsymbol{r}\right)$. We thus take the functional derivative of eq. 2.28 with respect to $n\left(\boldsymbol{r}\right)$ and find that

$$v_s\left(\boldsymbol{r}\right) = v_{\mathrm{ext}}\left(\boldsymbol{r}\right) + \int \mathrm{d}\boldsymbol{r'}\; w\left(\boldsymbol{r},\boldsymbol{r'}\right) n_0\left(\boldsymbol{r'}\right) + v_{\mathrm{xc}}\left[n_0\right]\left(\boldsymbol{r}\right) \tag{2.30}$$

with the exchange-correlation potential

$$v_{\mathrm{xc}}\left[n_0\right]\left(\boldsymbol{r}\right) = \left.\frac{\delta E_{\mathrm{xc}}\left[n\right]}{\delta n\left(\boldsymbol{r}\right)}\right|_{n_0}. \tag{2.31}$$

For a normal electronic system, w will correspond to the electron-electron repulsion (Hartree interaction v_{H}) and we have:

$$\begin{aligned} v_s\left(\boldsymbol{r}\right) &= v_{\mathrm{ext}}\left(\boldsymbol{r}\right) + \int \mathrm{d}\boldsymbol{r'}\; \frac{n_0\left(\boldsymbol{r'}\right)}{\left|\boldsymbol{r}-\boldsymbol{r'}\right|} + v_{\mathrm{xc}}\left[n_0\right]\left(\boldsymbol{r}\right) & (2.32)\\ &= v_{\mathrm{ext}}\left(\boldsymbol{r}\right) + v_{\mathrm{H}}\left[n_0\right]\left(\boldsymbol{r}\right) + v_{\mathrm{xc}}\left[n_0\right]\left(\boldsymbol{r}\right). & (2.33) \end{aligned}$$

As v_s depends on the ground state density n_0, it is necessary to solve eqs. (2.25), (2.32) self-consistently. Despite this, the KS system is computationally much easier to solve than the original, interacting system, as it no longer is limited by exponential scaling (fig. 2.1). One may raise the question whether there exists for every interacting system a potential v_s which makes it possible to represent it as a non-interacting system. This question of non-interacting v-representability has been addressed previously and turns out not to be a limitation in practice. The reader is again referred to the book by Engel and Dreizler [7] for a more in-depth explanation.

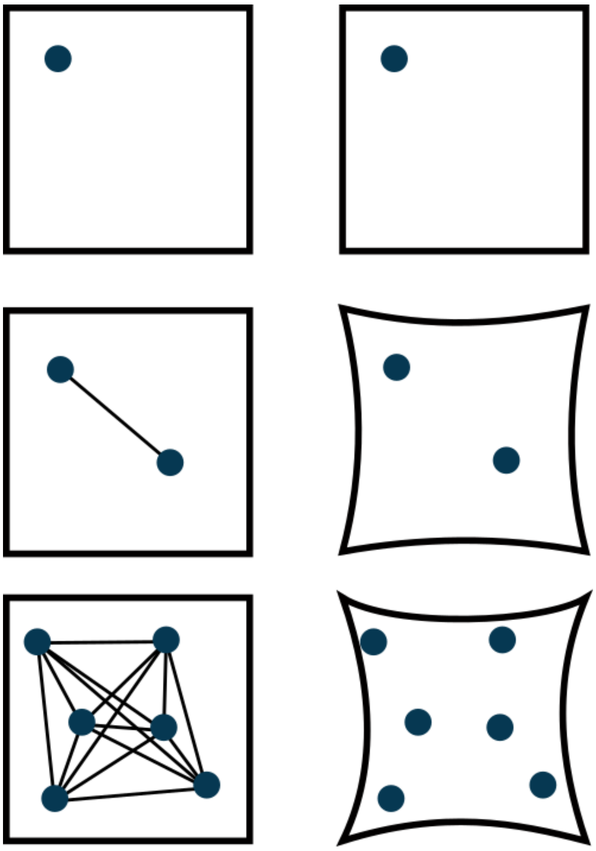

Figure 2.1
Schematic comparison of an interacting, Schrödinger equation approach (left column) and a KS system (right column). In a wave function approach, the complexity grows exponentially, as can be seen by the number of edges. In the KS system, electrons are non-interacting and no edges are present. Although the environment changes ($v_{\mathrm{xc}}\left([n_0]\,;\boldsymbol{r}\right) \neq 0$), this barely increases the computational cost. The KS system is formally exact and reproduces the same density $n\left(\boldsymbol{r}\right)$ as the interacting density.

2.2.3 Extensions of DFT

All of our DFT considerations so far were only concerned with the charge density. While every quantity can be derived from the density alone due to the HK theorem, the functionals to do so are often not known. A standard approach to circumvent this problem is to add extra densities to the KS system, which will then be reproduced exactly alongside the charge density. We showcase two examples of extensions of DFT in this section.

Spin-DFT

A prime example of an added extra density is the magnetization density. The magnetization and spin-based phenomena in general are, due to the functionals being unknown, typically not attainable from the charge density. To circumvent this problem, Barth and Hedin [11] came up with **s**pin-**d**ensity **f**unctional **t**heory (SDFT), where the magnetization is an additional density. The aim is then to find a non-interacting system which reproduces the correct charge and magnetization density of an interacting system, $n_s(\boldsymbol{r}) = n(\boldsymbol{r})\,,\ \boldsymbol{m}_s(\boldsymbol{r}) = \boldsymbol{m}(\boldsymbol{r})$. We extend the Hamiltonian (eq. 2.17) to be:

$$\hat{H} = \hat{T} + \hat{W} + \int \mathrm{d}\boldsymbol{r}\, v_{\text{ext}}(\boldsymbol{r})\, \hat{n}(\boldsymbol{r}) + \frac{1}{2c}\boldsymbol{B}_{\text{ext}}(\boldsymbol{r}) \cdot \hat{\boldsymbol{m}}(\boldsymbol{r})\,. \tag{2.34}$$

Here, $\hat{\boldsymbol{m}}$ is the operator of the magnetization density

$$\hat{\boldsymbol{m}}(\boldsymbol{r}) = \sum_i^N \boldsymbol{\sigma}_i \delta(\boldsymbol{r} - \boldsymbol{r}_i)\,, \quad \boldsymbol{\sigma} = \begin{pmatrix} \sigma_x \\ \sigma_y \\ \sigma_z \end{pmatrix} \tag{2.35}$$

and σ_i are the Pauli matrices. Analogous to the ground state charge density, we can define the ground state magnetization density:

$$\boldsymbol{m}_0 = \langle \Psi_0 | \hat{\boldsymbol{m}}(\boldsymbol{r}) | \Psi_0 \rangle\,. \tag{2.36}$$

It is then possible to derive a one-to-one correspondence similarly to the HK theorem,

$$|\Psi_0\rangle \leftrightarrow (n_0, \boldsymbol{m}_0) \tag{2.37}$$

and consequently, we can define a ground state functional:

$$E[n, \boldsymbol{m}] = F[n, \boldsymbol{m}] + \int \mathrm{d}\boldsymbol{r}\, v_{\text{ext}}(\boldsymbol{r})\, \hat{n}(\boldsymbol{r}) + \boldsymbol{B}_{\text{ext}}(\boldsymbol{r}) \cdot \hat{\boldsymbol{m}}(\boldsymbol{r}) \tag{2.38}$$

$$F[n, \boldsymbol{m}] = \langle \Psi[n, \boldsymbol{m}] | \hat{T} + \hat{W} | \Psi[n, \boldsymbol{m}] \rangle \tag{2.39}$$

with the minimum condition that

$$E[n_0, \boldsymbol{m}_0] < E[n, \boldsymbol{m}] \quad \forall (n, \boldsymbol{m}) \neq (n_0, \boldsymbol{m}_0)\,. \tag{2.40}$$

In this case, a minimization of the energy with respect to the non-interacting orbitals φ will lead to a KS system which is spin-dependent:

$$\left[-\frac{\nabla^2}{2}+v_s\left[n,\boldsymbol{m}\right](\boldsymbol{r})+\frac{1}{2c}\boldsymbol{B}_s\left[n,\boldsymbol{m}\right](\boldsymbol{r})\cdot\boldsymbol{\sigma}\right]\varphi_j\left(\boldsymbol{r},\sigma\right)=\epsilon_i\varphi_j\left(\boldsymbol{r},\sigma\right). \tag{2.41}$$

where

$$v_s\left[n,\boldsymbol{m}\right](\boldsymbol{r})=v_{\text{ext}}(\boldsymbol{r})+v_{\text{H}}\left[n\right](\boldsymbol{r})+\underbrace{\left.\frac{\delta E_{\text{xc}}\left[n,\boldsymbol{m}\right]}{\delta n\left(\boldsymbol{r}\right)}\right|_{\boldsymbol{m}}}_{v_{\text{xc}}[n,\boldsymbol{m}](\boldsymbol{r})} \tag{2.42}$$

$$\boldsymbol{B}_s\left[n,\boldsymbol{m}\right](\boldsymbol{r})=\boldsymbol{B}_{\text{ext}}(\boldsymbol{r})+2c\underbrace{\left.\frac{\delta E_{\text{xc}}\left[n,\boldsymbol{m}\right]}{\delta \boldsymbol{m}\left(\boldsymbol{r}\right)}\right|_{n}}_{\boldsymbol{B}_{\text{xc}}[n,\boldsymbol{m}](\boldsymbol{r})} \tag{2.43}$$

Similar to how $v_{\text{xc}}(\boldsymbol{r})$ represents many-particle exchange and correlation effects acting on the charge density, $\boldsymbol{B}_{\text{xc}}(\boldsymbol{r})$ contains these effects for the magnetization density.

Current-Spin-DFT

As a second example, we will mention that one can further extend the KS equations to also reproduce the exact interacting current density $\boldsymbol{j}$. The formal theory is **c**urrent-**s**pin-**d**ensity **f**unctional **t**heory [12]. The total current in a stationary system is given by:

$$\boldsymbol{j}=\boldsymbol{j}_p+\frac{1}{2}\nabla\times\boldsymbol{m}(\boldsymbol{r})-\frac{1}{c}\boldsymbol{A}_{\text{ext}}(\boldsymbol{r})\,n(\boldsymbol{r}), \tag{2.44}$$

where $\boldsymbol{j}_p$ is the paramagnetic current density, which can be conveniently expressed with the anti-commutator $\{\ldots,\ldots\}$,

$$\hat{\boldsymbol{j}}_p(\boldsymbol{r})=\sum_{i=1}^{N}\frac{1}{2}\left\{\delta\left(\boldsymbol{r}-\boldsymbol{r}_i\right),\hat{\boldsymbol{p}}_i\right\}. \tag{2.45}$$

As can be seen, the second and third term in eq. 2.44 will be correctly reproduced if $n(\boldsymbol{r})$ and $\boldsymbol{m}(\boldsymbol{r})$ are correctly reproduced. Therefore, a current extension of DFT only needs to reproduce the exact paramagnetic current $\boldsymbol{j}_p$, which is achieved by introducing an exchange-correlation vector potential $\boldsymbol{A}_{\text{xc}}$. The full KS equations for $n,\boldsymbol{m},\boldsymbol{j}_p$ are given by

$$\begin{aligned}\Bigg\{\left(-i\nabla+\frac{1}{c}\boldsymbol{A}_{\text{ext}}(\boldsymbol{r})+\boldsymbol{A}_{\text{xc}}(\boldsymbol{r})\right)^2+v_{\text{ext}}(\boldsymbol{r})+v_{\text{H}}(\boldsymbol{r})+v_{\text{xc}}(\boldsymbol{r})&\\ +\frac{1}{2c}\left(\boldsymbol{B}_{\text{ext}}(\boldsymbol{r})+\boldsymbol{B}_{\text{xc}}(\boldsymbol{r})\right)\cdot\boldsymbol{\sigma}\Bigg\}\epsilon_i\varphi_j\left(\boldsymbol{r},\sigma\right)=\epsilon_i\varphi_j\left(\boldsymbol{r},\sigma\right).&\end{aligned} \tag{2.46}$$

Analogous to the previous DFT extensions, we have

$$\begin{aligned} v_{\mathrm{xc}}(\boldsymbol{r}) &= \left.\frac{\delta E_{\mathrm{xc}}[n,\boldsymbol{j}_p,\boldsymbol{m}]}{\delta n(\boldsymbol{r})}\right|_{\boldsymbol{j}_p,\boldsymbol{m}} \\ \boldsymbol{A}_{\mathrm{xc}}(\boldsymbol{r}) &= c\left.\frac{\delta E_{\mathrm{xc}}[n,\boldsymbol{j}_p,\boldsymbol{m}]}{\delta \boldsymbol{j}_p(\boldsymbol{r})}\right|_{n,\boldsymbol{m}} \\ \boldsymbol{B}_{\mathrm{xc}}(\boldsymbol{r}) &= 2c\left.\frac{\delta E_{\mathrm{xc}}[n,\boldsymbol{j}_p,\boldsymbol{m}]}{\delta \boldsymbol{m}(\boldsymbol{r})}\right|_{n,\boldsymbol{j}_p}. \end{aligned} \tag{2.47}$$

Current-Spin-DFT in this form has not been used much, mostly due to the lack of good approximations for $\boldsymbol{A}_{\mathrm{xc}}(\boldsymbol{r})$. A proposed functional by Vignale and Kohn [13] was found to yield mixed results, performing reasonably well for optical properties of metals [14] but very badly for semiconductors [15]. Often it is simply assumed that $\boldsymbol{A}_{\mathrm{xc}}(\boldsymbol{r}) = 0$.

2.2.4 Approximate functionals

Charge density-dependent functionals

A central quantity in all our considerations up to this point is the XC energy functional $E_{\mathrm{xc}}[n]$, which represents quantum many-body effects. As we have already mentioned, the XC-functional needs to be approximated. The oldest approximation is the **l**ocal-**d**ensity **a**pproximation (LDA) [8]. As the name suggests, the LDA only depends on the density locally:

$$E_{\mathrm{xc}}^{\mathrm{LDA}}[n] = \int d^3r\, e_{\mathrm{xc}}^{\mathrm{hom}}(n(\boldsymbol{r})), \tag{2.48}$$

where $e_{\mathrm{xc}}^{\mathrm{hom}}(\boldsymbol{r})$ is the XC-energy density of the homogeneous electron gas. This is justified because the definition of $E_{\mathrm{xc}}[n]$ (eq. (2.29)) is universal, i.e. it does not depend on any external potential, a general E_{xc} can therefore be derived from any electronic system. While the exchange (X) contribution is known analytically, the correlation (C) has to be approximated. Commonly in use is a parametrization of the correlation energy [16] based on a Monte-Carlo simulation of the homogeneous electron gas [17]. The correlation energy as a function of the density is shown in fig. 2.2. Despite its simple form, LDA performs surprisingly well for various systems.

We will briefly state that developing better functionals has been ongoing research throughout the years. A common goal is to also account for non-local effects in E_{xc}. The generalized gradient approximation (GGA) therefore also includes the first order gradient of the density, $E_{\mathrm{xc}}^{\mathrm{GGA}}[n,\nabla n]$ [18]. Meta-GGA includes an additional second-order gradient in the KS-orbitals, $E_{\mathrm{xc}}^{\mathrm{mGGA}}[n,\nabla n,\nabla^2\varphi]$. Parametrizations exist for both approximations [18, 19] and both approximations generally perform better than LDA.

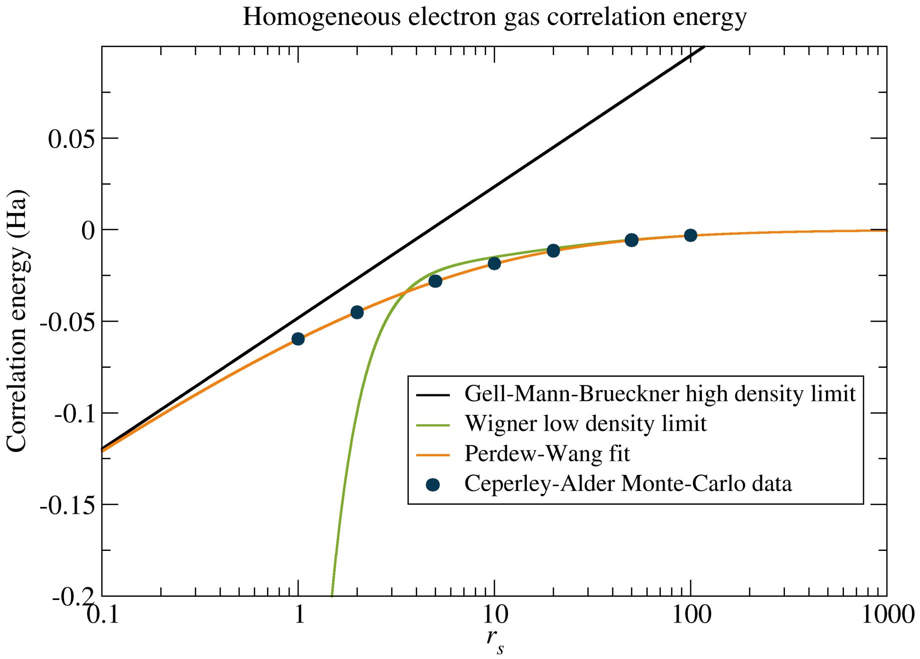

Figure 2.2
The correlation energy of the homogeneous electron gas as a function of the Wigner-Seitz radius r_s. r_s is the radius corresponding to the average spherical volume per electron in the system. The Perdew-Wang fit [16] matches the Monte-Carlo data by Ceperley-Alder [17] and interpolates smoothly between the Gell-Mann-Brueckner high density [20] and the Wigner low density limit [21].

Charge- and spin-dependent functionals

We will now focus on how to extend charge-dependent functionals to incorporate spin-dependence as well. As can be seen from eq. 2.38, such a functional would need to depend on $n(\boldsymbol{r})$ and $\boldsymbol{m}(\boldsymbol{r})$. The simplest functional within SDFT is the **l**ocal **s**pin-**d**ensity **a**pproximation (LSDA), a spin-dependent version of the LDA, which we will derive in the following. A helpful quantity in SDFT is the spin-density matrix, which is given by:

$$\begin{aligned}\underline{\underline{\rho}}(\boldsymbol{r}) &= \frac{1}{2}\left(n(\boldsymbol{r})\,\underline{\underline{I_2}} + \boldsymbol{\sigma}\cdot\boldsymbol{m}\right) \\ &= \frac{1}{2}\begin{pmatrix} n(\boldsymbol{r}) + m_z(\boldsymbol{r}) & m_x(\boldsymbol{r}) - i m_y(\boldsymbol{r}) \\ m_x(\boldsymbol{r}) + i m_y(\boldsymbol{r}) & n(\boldsymbol{r}) - m_z(\boldsymbol{r}) \end{pmatrix}. \end{aligned} \tag{2.49}$$

For simplicity, we will start with considering a collinear system, i.e. the magnetization and the magnetic field are parallel to each other ($\boldsymbol{B}_{\text{ext}} \parallel \boldsymbol{m}$) and are aligned with a given axis at every point in space (we choose $\boldsymbol{e}_z$). As a result, $n, m_z \neq 0$ and $m_x, m_y = 0$. $v_{\text{xc}}(\boldsymbol{r})$ and $B^z_{\text{xc}}(\boldsymbol{r})$ are therefore the only finite XC fields in the system. Because $B^z_{\text{xc}}(\boldsymbol{r})$ couples only to $\underline{\underline{\sigma_z}}$ this results in two decoupled equations for the spin-up and spin-down components with a different local potential,

$$v_{\text{xc},\uparrow}(\boldsymbol{r}) = v_{\text{xc}}(\boldsymbol{r}) + \frac{1}{2c}B^z_{\text{xc}}(\boldsymbol{r}), \quad v_{\text{xc},\downarrow}(\boldsymbol{r}) = v_{\text{xc}}(\boldsymbol{r}) - \frac{1}{2c}B^z_{\text{xc}}(\boldsymbol{r}). \tag{2.50}$$

The spin-density matrix (eq. 2.49) is diagonal in this case and the diagonal elements are typically represented as

$$n_\uparrow(\boldsymbol{r}) = \frac{1}{2}\left(n(\boldsymbol{r}) + m_z(\boldsymbol{r})\right), \quad n_\downarrow(\boldsymbol{r}) = \frac{1}{2}\left(n(\boldsymbol{r}) - m_z(\boldsymbol{r})\right). \tag{2.51}$$

Physically, $n_\uparrow, n_\downarrow$ correspond to the charge density of only spin-up and only spin-down electrons, respectively. We can thus also express the XC energy for collinear systems with $n_\uparrow, n_\downarrow$:

$$E^{\text{LSDA}}_{\text{xc}}[n_\uparrow, n_\downarrow] = \int d^3r\, e^{\text{hom}}_{\text{xc}}\left(n_\uparrow(\boldsymbol{r}), n_\downarrow(\boldsymbol{r})\right), \tag{2.52}$$

where $e^{\text{hom}}_{\text{xc}}\left(n_\uparrow(\boldsymbol{r}), n_\downarrow(\boldsymbol{r})\right)$ is now the XC-energy density of the spin-polarized homogeneous electron gas. Similarly to the LDA, the exchange part is known exactly. The correlation part has been generalized to spin-dependent systems based on analytical spin-scaling considerations [22] and was later found to match Monte Carlo simulations [23].

The corresponding XC-potential can be obtained via

$$v^{\text{LSDA}}_{\text{xc,s}}[n_\uparrow, n_\downarrow](\boldsymbol{r}) = \frac{\delta E^{\text{LSDA}}_{\text{xc}}}{\delta n_s(\boldsymbol{r})} = \left.\frac{\partial e^{\text{hom}}_{\text{xc}}(\tilde{n}_\uparrow, \tilde{n}_\downarrow)}{\partial \tilde{n}_s}\right|_{\tilde{n}_s = n_s(\boldsymbol{r})}, \; s = \{\uparrow, \downarrow\}. \tag{2.53}$$

We limited our discussions to collinear systems up to this point. In non-collinear systems the spin-density matrix (eq. 2.49) is no longer diagonal and it is not sufficient to describe the system only by $n_\uparrow, n_\downarrow$. A simple way to extend the present LSDA to non-collinear systems is to treat every point in space as locally collinear [24]. In practice, one then has to rotate the spin-density matrix (eq. 2.49) at every point in space with a unitary transformation such that it becomes locally diagonal

$$\underline{\underline{\tilde{\rho}}}(\boldsymbol{r}) = \underline{\underline{U}}(\boldsymbol{r})\, \underline{\underline{\rho}}(\boldsymbol{r})\, \underline{\underline{U}}^\dagger(\boldsymbol{r}) = \begin{pmatrix} \tilde{n}^\uparrow(\boldsymbol{r}) & 0 \\ 0 & \tilde{n}^\downarrow(\boldsymbol{r}) \end{pmatrix}. \tag{2.54}$$

We can then apply eq. 2.53 on the diagonal and perform the inverse rotation,

$$\underline{\underline{v_{\mathrm{xc}}}}[n, \boldsymbol{m}](\boldsymbol{r}) = \underline{\underline{U}}^\dagger \begin{pmatrix} v^{\mathrm{LSDA}}_{\mathrm{xc},\uparrow}[\tilde{n}_\uparrow, \tilde{n}_\downarrow](\boldsymbol{r}) & 0 \\ 0 & v^{\mathrm{LSDA}}_{\mathrm{xc},\downarrow}[\tilde{n}_\uparrow, \tilde{n}_\downarrow](\boldsymbol{r}) \end{pmatrix} \underline{\underline{U}}. \tag{2.55}$$

By working out $\underline{\underline{U}}(\boldsymbol{r})$ it is possible to show that the matrix $\underline{\underline{v_{\mathrm{xc}}}}$ can be separated into a scalar XC-potential $v_{\mathrm{xc}}(\boldsymbol{r})$ and a magnetic XC-field $\boldsymbol{B}_{\mathrm{xc}}(\boldsymbol{r})$,

$$\begin{aligned} v^{\mathrm{LSDA}}_{\mathrm{xc}}[n, \boldsymbol{m}](\boldsymbol{r}) &= \frac{1}{2}\left(v^{\mathrm{LSDA}}_{\mathrm{xc},\uparrow}[\tilde{n}_\uparrow, \tilde{n}_\downarrow](\boldsymbol{r}) + v^{\mathrm{LSDA}}_{\mathrm{xc},\downarrow}[\tilde{n}_\uparrow, \tilde{n}_\downarrow](\boldsymbol{r})\right), \\ \boldsymbol{B}^{\mathrm{LSDA}}_{\mathrm{xc}}[n, \boldsymbol{m}](\boldsymbol{r}) &= c\left(v^{\mathrm{LSDA}}_{\mathrm{xc},\uparrow}[\tilde{n}_\uparrow, \tilde{n}_\downarrow](\boldsymbol{r}) - v^{\mathrm{LSDA}}_{\mathrm{xc},\downarrow}[\tilde{n}_\uparrow, \tilde{n}_\downarrow](\boldsymbol{r})\right)\frac{\boldsymbol{m}(\boldsymbol{r})}{|\boldsymbol{m}(\boldsymbol{r})|}. \end{aligned} \tag{2.56}$$

This is the form in which the non-collinear LSDA is typically presented and which is employed in calculations throughout this thesis.

2.3 Time-dependent density functional theory

When treating explicitly time-dependent effects like time-dependent currents or fast magnetization switching, we have to use the time-dependent version of the Schrödinger equation (eq. 2.16). In analogy to the static case, we first consider an electronic Hamiltonian with a now explicitly time-dependent external electrostatic potential

$$\hat{H} = \hat{T} + \hat{W} + \hat{V}_{\mathrm{ext}}(t). \tag{2.57}$$

Solving for the wave function via eq. 2.16 is again a hopeless endeavor for more than a few particles. The HK theorem, however, is only valid for static, time-independent phenomena, i.e. $V_{\mathrm{ext}}(\boldsymbol{r}, t) = V_{\mathrm{ext}}(\boldsymbol{r})$. The derivations based on the HK theorem are not sufficient for time-dependent systems. We will therefore, in this section, focus on how to treat explicitly time-dependent systems. This section is partially based on the textbook by Carsten Ullrich [25].

2.3.1 Fundamental Theorems

Runge-Gross Theorem

In 1984 Runge and Gross formulated what is nowadays known as the Runge-Gross (RG) theorem [26]. The RG theorem can be understood as a time-dependent version of the HK theorem. It states that a one-to-one mapping between the time-dependent external potential $v_{\text{ext}}(\boldsymbol{r}, t)$ and the interacting time-dependent electron density $n(\boldsymbol{r}, t) = \langle \Psi(t) | \hat{n}(\boldsymbol{r}) | \Psi(t) \rangle$ exists. Similarly to how the HK theorem is the basis of DFT, the RG theorem is the basis of **t**ime-**d**ependent **d**ensity **f**unctional **t**heory (TDDFT). Runge and Gross managed to prove that two densities $n(\boldsymbol{r}, t)$, $n'(\boldsymbol{r}, t)$ evolving from the same initial state $|\Psi_0\rangle$ under the two potentials $v_{\text{ext}}(\boldsymbol{r}, t)$, $v'_{\text{ext}}(\boldsymbol{r}, t)$ are always different, if the potentials differ by more than a merely time-dependent function,

$$v_{\text{ext}}(\boldsymbol{r}, t) \neq v'_{\text{ext}}(\boldsymbol{r}, t) + c(t) \xrightarrow{RG} n(\boldsymbol{r}, t) \neq n'(\boldsymbol{r}, t) \,. \tag{2.58}$$

From the uniqueness of the map follows in return that the time-dependent density determines the time-dependent potential up to a function which only depends on time. Subsequently, using the time-dependent Schrödinger equation (eq. (2.16)), the time-dependent many-particle state is also determined by the many-body density and the initial state up to a time-dependent phase factor, $|\Psi(t)\rangle = |\Psi[n, \Psi_0](t)\rangle$. Such a time-dependent phase factor does not have any physical meaning, therefore all time-dependent observables can be calculated from the time-dependent density and the initial state:

$$\left\langle \hat{O} \right\rangle(t) = \langle \Psi(t) | \hat{O} | \Psi(t) \rangle = \langle \Psi[n, \Psi_0](t) | \hat{O} | \Psi[n, \Psi_0](t) \rangle = O[n, \Psi_0](t) \,. \tag{2.59}$$

If the system is in its ground state at $t = 0$, it follows from the HK theorem that $|\Psi_0\rangle = |\Psi_0[n_0]\rangle$ meaning that all observables can, in principle, be calculated from the time-dependent density alone.

Van Leeuwen theorem

While the RG theorem guarantees a mapping between the potential $v_{\text{ext}}(\boldsymbol{r}, t)$ and the electron density $n(\boldsymbol{r}, t)$ and thus lays the foundation for TDDFT, it does not prescribe a practical approach to actually calculating the time-dependent, interacting density. It is not a priori obvious that a generalized, time-dependent KS system exists. Such a system would be a system of non-interacting particles which produces the same density as a system of interacting particles, $n_s(\boldsymbol{r}, t) = n(\boldsymbol{r}, t)$ for all t. This "time-dependent v-representability" problem was solved by van Leeuwen in 1999 [27].

Van Leeuwen proved that for any time-dependent system with interaction $\hat{W}$ evolving from an initial state $|\Psi_0\rangle$ under the potential $v(\boldsymbol{r}, t)$ according to eq. 2.16, there exists a system with a different interaction $\hat{W}'$ evolving from a different initial state $|\Psi'_0\rangle$ under a different potential $v'(\boldsymbol{r}, t)$ (still according to eq. 2.16), which has the same time-dependent density for all t, i.e. $n(\boldsymbol{r}, t) = n'(\boldsymbol{r}, t)$. Furthermore, van Leeuwen showed that $v'(\boldsymbol{r}, t)$ is uniquely determined (up to a merely time-dependent function) by the density $n(\boldsymbol{r}, t)$, the initial states $|\Psi_0\rangle, |\Psi'_0\rangle$ and the interactions $\hat{W}, \hat{W}'$. The only restriction is that the initial states must have the same density and time derivative of the density at $t = 0$: This statement is often called van

Leeuwen theorem. For the special case that $\hat{W} = \hat{W}'$ and $|\Psi_0\rangle = |\Psi_0'\rangle$ the theorem states that an unique $v'(\boldsymbol{r}, t)$ exists which yields $n(\boldsymbol{r}, t)$, thus the RG emerges as a special case from the van Leeuwen theorem. Another relevant special case is that of a non-interacting system, $\hat{W}' = 0$. If a non-interacting state $|\Phi_0\rangle$ exists which yields the interacting density and its time derivative, then there exists a unique potential (up to a merely time-dependent function) $v_s(\boldsymbol{r}, t)$ which reproduces the interacting density for all t. This makes a time-dependent KS system possible.

2.3.2 Time-dependent Kohn-Sham equations

The van Leeuwen theorem not only tells that a time-dependent Kohn-Sham system with a single-particle potential $v_s(\boldsymbol{r}, t)$ exists, it also gives away the properties of such a potential: For a given external potential, it is a functional of the interacting ground state $|\Psi_0\rangle$, the non-interacting ground state $|\Phi_0\rangle$ and the electron density n:

$$v_s(\boldsymbol{r}, t) = v_s[\Psi_0, \Phi_0, n](\boldsymbol{r}, t). \tag{2.60}$$

If the system is initially in the ground state, the HK theorem states that $|\Psi_0\rangle$, $|\Phi_0\rangle$ are functionals of the density, therefore the potential will be a functional of the density alone, $v_s[n](\boldsymbol{r}, t)$. The time-dependent KS system is then given by:

$$\partial_t \varphi_j(\boldsymbol{r}, t) = \left[-\frac{\nabla^2}{2} + v_s(\boldsymbol{r}, t)\right] \varphi_j(\boldsymbol{r}, t), \; n_s(\boldsymbol{r}, t) = \sum_{i=1}^{N} |\varphi_j(\boldsymbol{r}, t)|^2. \tag{2.61}$$

This set of equations is similar to the ground state Kohn-Sham equations (eq. 2.25), but the Kohn-Sham orbitals, the single-particle potential and the electron density are now explicitly time-dependent. The time-dependent potential for electrons interacting via the Coulomb interaction is given by:

$$v_s[n](\boldsymbol{r}, t) = v_{\mathrm{ext}}(\boldsymbol{r}, t) + \int \mathrm{d}\boldsymbol{r}' \frac{n(\boldsymbol{r}', t)}{|\boldsymbol{r} - \boldsymbol{r}'|} + v_{\mathrm{xc}}[n](\boldsymbol{r}, t). \tag{2.62}$$

While the Hartree potential depends on the density instantaneously, the time-dependent XC potential is usually memory-dependent. That means that v_{xc} does not depend only on the density at time t but it usually depends on the density at previous times $t' < t$ as well. It is not possible to define the time-dependent v_{xc} via a functional minimization, as the energy is not generally conserved in a time-dependent system. It is, however, possible to define it via the stationary principle of the quantum mechanical action [28]. Analogous to the static XC potential $v_{\mathrm{xc}}[n](\boldsymbol{r})$, the time-dependent version $v_{\mathrm{xc}}|n](\boldsymbol{r}, t)$ is also not know exactly and needs to be approximated.

2.3.3 Extensions to TDDFT

Similarly to the ground state, all time-dependent observables are in principle obtainable from the time-dependent density alone (eq. 2.59). For many important quantities, however, practical functionals are unknown and various extensions to TDDFT incorporating extra densities exist. We will only briefly mention some of them here. Examples include **t**ime-**d**ependent **s**pin **d**ensity **f**unctional **t**heory (TDSDFT) for treating spin-polarized systems [29], where both, an external potential $v_{\text{ext}}\left(\boldsymbol{r},t\right)$ and an external magnetic field $\boldsymbol{B}_{\text{ext}}\left(\boldsymbol{r},t\right)$ are present. A corresponding KS then reproduces the interacting time-dependent densities $\rho\left(\boldsymbol{r},t\right),\boldsymbol{m}\left(\boldsymbol{r},t\right)$. Another extension is **t**ime-**d**ependent **c**urrent **d**ensity **f**unctional **t**heory (TDCDFT), where an external vector potential $\boldsymbol{A}_{\text{ext}}\left(\boldsymbol{r}\right)$ and the current density $\boldsymbol{j}\left(\boldsymbol{r},t\right)$ are the conjugated variables [30]. While a proof of the van-Leeuwen theorem exists for TDCDFT [31], no such proof currently exists for magnetic systems. We will further explore extensions to TDDFT in chapter 3, where we treat magnetic materials subjected to an external laser field with TDDFT.

2.3.4 Time-dependent functionals

Much like the static KS system (eq. 2.25), the time-dependent KS system (eq. 2.61) relies on an XC-potential (eq. 2.62) to guarantee that the time-dependent, non-interacting system reproduces the true densities of the time-dependent interacting system. Finding a good approximation for $v_{\text{xc}}\left(\boldsymbol{r},t\right)$ is therefore essential for an accurate calculation. This time, however, the XC-potential does not only have to absorb the spatial complexity of the interacting system, it has to account for the temporal complexity as well. While the XC potential is a unique functional of the time-dependent density only (assuming the system is originally in its ground state), $v_{\text{xc}}\left[n\right]\left(\boldsymbol{r},t\right)$, it generally depends on the whole history of the density $n\left(\boldsymbol{r},t\right)$, i.e. the XC potential depends on $n\left(\boldsymbol{r},t'\right),t'<t$. The simplest time-dependent approach is treating $v_{\text{xc}}\left[n\right]\left(\boldsymbol{r},t\right)$ adiabatically, i.e. assuming that $v_{\text{xc}}\left[n\right]\left(\boldsymbol{r},t\right)$ evolves infinitesimally slowly in time. Every time t can then be considered as an independent physical system, thus the history dependence vanishes. We can then use the exact ground state XC functional with the instantaneous density as an input at every t,

$$v_{\text{xc}}^{\text{A}}\left[n\right]\left(\boldsymbol{r},t\right)=v_{\text{xc}}^{t=0}\left[\tilde{n}\right]\left(\boldsymbol{r}\right)|_{\tilde{n}(\boldsymbol{r})=n(\boldsymbol{r},t)}\,. \tag{2.63}$$

The exact ground state functional $v_{\text{xc}}^{t=0}\left[\tilde{n}\right]\left(\boldsymbol{r}\right)$, however, is also not known. In the most famous approximation in TDDFT, the LDA is used as the ground state functional, consequently this approximation to $v_{\text{xc}}\left[n\right]\left(\boldsymbol{r},t\right)$ is called **a**diabatic **l**ocal **d**ensity **a**pproximation (ALDA):

$$v_{\text{xc}}^{\text{ALDA}}\left[n\right]\left(\boldsymbol{r},t\right)=v_{\text{xc}}^{\text{LDA}}\left[\tilde{n}\right]\left(\boldsymbol{r}\right)|_{\tilde{n}(\boldsymbol{r})=n(\boldsymbol{r},t)}\,. \tag{2.64}$$

$v_{\text{xc}}\left[n\right]\left(\boldsymbol{r},t\right)$ does not evolve adiabatically when computing real systems, therefore there is always an error introduced when treating the XC potential adiabatically. We emphasize again that this is an additional approximation. Even with the exact spatial functional, non-adiabatic effects would not be captured. Truly non-adiabatic functionals are currently not available. Considering that the ALDA is a very crude approximation, being local in time and space, it performs surprisingly well for excitation energies of finite systems. In solids, unfortunately, ALDA has shown problems when it comes to describing excitation energies [32]. The adiabatic approximation can of course be employed for the extensions of TDDFT as well. For example we can simply formulate an **a**diabatic **l**ocal **s**pin-**d**ensity **a**pproximation (ALSDA) by using the LSDA (eq. 2.56):

$$\begin{aligned} v_{\mathrm{xc}}^{\mathrm{ALSDA}}\left[n,\boldsymbol{m}\right](\boldsymbol{r},t) &= v_{\mathrm{xc}}^{\mathrm{LSDA}}\left[\tilde{n},\tilde{\boldsymbol{m}}\right](\boldsymbol{r})\Bigg|_{\substack{\tilde{n}(\boldsymbol{r})=n(\boldsymbol{r},t)\\ \tilde{\boldsymbol{m}}(\boldsymbol{r})=\boldsymbol{m}(\boldsymbol{r},t)}}, \\ \boldsymbol{B}_{\mathrm{xc}}^{\mathrm{ALSDA}}\left[n,\boldsymbol{m}\right](\boldsymbol{r},t) &= \boldsymbol{B}_{\mathrm{xc}}^{\mathrm{LSDA}}\left[\tilde{n},\tilde{\boldsymbol{m}}\right](\boldsymbol{r})\Bigg|_{\substack{\tilde{n}(\boldsymbol{r})=n(\boldsymbol{r},t)\\ \tilde{\boldsymbol{m}}(\boldsymbol{r})=\boldsymbol{m}(\boldsymbol{r},t)}}, \end{aligned} \tag{2.65}$$

which is also the approximate functional we will employ in chapter 3 when calculating the time-dependent response of magnetic materials to external fields.

2.4 Relativistic effects

As stated before, the Schrödinger equation (eq. 2.15) is a non-relativistic equation and is therefore only valid in the limit of slowly moving electrons. The proper theory for describing relativistic many-electron systems interacting with a photonic field is **q**uantum **e**lectro**d**ynamics (QED). While a **r**elativistic **d**ensity **f**unctional **t**heory (RDFT) has been defined rigorously [33–35], it is not easily employed. The calculation of observables, for example, is much more involved due to the presence of anti-particle states. A further problem is that the central observable is now the four current j^{μ}, consisting of the charge density and the current density. Information about the magnetization cannot be directly accessed via the four current.

When treating systems with relevant relativistic contributions, one thus typically employs a relativistic expansion of QED. The order of terms in this expansion is given by the order of the coefficient $1/c$, with c being the speed of light. This expansion has been evaluated up to the order $1/c^2$ by Itoh [36]. The result is given by:

$$H = \sum_j \left\{ \frac{1}{2}\boldsymbol{p}_j^2 - \frac{1}{8c^2}\boldsymbol{p}_j^4 + \frac{1}{c}\boldsymbol{p}\cdot\boldsymbol{A}_{\text{ext}}\left(\boldsymbol{r}_j\right) + \frac{1}{2c^2}\boldsymbol{A}_{\text{ext}}\left(\boldsymbol{r}_j\right)^2 \right\} \tag{2.66}$$

$$+ \sum_j \left\{ -\Phi_{\text{ext}}\left(\boldsymbol{r}_j\right) + \frac{1}{2c}\boldsymbol{\sigma}_j\cdot\boldsymbol{B}_{\text{ext}} + \frac{1}{4c^2}\boldsymbol{\sigma}_j\cdot\left[\boldsymbol{E}_{\text{ext}}\left(\boldsymbol{r}_j\right)\times\boldsymbol{p}_j\right] + \frac{\pi}{2c^2}\rho_{\text{ext}}\left(\boldsymbol{r}_j\right) \right\} \tag{2.67}$$

$$+ \frac{1}{2}\sum_{j\neq k}\left\{ \frac{1}{\left|\boldsymbol{r}_j-\boldsymbol{r}_k\right|} - \frac{\pi}{c^2}\delta\left(\boldsymbol{r}_j-\boldsymbol{r}_k\right) \right\} \tag{2.68}$$

$$\begin{aligned} &- \frac{1}{8c^2}\sum_{j\neq k}\left\{ \left[\frac{3\left[\boldsymbol{\sigma}_j\cdot\left(\boldsymbol{r}_j-\boldsymbol{r}_k\right)\right]\left[\left(\boldsymbol{r}_j-\boldsymbol{r}_k\right)\cdot\boldsymbol{\sigma}_j\right]}{\left|\boldsymbol{r}_j-\boldsymbol{r}_k\right|^5} - \frac{\boldsymbol{\sigma}_j\cdot\boldsymbol{\sigma}_k}{\left|\boldsymbol{r}_j-\boldsymbol{r}_k\right|^3} \right] \right. \\ &\left. + \frac{8\pi}{3}\delta\left(\boldsymbol{r}_j-\boldsymbol{r}_k\right)\boldsymbol{\sigma}_j\cdot\boldsymbol{\sigma}_k + 2\left[\frac{3\left[\boldsymbol{p}_j\cdot\left(\boldsymbol{r}_j-\boldsymbol{r}_k\right)\right]\left[\left(\boldsymbol{r}_j-\boldsymbol{r}_k\right)\cdot\boldsymbol{p}_j\right]}{\left|\boldsymbol{r}_j-\boldsymbol{r}_k\right|^3} + \frac{\boldsymbol{p}_j\cdot\boldsymbol{p}_k}{\left|\boldsymbol{r}_j-\boldsymbol{r}_k\right|} \right] \right\} \end{aligned} \tag{2.69}$$

$$- \frac{1}{4c^2}\sum_{j\neq k}\left\{ 2\frac{\boldsymbol{\sigma}_j\cdot\left[\left(\boldsymbol{r}_k-\boldsymbol{r}_j\right)\times\boldsymbol{p}_k\right]}{\left|\boldsymbol{r}_j-\boldsymbol{r}_k\right|^3} + \frac{\boldsymbol{\sigma}_j\cdot\left[\left(\boldsymbol{r}_k-\boldsymbol{r}_j\right)\times\boldsymbol{p}_j\right]}{\left|\boldsymbol{r}_j-\boldsymbol{r}_k\right|^3} \right\}. \tag{2.70}$$

In eq. 2.66 are relativistic kinetic energy corrections and the contributions from an external vector potential. Eq. 2.67 comprises the interaction with external fields and consists of an external electrostatic potential, a Zeeman term and a contribution of an external electric field coupling to the spin of an electron via the electron's orbit. The last term in eq. 2.67 is a correction to the interaction with the external potential due to the spread of the charge of the electron and is typically called "Darwin-term". Here $\rho_{\text{ext}}\left(\boldsymbol{r}\right)$ is that external charge density which gives rise to $\Phi_{\text{ext}}\left(\boldsymbol{r}\right)$, thus $\Delta\Phi_{\text{ext}}\left(\boldsymbol{r}\right) = -4\pi\rho_{\text{ext}}\left(\boldsymbol{r}\right)$. Eq. 2.68 is the Coulomb interaction between electrons with an additional correction term. This correction term is related to the Darwin-term in that it describes the overlap with other charges and is therefore often called "two-electron Darwin-term". The terms in eq. 2.69 correspond to the magnetic dipole interaction: The first term is a dipole-dipole interaction due to the electronic spin. The second term guarantees the correct limit for $\boldsymbol{r}\rightarrow\boldsymbol{r'}$ and also exists in classical electrodynamics [37]. The last term is a dipole-dipole interaction due to the orbital magnetization of electrons. Lastly eq. 2.70 includes interactions between electronic spin and electronic motion. The first term is the interaction of an electron's spin with the magnetic field generated by the current from other moving electrons. The second term is an interaction of the spin of an electron with its own motion. This is because a moving electron, in its rest frame, will experience an effective magnetic field.

We can easily see that we can extract the terms forming the gauge-invariant electronic Schrödinger equation eq. 2.15. Out of the additional relativistic corrections to second order the most important contributions for this work are the **s**pin-**o**rbit **c**oupling (SOC) and the **m**agnetic **d**ipole **i**nteraction (MDI). The SOC term

$$H^{\text{SO}} = \frac{1}{4c^2}\sum_j \boldsymbol{\sigma}_j\cdot\left[\boldsymbol{E}_{\text{ext}}\left(\boldsymbol{r}\right)\times\boldsymbol{p}_j\right] = \frac{1}{4c^2}\sum_j \boldsymbol{\sigma}_j\cdot\left[\nabla\Phi_{\text{ext}}\left(\boldsymbol{r}\right)\times i\nabla\right] \tag{2.71}$$

is notable as it is the lowest order term which allows a coupling of an external electric field to the spin of an electron. To second order, the Zeeman term and the SOC are the only terms which couple external fields to the value of a single spin and thus break conservation of spin momentum. It is therefore expected that both terms are crucial for a simulation of ultrafast demagnetization (cf. chapter 3).

The MDI (eq. 2.69) is the quantum mechanical analog to the classical, magnetostatic interaction between two magnetic dipoles. It is noteworthy in that it is the leading order magnetic-magnetic interaction. The orbital contribution to the MDI is typically small and therefore not considered in this work. For the MDI, we are thus left with

$$
\begin{aligned}
H^{\mathrm{DP}} = -\frac{1}{8c^2}\sum_{j\neq k}\Bigg\{&\left[\frac{3\left[\boldsymbol{\sigma}_j\cdot\left(\boldsymbol{r}_j-\boldsymbol{r}_k\right)\right]\left[\left(\boldsymbol{r}_j-\boldsymbol{r}_k\right)\cdot\boldsymbol{\sigma}_j\right]}{r_{jk}^5}-\frac{\boldsymbol{\sigma}_j\cdot\boldsymbol{\sigma}_k}{r_{jk}^3}\right]\\
&+\frac{8\pi}{3}\delta\left(\boldsymbol{r}_j-\boldsymbol{r}_k\right)\boldsymbol{\sigma}_j\cdot\boldsymbol{\sigma}_k\Bigg\}. \qquad (2.72)
\end{aligned}
$$

This interaction will be discussed later in more detail. It can be a source of non-trivial magnetic order.

2.5 Numerical implementation

We use the Elk electronic structure code for all of our calculations. While Elk is a general code that can handle atoms and molecules, it was designed specifically for solids. In this section we will showcase some additional approximations made in the implementation. For more information we refer to the Elk code documentation [38].

Periodic systems

For solids, standard periodic boundary conditions are employed. The central theorem is Bloch's theorem, which we will briefly review in the following. Bloch's theorem states that the eigenstates of a non-interacting Schrödinger equation with a periodic potential $V\left(\boldsymbol{r}+\boldsymbol{R}\right)=V\left(\boldsymbol{r}\right)$ are given by Bloch waves

$$
\varphi_{\boldsymbol{k}}\left(\boldsymbol{r}\right)=\frac{1}{\sqrt{V}}e^{i\boldsymbol{k}\cdot\boldsymbol{r}}u_{\boldsymbol{k}}\left(\boldsymbol{r}\right),\; u_{\boldsymbol{k}}\left(\boldsymbol{r}+\boldsymbol{R}\right)=u_{\boldsymbol{k}}\left(\boldsymbol{r}\right). \qquad (2.73)
$$

Thus the Bloch waves consist of a periodic function with the same periodicity as the potential V multiplied by a plane wave factor. Furthermore, the reciprocal wave vectors $\boldsymbol{k}$ can be restricted to the first Brillouin zone only. This is very important as it allows for a simple representation of eigenstates which extend throughout the whole solid. We can use the Bloch waves (eq. 2.73) to derive a Schrödinger equation (eq. 2.15) for each $\boldsymbol{k}$-vector,

$$
H_{\boldsymbol{k}}u_{\boldsymbol{k}}\left(\boldsymbol{r}\right)=\left[\frac{1}{2}\left(-i\nabla+\boldsymbol{k}\right)^2+V\left(\boldsymbol{r}\right)\right]u_{\boldsymbol{k}}\left(\boldsymbol{r}\right)=\epsilon_{\boldsymbol{k}}u_{\boldsymbol{k}}\left(\boldsymbol{r}\right). \qquad (2.74)
$$

For each $\boldsymbol{k}$, this is a boundary value problem for a single unit cell with a set of solutions indexed by j. The complete set of eigenstates is therefore given by $u_{j\boldsymbol{k}}(\boldsymbol{r})$ with the eigenenergies $\epsilon_{j\boldsymbol{k}}$. The states $u_{j\boldsymbol{k}}(\boldsymbol{r})$ can be made orthonormal on the unit cell. With the eigenstates, we can simply obtain the expectation value of a single particle via

$$\langle\varphi|\,\hat{O}\,|\varphi\rangle = \frac{\Omega}{(2\pi)^3}\int_{\mathrm{BZ}} d^3k \sum_j f_{j\boldsymbol{k}}\,\langle\varphi_{j\boldsymbol{k}}|\,\hat{O}\,|\varphi_{j\boldsymbol{k}}\rangle\,, \tag{2.75}$$

where Ω is the volume of a unit cell. Numerically, eq. 2.74 can be efficiently parallelized over $\boldsymbol{k}$-points, as there is an independent differential equation for every $\boldsymbol{k}$ ($\boldsymbol{k}$ is a quantum number, $\hat{H}$ is block-diagonal in $\boldsymbol{k}$). The $\boldsymbol{k}$-integral in eq. 2.75 cannot be evaluated exactly and is in practice approximated by a sum over a discrete set of $\boldsymbol{k}$-points. Finally we mention that Bloch's theorem and eqs. 2.74, 2.75 can be easily generalized to spin-dependent and time-dependent systems.

First and second variational step

In the Elk code, the KS equations for periodic systems are solved via a two-step process. In the "first-variational" step a purely electrostatic Hamiltonian with the kinetic energy, a scalar potential and an electric field is constructed

$$\hat{H} = \hat{T}_s + \hat{V}_{\mathrm{ext}} + \boldsymbol{E}\cdot\hat{\boldsymbol{r}} + \hat{V}_{\mathrm{xc}} \tag{2.76}$$

and diagonalized, $\hat{H}\,|\varphi_j\rangle = \epsilon_j\,|\varphi_j\rangle$. In the "second-variational" step, non-scalar effects are added, using the first-variational step as a basis:

$$H_{ij} = \epsilon_i\delta_{ij} + \langle\varphi_i|\,\hat{\boldsymbol{\sigma}}\cdot\boldsymbol{f} + \boldsymbol{g}\cdot\nabla\,|\varphi_j\rangle\,. \tag{2.77}$$

Here $\boldsymbol{f}$ contains all relevant magnetic and spin-dependent effects of the system, such as the Zeeman effect, SOC or the MDI and $\boldsymbol{g}$ typically corresponds to a vector potential in the system. Elk treats magnetism fully non-collinear instead of making the usual separation into spin-up and spin-down orbitals and potentials. To that end, the orbitals are fully variational spinor wavefunctions

$$\varphi_{j\boldsymbol{k}}(\boldsymbol{r}) = \begin{pmatrix} u^{\uparrow}_{j\boldsymbol{k}}(\boldsymbol{r}) \\ u^{\downarrow}_{j\boldsymbol{k}}(\boldsymbol{r}) \end{pmatrix} e^{i\boldsymbol{k}\cdot\boldsymbol{r}} \tag{2.78}$$

from which follows for the charge density $n(\boldsymbol{r}) = \sum_{j\boldsymbol{k}} \varphi^{\dagger}_{j\boldsymbol{k}}(\boldsymbol{r})\,\varphi_{j\boldsymbol{k}}(\boldsymbol{r})$ and for the magnetization density $\boldsymbol{m}(\boldsymbol{r}) = \sum_{j\boldsymbol{k}} \varphi^{\dagger}_{j\boldsymbol{k}}(\boldsymbol{r})\,\boldsymbol{\sigma}\varphi_{j\boldsymbol{k}}(\boldsymbol{r})$. Both, ultrafast (ch. 3) and ultra long-range (ch. 4) calculations are solved in the second-variational basis. As we do not update the first-variational basis, a large first-variational basis has to be chosen initially to allow for a sufficiently large second-variational basis.

The basis

Elk is an all electron code using the APW+LO (augmented plane waves plus local orbitals, ref. [39]) basis. The representation of a lattice periodic Bloch state $|u\rangle$ for given $n, \boldsymbol{k}$ in this basis is

$$|u\rangle = \sum_{l=0}^{l_{\max}} \sum_{m=-l}^{l} \sum_{n=1}^{N_{\max}^{l}} b_{lmn} \left|\psi_{\mathrm{lmn}}^{\mathrm{LO}}\right\rangle + \sum_{\boldsymbol{G}}^{N_{\max}^{\boldsymbol{G}}} a_{\boldsymbol{G}} \left|\psi_{\boldsymbol{G}}^{\mathrm{APW}}\right\rangle . \tag{2.79}$$

The central concept of the APW+LO basis is that the unit cell is divided into two different areas (fig. 2.3). The first term on the right-hand side in eq. 2.79 is concerned with the region in a sphere around each nucleus ("**m**uffin-**t**in", MT region). The sums run over the azimuthal number l, the magnetic number m and the number of **l**ocal **o**rbitals (LO) for a given l, n. $l_{\max}$ and $N_{\max}^{l}$ have to be chosen and can be increased for improved convergence. Inside the MTs the LOs are expanded in spherical harmonics,

$$\left\langle s, r, \theta, \phi \right| \left. \psi_{\mathrm{lmn}}^{\mathrm{LO}} \right\rangle = f_{lmn}^{s}\left(r\right) Y_{lm}\left(\theta, \phi\right) . \tag{2.80}$$

Outside the MTs the LOs evaluate to zero and do not contribute. The region outside of the MTs is called "**i**nterstitial **r**egion" (IR) and is represented by the second term in eq. 2.79. $N_{\max}^{\boldsymbol{G}}$ is the number of reciprocal lattice vectors $\boldsymbol{G}$ in the expansion, which is determined from an appropriately chosen cutoff length. In the IR, each APW is expanded with plane waves, i.e.

$$\left\langle s, \boldsymbol{r} \right| \psi_{\boldsymbol{G}}^{\mathrm{APW}} \left.\right\rangle \sim e^{i\boldsymbol{G}\cdot\boldsymbol{r}}. \tag{2.81}$$

The APWs are non-zero inside the MTs and expanded into radial functions. The form of the radial functions is similar to the LOs, however, the coefficients are not determined variationally. Instead, the radial functions have to be chosen such that the total wave function is continuous at all MT boundaries. We emphasize that the concept of MTs is of course not a physical concept but only an efficient numerical choice. Close to the nuclei the electrostatic potential is very strong and the wave function is rapidly changing (which can be efficiently represented by radial functions). Far away from the nuclei, the wave function drops off rapidly and is only weakly changing (almost like free electrons, best described by plane-waves). Thus when subdividing the unit cell into the IR and MTs of appropriate size, the total number of necessary basis functions can be drastically reduced. Finally we mention that APW+LO is a non-orthogonal basis, thus a generalized eigenvalue solver is required. For further details we refer to the text book by Singh [40].

Core and valence States

We already mentioned that Elk is an all-electron code. Especially for heavy atoms, the low lying electronic states will have a very large kinetic energy, to the extent that it is no longer accurate enough to treat them with the Schrödinger equation. This is solved in the ELK code by splitting the electronic states into core and valence states. Core states are all low-lying states which are strongly bound, have a large kinetic energy and are completely contained in the MTs. These states are solved

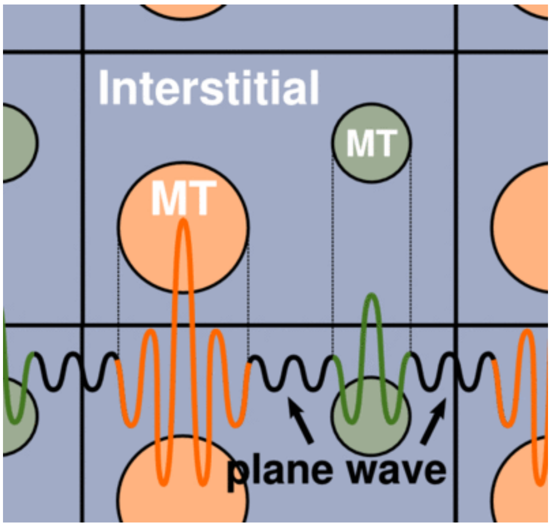

Figure 2.3
Schematic of the APW+LO basis. In a sphere around each nuclei (muffin-tins, “MT”), the wave function is expanded in spherical harmonics. In the remaining region (interstitial region, “IR”), the wave function is expanded in plane waves.

fully relativistically with the Dirac equation. Valence states refer to the states which are farther away from the atomic cores, are less strongly bound and have less kinetic energy. All valence states are solved with the scalar relativistic Schrödinger equation [41], which includes the Darwin-term and a relativistic mass correction (cf. section 2.4). The distinction between core and valence states becomes particularly important in chapters 3 and 4. For both time-dependent and large-scale calculations we do not re-evaluate the core states, as a significant change to the core states is only expected for a very strong external perturbation. For small to moderate changes in the external potentials and fields the electronic response is dominated by the loosely bound valence electrons.

3. Ultrafast demagnetization

In the late 1990s it was experimentally observed that femtosecond optical pulses interacting with magnetic matter lead to an ultrafast reduction (~100 fs) of the observed macroscopic magnetization [1–3]. This observation was nothing short of a scientific breakthrough and **u**ltra**f**ast **d**emagnetization (UFD) is still among the fastest known ways of altering the magnetization in a material. Not surprisingly, this discovery drew significant scientific interest and the dream of a magnetic device with femtosecond read/write times was born. Despite ample experimental and theoretical research, the driving mechanisms for UFD remain controversial. Experimentally, it remains difficult to achieve precise measurements at ultrafast time-scales and the exact electronic behavior is of course not accessible. Theoretically, one has to deal with an out of equilibrium, interacting many-particle system, for which methods are scarce. As a result, theoretical descriptions are often phenomenological and do not provide a microscopic understanding.

In this chapter, we report on two joint experimental and theoretical studies to unravel the physics of UFD. We will first start with briefly discussing previously suggested mechanisms for UFD. We will then give a basic review of the field of magneto-optics, on which the experimental measurements are based. We continue with a detailed explanation of our TDDFT approach to UFD. Finally, we show a direct comparison of experimental and theoretical results. We are able to extract the fundamental microscopic phenomena driving UFD at the fastest time scales. For a layered system of Co/Cu(001), we obtain the best reported agreement between experiment and theory so far.

3.1 First observation and suggested explanations

A common phenomenological approach to UFD is the “three-temperature model”, which assigns three different temperatures to the electron system, the spin system and the lattice system [1, 42, 43]. This model assumes that a short laser pulse leads to a different amount of heating and thus a different effective temperature within the electronic, spin and lattice systems. The heat induced by the laser will during the first $\approx 200\,\mathrm{fs}$ mostly affect the electronic and the spin system, resulting in an increase in the spin-temperature and hence a loss in the magnetic moment. At later times, the coupling between the electrons and the lattice will become more important, resulting in a heat flow from the electron and spin systems to the lattice system. As a consequence, the spin system will cool down and slowly relax back to its original magnetic configuration. While this mechanism describes the observed behavior quite well, it remains a phenomenological approach and does not provide insight into the microscopic details.

Demanding a microscopic explanation has, however, not narrowed down possible mechanisms but instead resulted in several proposed effects which may lead to ultra fast demagnetization. Already in 2000, it was suggested that UFD might be due to spin-orbit driven spin-flips during the excitation of the laser pulse [44]. However, in all experiments carried out so far, UFD does not occur during the excitation but is delayed and happens only shortly after the laser pulse is over. Another proposed mechanism for UFD was Elliott-Yaffett spin-flip scattering [45]. This describes the scattering of electrons with phonons in which the electronic spin is transferred to the angular momentum of phonons. It has been questioned, however, whether the scattering rate is high enough to fully explain the observed amount of demagnetization. The so-called superdiffusive model was put forward in 2010 [46] and assumes that majority spin-carriers are carrying magnetization away from the area of excitation. A final possible explanation we want to mention was proposed by Krieger et. al [6] and based on their parameter free, ab-initio treatment of the excitation process via TDDFT. Their conclusion was that demagnetization is a two-step process, where the laser pulse excites electrons and the demagnetization occurs due to subsequent spin-orbit mediated spin-flips of the remaining electrons.

The results obtained in this thesis challenge the superdiffusive model as the sole explanation for UFD and support a spin-orbit coupling mediated loss of the magnetization.

3.2 Ultrafast magneto-optics

Investigating magnetic phenomena on femtosecond time scales is also experimentally highly non-trivial. The only currently available methods on these time scales are “pump-probe” experiments. In a pump-probe experiment, a sample is first excited at a time $t = 0$ with a strong laser pulse (“pump” pulse) to kick the system out of equilibrium. After a certain time t, a second, much weaker pulse is applied to the sample (“probe” pulse). By measuring the transmitted or reflected part of the probe-pulse, information about the magnetization in the sample at time t can then be inferred. As the probe pulse is very weak, it is not expected to change the dynamics in the material considerably. We will discuss general properties of laser pulses and how to use them to measure a magnetization in more detail in the following.

3.2.1 Ultrashort laser pulses

We have already stated above that all investigations in the field of UFD rely on pump-probe experiments. To achieve femtosecond pump-probe experiments, it is of course necessary to have laser pulses with femtosecond pulse duration. Nowadays, femtosecond pulses of high intensity with almost arbitrary shape can be generated [47]. Maxwell's equations yield wave equations for the propagation of a laser pulse. In a vacuum, these wave equations are given by:

$$\Delta \boldsymbol{A}\left(\boldsymbol{r},t\right) - \frac{1}{c^2}\partial_t^2 \boldsymbol{A}\left(\boldsymbol{r},t\right) = 0, \tag{3.1}$$

$$\Delta \Phi\left(\boldsymbol{r},t\right) - \frac{1}{c^2}\partial_t^2 \Phi\left(\boldsymbol{r},t\right) = 0. \tag{3.2}$$

A simple, yet quite general solution is achieved by $\Phi\left(\boldsymbol{r},t\right) = 0$ ("radiation gauge") and using superpositions of plane waves for the vector potential,

$$\boldsymbol{A}\left(\boldsymbol{r},t\right) = \hat{\boldsymbol{a}} \int dk \tilde{A}\left(k\right) e^{i\left(\boldsymbol{k}\cdot\boldsymbol{r}-\omega t\right)},\ \boldsymbol{a} \perp \boldsymbol{k},\ \Phi\left(\boldsymbol{r},t\right) = 0. \tag{3.3}$$

Here $\boldsymbol{a}$ is the polarization vector which is always perpendicular to the propagation direction $\boldsymbol{k}$. $k = 2\pi/\lambda$ is the magnitude of the wave vector associated with wave length λ and ω is the angular frequency of the pulse. The electric and magnetic fields $\boldsymbol{E}\left(\boldsymbol{r},t\right), \boldsymbol{B}\left(\boldsymbol{r},t\right)$ associated with the vector potential $\boldsymbol{A}\left(\boldsymbol{r},t\right)$ are given by the usual relations (eqs. 2.7, 2.8). In a vacuum, the propagation speed of the pulse is simply given by $c = \omega/k$. In the general case of a laser pulse propagating through a medium, the dispersion relation $\omega\left(k\right)$ is typically much more involved and the propagation speed is given by $v = \partial\omega/\partial k$. Two quantities which are commonly used to describe the strength of a laser pulse are the peak intensity and the fluence. The peak intensity is given by $I = E_{\mathrm{max}}^2 c/8\pi$ and is measured in power per unit area, E_{max} is the maximum of the electric field. The fluence is measured in energy per unit area and can be obtained by a time integral of the intensity, $F = \int_{-\infty}^{\infty} dt \left[E\left(t\right)\right]^2 c/8\pi$.

Eq. 3.3 describes an extended pulse, but real pulses do of course not extend infinitely, neither in space nor in time. The spatial and temporal shape of a laser pulse is typically given by a Gaussian. An example of such a pulse traveling along the z-axis is given by

$$\boldsymbol{A}\left(\boldsymbol{r},t\right) = \hat{\boldsymbol{a}} \left|\boldsymbol{A}\right| e^{i\left(kz-\omega t\right)} e^{-\frac{\left(t-t_0\right)^2}{2\sigma_t^2}} e^{-\frac{\left(x-x_0\right)^2}{2\sigma_x^2}} e^{-\frac{\left(y-y_0\right)^2}{2\sigma_y^2}}, \tag{3.4}$$

where $\sigma_t, \sigma_x, \sigma_y$ are Gaussian standard deviations. It is simple to verify that eq. 3.4 also fulfills Maxwell's equations. Often, the **f**ull **w**idth at **h**alf **m**aximum (FWHM) is specified for the width of the pulse instead of the standard deviation. For a Gaussian pulse, it is simply given by FWHM $= 2\sqrt{2\ln 2}\sigma$.

We finish our considerations on the general properties of laser pulses with a closer look at the polarization vector $\boldsymbol{a}$. As we have stated previously, it should always be perpendicular to the propagation direction $\boldsymbol{k}$. We assume, without loss of generality, that $\boldsymbol{k} \parallel \boldsymbol{e}_z$. We can then define two orthonormal polarization vectors

$$\boldsymbol{a}_1 = \begin{pmatrix} \cos\theta \\ \sin\theta e^{2i\eta} \\ 0 \end{pmatrix},\ \boldsymbol{a}_2 = \begin{pmatrix} -\sin\theta \\ \cos\theta e^{-2i\eta} \\ 0 \end{pmatrix} \tag{3.5}$$

both of which generally have the form of an ellipse. Here, $0 \leq \theta \leq \pi$ is called orientation angle and $-\pi/4 \leq \eta \leq \pi$ is the ellipticity angle (fig. 3.1). While arbitrary superpositions of $\boldsymbol{a}_1, \boldsymbol{a}_2$ are of course possible, we assume for simplicity in the following that the polarization of our laser pulse is described by $\boldsymbol{a}_1$,

$$\boldsymbol{A}\left(\boldsymbol{r}, t\right) \propto \begin{pmatrix} \cos\theta e^{i(kz-\omega t)} \\ \sin\theta e^{i(kz-\omega t+2\eta)} \\ 0 \end{pmatrix}. \tag{3.6}$$

There are three different cases which one typically distinguishes. First, if $\eta = 0$, both the x and the y component of the vector potential, A_x, A_y, reach their respective maximum at the same time. This is referred to as “linearly-polarized”. If instead $\eta = \pm\pi/4$ and $\theta = \pi/4$, A_x is at its maximum when A_y is zero and vice versa, the laser pulse is right-handed ($\eta = \pi/4$) or left-handed ($\eta = -\pi/4$) circularly polarized. Two examples are shown in fig. 3.2. All other cases are called elliptically polarized. It should be clear that all of these cases can be represented by any two orthogonal vectors. Nonetheless, we mention that a linearly polarized laser pulse can be decomposed into two circularly polarized pulses:

$$\boldsymbol{a}_L = \boldsymbol{a}_+ + \boldsymbol{a}_- = \begin{pmatrix} 2 \\ 0 \\ 0 \end{pmatrix} = \begin{pmatrix} 1 \\ +i \\ 0 \end{pmatrix} + \begin{pmatrix} 1 \\ -i \\ 0 \end{pmatrix}. \tag{3.7}$$

This is a common decomposition encountered in magneto-optics, which will become important in the following sections.

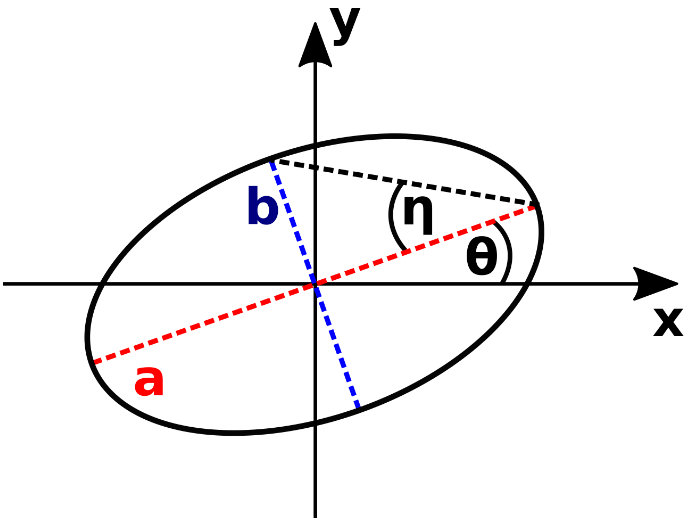

Figure 3.1
The polarization ellipse. a, b are the major and minor axes, respectively. $0 \leq \theta \leq \pi$ is the orientation angle and $-\pi/4 \leq \eta \leq \pi/4$ is the ellipticity angle. If $\eta = 0$, the laser pulse is linearly polarized, for $\eta = \pm\pi/4$ and $\theta = \pi/4$, the laser pulse is circularly polarized. For all other angles, the laser pulse is elliptically polarized.

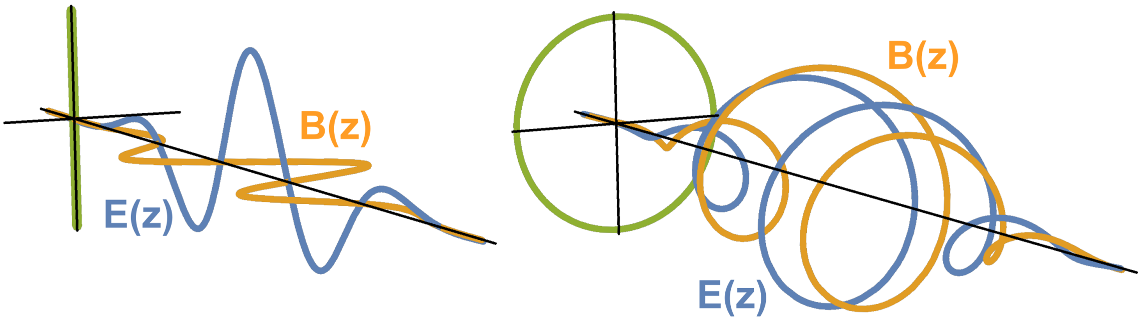

Figure 3.2
Linearly (left) and left-handed circularly (right) polarized pulses. The polarization ellipse for the electric field is shown in green. Both pulses have a Gaussian shape.

3.2.2 Laser pulses in magnetic materials - The Faraday effect

When a linearly polarized **e**lectro**m**agnetic **w**ave (EMW) travels parallel to the magnetization $\boldsymbol{M}$ in a material, a rotation of the polarization plane is observed (θ changes, fig. 3.1). The direction of the rotation hereby depends on the relative alignment of the EMW and the magnetization. Placing a mirror behind the magnetic material and forcing the EMW to travel through the magnet again from the opposite direction will thus double the observed rotation instead of reverting it to zero. This is due to the magnetization breaking time-inversion symmetry locally. The first experimental observation of this effect was already made in the 19th century by Michael Faraday and the effect is nowadays known as Faraday effect. Faraday made his original observations in non-magnetic materials subjected to an external magnetic field. He found the following formula:

$$\Delta\theta = \nu\left(\omega\right) H l, \tag{3.8}$$

where $\Delta\theta$ is the change in the angle of rotation, H is a magnetic field applied parallel to the propagation direction, l is the length of the path the EMW travels in the material and ν is the Verdet constant, which is material specific and generally depends on the frequency of the EMW. We will in the following give a brief theoretical explanation on this effect based on Maxwell's equations. Our derivations in this and the following subsection are based on the textbook on magneto-optics by Sugano [48].

Within classical electrodynamics, the electric displacement field $\boldsymbol{D}$ and the magnetic field $\boldsymbol{H}$ are the proper quantities for EMWs in materials, as they include the reaction of the material:

$$\boldsymbol{D} = \boldsymbol{E} + 4\pi\boldsymbol{P} = \underline{\underline{\epsilon}}\left(\omega, \boldsymbol{P}\right)\boldsymbol{E}, \tag{3.9}$$

$$\boldsymbol{H} = \boldsymbol{B} - 4\pi\boldsymbol{M} = \underline{\underline{\mu}}^{-1}\left(\omega, \boldsymbol{M}\right)\boldsymbol{B}. \tag{3.10}$$

$\boldsymbol{P}, \boldsymbol{M}$ are the classical polarization and magnetization. $\underline{\underline{\epsilon}}, \underline{\underline{\mu}}$ are the dielectric tensor and the permeability tensor.

For Maxwell's equations in materials we have

$$\nabla\cdot\ \boldsymbol{D} = 4\pi\rho_f \qquad \nabla\cdot\boldsymbol{B} = 0 \tag{3.11}$$

$$\nabla\times\boldsymbol{E} = -\frac{1}{c}\frac{\partial\boldsymbol{B}}{\partial t} \qquad \nabla\times\boldsymbol{H} = \frac{1}{c}\left(4\pi\boldsymbol{j}_f + \frac{\partial\boldsymbol{D}}{\partial t}\right) \tag{3.12}$$

where $\rho_f, \boldsymbol{j}_f$ are only the "free" charge and current densities of unbound electrons. For our basic considerations, it is sufficient to assume $\rho_f = 0, \boldsymbol{j}_f = 0$. Our main task is then to evaluate the remaining non-zero Maxwell equations, i.e.

$$\nabla\times\boldsymbol{E} = -\frac{1}{c}\underline{\underline{\mu}}\left(\omega, \boldsymbol{M}\right)\frac{\partial\boldsymbol{H}}{\partial t}, \qquad \nabla\times\boldsymbol{H} = \frac{1}{c}\underline{\underline{\epsilon}}\left(\omega, \boldsymbol{P}\right)\frac{\partial\boldsymbol{E}}{\partial t}. \tag{3.13}$$

The propagation of an EMW through a material depends only on the product of the permittivity and the permeability, $\underline{\underline{\epsilon}}\underline{\underline{\mu}}$ [49]. We can therefore always choose $\underline{\underline{\mu}} = 1$ by absorbing any functional dependence of the permeability into an effective permittivity $\tilde{\underline{\underline{\epsilon}}}$. If the magnetization is along the z-direction, $\tilde{\underline{\underline{\epsilon}}}$ is given by:

$$\tilde{\underline{\underline{\epsilon}}}\left(\omega, \boldsymbol{M}\right) = \begin{pmatrix} \epsilon_{xx} & \epsilon_{xy} & 0 \\ -\epsilon_{xy} & \epsilon_{xx} & 0 \\ 0 & 0 & \epsilon_{zz} \end{pmatrix}. \tag{3.14}$$

Because we are interested only in magneto-optical effects, we dropped the dependence on the polarization and will neglect it in the following. The tensor elements of $\tilde{\underline{\underline{\epsilon}}}\left(\omega, \boldsymbol{M}\right)$ obey $\epsilon_{xy}\left(\omega, \boldsymbol{M}\right) = \epsilon_{yx}\left(\omega, -\boldsymbol{M}\right) = -\epsilon_{yx}\left(\omega, \boldsymbol{M}\right)$ from which follows $\epsilon_{xy} \propto |\boldsymbol{M}|$, for small values of $|\boldsymbol{M}|$. Without giving a detailed proof, we will emphasize that this form makes intuitive sense. It is the shape one would expect from a quantum mechanical spin-system, with a longitudinal component along the quantization axis and coupled transversal components. We are now set for solving eqs. 3.13. We use a plane wave as an ansatz

$$\boldsymbol{E}\left(\boldsymbol{r}, t\right) = \boldsymbol{E}_0 e^{i(\boldsymbol{k}\cdot\boldsymbol{r}-\omega t)}, \quad \boldsymbol{H}\left(\boldsymbol{r}, t\right) = \boldsymbol{H}_0 e^{i(\boldsymbol{k}\cdot\boldsymbol{r}-\omega t)}, \quad \boldsymbol{H}_0, \boldsymbol{E}_0 \perp \boldsymbol{k} \tag{3.15}$$

and arrive at a set of linear equations for $\boldsymbol{E}, \boldsymbol{H}$,

$$\begin{aligned} \boldsymbol{k} \times \boldsymbol{E} &= \frac{\omega}{c}\boldsymbol{H}, \\ \boldsymbol{k} \times \boldsymbol{H} &= -\frac{\omega}{c}\,\tilde{\underline{\underline{\epsilon}}}\,\boldsymbol{E}, \end{aligned} \tag{3.16}$$

which we can solve for $\boldsymbol{E}$:

$$\boldsymbol{k}\left(\boldsymbol{k}\cdot\boldsymbol{E}\right) - k^2\boldsymbol{E} + \frac{\omega^2}{c^2}\tilde{\underline{\underline{\epsilon}}}\,\boldsymbol{E} = 0. \tag{3.17}$$

In accordance with the phenomenological observations of the Faraday effect, we choose the propagation direction along the z-direction as well, $\boldsymbol{k} \parallel \boldsymbol{M} \parallel \boldsymbol{e}_z$. As a result, $E_z = 0$ and we are left with finding a general solution for eq. 3.17 which allows for finite values of E_x, E_y. The equations for which are given by:

$$\begin{aligned} \left(n^2 - \epsilon_{xx}\right) E_x - \epsilon_{xy} E_y &= 0 \\ \epsilon_{xy} E_x + \left(n^2 - \epsilon_{xx}\right) E_y &= 0. \end{aligned} \tag{3.18}$$

Here $n^2 = c^2k^2/\omega^2$, which corresponds to the refractive index of the material. We explicitly allow k to be complex valued, resulting in a generally complex refractive index and an energy loss of the EMW as it propagates through the material. We obtain non-trivial solutions to eq. 3.18 if we choose:

$$n_\pm^2 = \epsilon_{xx} \pm i\epsilon_{xy}, \quad \pm iE_x = E_y. \tag{3.19}$$

We then obtain the following normal modes of the EMW

$$\boldsymbol{D}_+ = n_+^2 \left|\boldsymbol{E}\right| \left(\boldsymbol{e}_x + i\boldsymbol{e}_y\right), \quad \boldsymbol{D}_- = n_-^2 \left|\boldsymbol{E}\right| \left(\boldsymbol{e}_x - i\boldsymbol{e}_y\right), \tag{3.20}$$

which are right-handed and left-handed circularly polarized EMWs with different complex refractive indices $n_\pm^2$. As a result, two circularly polarized waves with different handedness propagating through a magnetic material will accumulate a difference in both, their relative phase and magnitude, due to the real and imaginary part of the refractive indices being different. When the two waves exit the magnetic material, these changes manifest themselves by a rotation of the orientation angle θ and by a change in the ellipticity η (fig. 3.1):

$$\theta_F = \frac{\omega}{2c}\mathrm{Re}\left(n_+ - n_-\right), \quad \eta_F = -\frac{\omega}{2c}\mathrm{Im}\left(n_+ - n_-\right). \tag{3.21}$$

The transmitted EMW is therefore in general elliptically polarized. Both, θ_F and η_F are experimentally accessible, θ_F is measured in Faraday experiments whereas η_F is measured in **m**agnetic **c**ircular **d**ichroism (MCD) experiments, which measure the difference in absorption of left and right-handed circularly polarized wave transversing a magnetic material. As a last step, it is illustrative to define the average refraction index and the average absorption:

$$n_0 = \frac{1}{2}\mathrm{Re}\left(n_+ + n_-\right), \quad \kappa_0 = \frac{1}{2}\mathrm{Im}\left(n_+ + n_-\right). \tag{3.22}$$

Using some basic algebra, this allows us to rewrite eqs. 3.21 as

$$\theta_F = -\frac{\omega}{2c}\frac{\kappa_0\mathrm{Re}\left(\epsilon_{xy}\right) - n_0\mathrm{Im}\left(\epsilon_{xy}\right)}{n_0^2 + \kappa_0^2}, \quad \eta_F = -\frac{\omega}{2c}\frac{n_0\mathrm{Re}\left(\epsilon_{xy}\right) - \kappa_0\mathrm{Im}\left(\epsilon_{xy}\right)}{n_0^2 + \kappa_0^2}. \tag{3.23}$$

In the limit of a transparent material, $n_0 \gg \kappa_0$, we find that $\theta_F \propto \mathrm{Im}\left(\epsilon_{xy}\right)$ and $\eta_F \propto -\mathrm{Re}\left(\epsilon_{xy}\right)$. Because $\epsilon_{xy} \propto \boldsymbol{M}$ for small $\boldsymbol{M}$, we also have that, to lowest order, θ_F and η_F are proportional to $\boldsymbol{M}$.

3.2.3 Reflection from surfaces - The magneto-optic Kerr effect

A second common method of measuring the magnetization in a sample is employing the **m**agneto-**o**ptic **K**err **e**ffect (MOKE), which is named after the Scottish Physicist John Kerr. In a MOKE experiment, the information about the magnetization is not obtained from the transmitted, but from the reflected EMW instead. The observed behavior varies, depending on the relative alignment of the magnetization, the plane of incidence of the EMW and the surface plane of the material (fig. 3.3). We will in the following consider the polar-MOKE, where both, the magnetization and the plane of incidence are parallel to each other and perpendicular to the material surface. In the previous section, we derived that the normal-modes of EMWs inside a magnetic material are given by circularly polarized waves. After an initial excitation, we can model the reflection process as circularly polarized waves being emitted from the material. We can then simply use the Fresnel equations to obtain the reflection coefficients for circularly polarized EMWs:

$$r_+ = \frac{n_+ - 1}{n_+ + 1}, \quad r_- = \frac{n_- - 1}{n_- + 1}. \tag{3.24}$$

We use the usual relations for circularly polarized waves $r_+ = r_x + ir_y$ and $r_- = r_x - ir_y$ to obtain

$$r_x = \frac{r_+ + r_-}{2}, \quad r_y = -i\frac{r_+ - r_-}{2}. \tag{3.25}$$

Therefore, the reflected signal will have a finite contribution for both, r_x and r_y. The complex Kerr-angle Φ_K, for small changes in the polarization of the reflected EMW, is then given by:

$$\Phi_K = \theta_K + i\eta_K \approx -\frac{r_y}{r_x} = \frac{i\left(r_+ - r_-\right)}{r_+ + r_-}, \tag{3.26}$$

Using eq. 3.24, we can rewrite this and obtain:

$$\theta_K = -\mathrm{Im}\frac{n_+ - n_-}{n_+ n_- - 1}, \quad \eta_K = \mathrm{Re}\frac{n_+ - n_-}{n_+ n_- - 1}. \tag{3.27}$$

Analogous to our considerations regarding the Faraday effect, it is instructive to consider the limit $n_0 \gg \kappa_0$, in which we have

$$\theta_K = -\frac{\mathrm{Re}\left(\epsilon_{xy}\right)}{n_0\left(n_0^2 - 1\right)}, \quad \eta_K = -\frac{\mathrm{Im}\left(\epsilon_{xy}\right)}{n_0\left(n_0^2 - 1\right)}. \tag{3.28}$$

We thus find that, compared to the Faraday effect, the role of the real and imaginary parts are inverted: θ_K, η_F are proportional to the real part of ϵ_{xy}, whereas η_K, θ_F are proportional to the imaginary part of ϵ_{xy}.

3.2.4 Magnetic second harmonic generation

The last method in magneto optics we will discuss is **m**agnetic **s**econd **h**armonic **g**eneration (MSHG), which is, unlike the MOKE and the Faraday effect, a non-linear effect and in comparison a very recent theoretical prediction [50]. The setup for MSHG is similar to the MOKE, in the sense that the change in the reflected wave from a sample is measured. The key difference, however, is that the second harmonic at frequency 2ω in the reflected signal is measured instead of the first harmonic at frequency ω. It is well known that centrosymmetric systems do not show a second harmonic in the reflected EMW, as centrosymmetric systems do not have tensors of even rank in the expansion of their response function (their is no even response to an odd excitation). In such systems, only interfaces or surfaces, where the inversion symmetry is broken, give rise to a second harmonic. The presence of magnetization does not break inversion symmetry, but alters the polarization

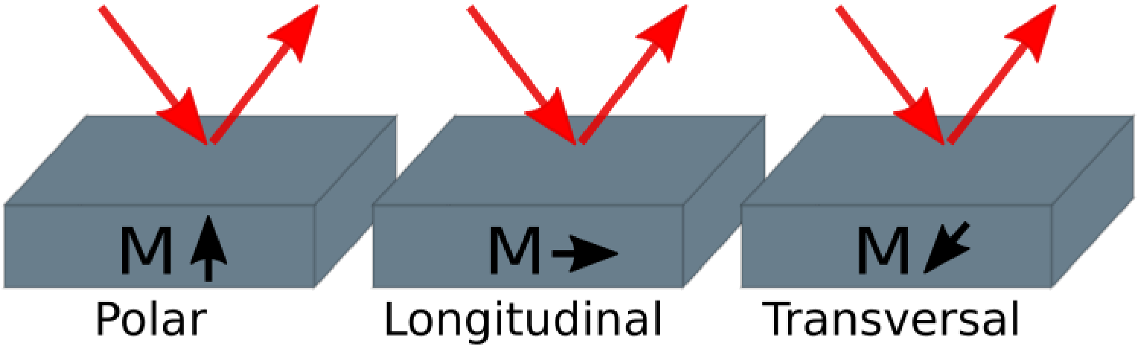

Figure 3.3
The magneto-optical Kerr effect can be characterized according to the orientation of the magnetization, the surface and the plane of incidence of the laser pulse. In the polar case, the magnetization is perpendicular to the surface and parallel to the plane of incidence. For the longitudinal case, the magnetization is parallel to the surface and the plane of incidence. Finally, the case where the magnetization is parallel to the surface and perpendicular to the plane of incidence is called transversal moke.

of a generated second harmonic. MSHG is therefore an extremely sensitive tool for measuring the contribution of surfaces or interfaces to the magnetization of the system.

We will only give a brief motivation on the theory behind MSHG. In our case, the relevant configuration is a transversal experiment, which is setup in the same way as the transversal MOKE (fig. 3.3). For such a case, the optical second harmonic polarization can be written as [51]

$$\boldsymbol{a}\left(2\omega, \pm\boldsymbol{M}\right) = \left(\vec{\chi}^{(2)}_{\text{even}}\left(\pm\boldsymbol{M}\right) \pm \vec{\chi}^{(2)}_{\text{odd}}\left(\pm\boldsymbol{M}\right)\right) E^{2}\left(\omega\right), \tag{3.29}$$

where $\vec{\chi}^{(2)}$ are the surface response functions and tensors of rank three. Even/odd refer to the sign change of the term under inversion of the magnetization. An intuitive picture is that the even term corresponds to a crystallographic response, whereas the odd term corresponds to a magnetic response. In a typical transversal MSHG experiment, the reflected intensities for opposite directions of the magnetization are measured, from which even and odd contributions can be inferred.

3.3 Ab-initio treatment of ultrafast demagnetization

In this section we will introduce our TD-SDFT framework which we use to study UFD theoretically. We will start with our time-dependent Kohn-Sham system (TD-KS) and continue with explaining all relevant approximations we make.

3.3.1 Time-dependent Kohn-Sham system

We use the TD-KS system introduced by Krieger et. al [6] to treat the interacting electronic system formally exact in real-time. This method has been applied successfully to varying systems, including transition metals in the original publication, the more complicated Heusler alloys [52] and thin film systems [53]. The TD-KS system we use is given by [6]:

$$\begin{aligned} i\partial_t \underline{\varphi}_j^{\boldsymbol{k}}(\boldsymbol{r},t) = & \left[\frac{1}{2}\left(-i\nabla + \frac{1}{c}\boldsymbol{A}_{\text{ext}}(t)\right)^2 + v_s(\boldsymbol{r},t) + \frac{1}{2c}\boldsymbol{\sigma}\cdot\boldsymbol{B}_s(\boldsymbol{r},t)\right. \\ & \left. + \frac{1}{4c^2}\boldsymbol{\sigma}\left(\nabla v_s(\boldsymbol{r},t)\times i\nabla\right)\right]\underline{\varphi}_j^{\boldsymbol{k}}(\boldsymbol{r},t) \end{aligned} \tag{3.30}$$

with
$$\begin{aligned} v_s(\boldsymbol{r},t) &= v_{\text{ext}}(\boldsymbol{r},t) + v_{\text{H}}[n](\boldsymbol{r},t) + v_{\text{xc}}^{\text{ALSDA}}[n,\boldsymbol{m}](\boldsymbol{r},t) \\ \boldsymbol{B}_{\text{s}}(\boldsymbol{r},t) &= \boldsymbol{B}_{\text{ext}}(t) + \boldsymbol{B}_{\text{xc}}^{\text{ALSDA}}[n,\boldsymbol{m}](\boldsymbol{r},t) \end{aligned}$$

and
$$\begin{aligned} n(\boldsymbol{r},t) &= \frac{1}{N_{\boldsymbol{k}}}\sum_{j,\boldsymbol{k}} f_j^{\boldsymbol{k}}\left|\underline{\varphi}_j^{\boldsymbol{k}}(\boldsymbol{r},t)\right|^2 \\ \boldsymbol{m}(\boldsymbol{r},t) &= \frac{1}{N_{\boldsymbol{k}}}\sum_{j,\boldsymbol{k}} f_j^{\boldsymbol{k}}\left(\underline{\varphi}_j^{\boldsymbol{k}}(\boldsymbol{r},t)\right)^\dagger \boldsymbol{\sigma}\underline{\varphi}_j^{\boldsymbol{k}}(\boldsymbol{r},t)\,. \end{aligned}$$

The KS potential and field $v_{\text{s}}(\boldsymbol{r},t)\,,\boldsymbol{B}_{\text{s}}(\boldsymbol{r},t)$ as well as the densities $n(\boldsymbol{r},t)$, $\boldsymbol{m}(\boldsymbol{r},t)$ are defined in accordance with chapter 2. The functional we will use in our calculations is the ALSDA (eq. 2.65). The last term on the right hand side is the relativistic spin-orbit coupling (eq. 2.71). This term is expected to be crucial in our calculations: Up to second order in the relativistic expansion (cf. section 2.4), only the Zeeman term and SOC violate conservation of spin momentum, thus allowing for a macroscopic decrease in the magnetization. Throughout this work, we approximate the SOC with a radial representation. For the laser pulse we use a classical vector potential and employ the dipole approximation, i.e. the vector potential is a function of time only, $\boldsymbol{A}_{\text{ext}} \equiv \boldsymbol{A}_{\text{ext}}(t)$. We provide more details on the approximations affecting the SOC and the laser pulse in the following subsections. In all our calculations, we treat the spins as fully noncollinear, which allows us to properly include spin currents, spin diffusion and spin flips. The Born-Oppenheimer approximation is used throughout this work. As a result, a possible contribution to UFD arising from phonons will not be captured by our approach. We do not expect this to majorly effect our results, as we limit our discussions to short time scales, where electronic processes are expected to dominate the dynamics.

A key difference to experiments is that we do not extract the information about the magnetization via a probe pulse. Instead, we directly calculate the magnetization from our KS-system (eq. 3.30). This may lead to a systematic difference between our simulations and experimental observations. A theoretical modeling of a pump probe experiment is much more computationally demanding and typically only of limited value, as the necessary numerical accuracy is difficult to reach.

There are some mathematical remarks we want to make. We note that it is not mathematically clear whether a KS of the form 3.30 is valid, as neither a rigorous proof of the RG nor of the van Leeuwen theorem for such a system exists. We also note that angular momentum is not conserved in any calculation we make. This has two reasons: First, due to employing the Born-Oppenheimer approximation, we have a fixed external potential in our system, therefore momentum and angular momentum are generally not conserved. This is well known from classical mechanics (e.g. a pendulum). Second, the spatial operator $\hat{\boldsymbol{r}}$ is not well-defined within periodic boundary conditions as it is not translationally invariant. Thus the angular momentum operator $\hat{\boldsymbol{L}} = \hat{\boldsymbol{r}} \times \hat{\boldsymbol{p}}$ is also not a well defined object and generally not conserved.

3.3.2 Spin-orbit coupling for radial potentials

In all calculations in this thesis, we assume that the KS potential $v_s(\boldsymbol{r}, t)$ in the SOC term is approximately a radial function:

$$\frac{1}{4c^2}\boldsymbol{\sigma} \cdot \left(\nabla v_s(\boldsymbol{r}, t) \times \hat{\boldsymbol{p}}\right) \approx \frac{1}{4c^2}\boldsymbol{\sigma} \cdot \left(\partial_r v_s(r, t)\, \boldsymbol{e}_r \times \hat{\boldsymbol{p}}\right). \tag{3.31}$$

This is typically a reasonable approximation, as the fastest changing contribution to $v_s(\boldsymbol{r}, t)$ arises from the nuclear potential, which is close to spherically symmetric near the nuclear positions. We furthermore assume that, in the spin-orbit term, the time-dependence of $v_s(\boldsymbol{r}, t)$ can be neglected, as the nuclei remain fixed during our calculations. We can then define the time-independent SOC radial functions:

$$\xi(r) = \frac{1}{2c^2 r}\partial_r v_s(r, 0). \tag{3.32}$$

With the definition of the angular momentum operator

$$\hat{\boldsymbol{L}} = r\boldsymbol{e}_r \times \hat{\boldsymbol{p}} \tag{3.33}$$

the spin-orbit coupling reduces to:

$$\frac{1}{4c^2}\boldsymbol{\sigma} \cdot \left(\nabla v_s(\boldsymbol{r}, t) \times \hat{\boldsymbol{p}}\right) \approx \frac{1}{2}\xi(r)\, \boldsymbol{\sigma} \cdot \hat{\boldsymbol{L}}. \tag{3.34}$$

This is the form we use in all following calculations. A more detailed numerical and analytical discussion showing that this approximation only leads to negligible effects can be found in the thesis by Krieger [54].

3.3.3 Classical vector potential and the dipole approximation

There are several approximations we make for describing the laser pulse. In eq. 3.30, the laser pulse is included as a classical field instead of quantized photon excitations.

For the exact treatment of electrons subjected to a laser pulse, using quantum electrodynamics would be necessary. However, if the density of phonons and the wave length of the laser pulse fulfill $n_{\mathrm{ph}} \gg 1/\lambda^3$, approximating the photon field by a classical field is justified [55]. In this work, we use laser pulses of $\approx 800\,\mathrm{nm}$ with peak intensities of at least $10^{-12}\,\mathrm{W\,cm^{-2}}$. We therefore expect that modeling the vector potential as a classical field is viable. A second approximation we made is the so-called "dipole-approximation", which assumes that the vector potential is given as a function of time only, $\boldsymbol{A}_{\mathrm{ext}} \equiv \boldsymbol{A}_{\mathrm{ext}}(t)$. The name for this approximation arose because this approximation, in the linear-response limit, limits electronic excitations in atoms to electric dipole transitions. Mathematically, this corresponds to taking only the constant term of the taylor expansion of a plane wave:

$$e^{i2\pi\frac{r}{\lambda}} = 1 + i2\pi\frac{r}{\lambda} - \frac{1}{2}\left(2\pi\frac{r}{\lambda}\right)^2 + \mathcal{O}\left(\frac{r^3}{\lambda^3}\right) \approx 1. \tag{3.35}$$

It can be easily seen from eq. 3.35 that the dipole approximation is valid as long as the maximum size of the system is much smaller then the wave length of the laser pulse $r_{\mathrm{max}} \ll \lambda$. This criterion is very well fulfilled in all following calculations, because we only consider layered systems with a few (≤ 10) atomic layers. For example, 10 layers of Ni are approximately 3.5 nm thick, which is small compared to a typical optical laser wavelength of around 800 nm. We note that there is a second limitation when applying the dipole approximation: The coupling of the vector potential $\boldsymbol{A}(\boldsymbol{r}, t)$ to the momentum operator $\hat{\boldsymbol{p}}$ will result in a breakdown of the approximation for very large pulse intensities [56]. As we use only moderate field strengths in this thesis, this should not affect us. For the laser pulses used in this thesis, we applied the dipole approximation to the pulse given in eq. 3.4. In addition, the spatial extent of the laser pulse is typically even larger than the wave length, the shape of the pulse has therefore only a tiny impact on the dynamics at the center of the pulse. The pulses in this work are thus purely time-dependent and read

$$\boldsymbol{A}(\boldsymbol{r}, t) = \hat{\boldsymbol{a}}\,|\boldsymbol{A}|\sin(\omega t + \delta)\,e^{-\frac{(t-t_0)^2}{2\sigma_t^2}}. \tag{3.36}$$

Finally, we note that our TD-KS system (eq. 3.30) is not coupled to Maxwell's equations. Radiative contributions from the material to the vector potential are thus not captured. We will, in the following, outline why such a coupling is difficult. As we solve for the electrostatic potential in the Coulomb gauge, we also have to evaluate the vector potential in the Coulomb gauge. The vector potential in Coulomb gauge is generally given by the following wave equation [57]:

$$\Delta\boldsymbol{A}(\boldsymbol{r}, t) - \frac{1}{c^2}\partial_t^2\boldsymbol{A}(\boldsymbol{r}, t) = -\frac{4\pi}{c}\boldsymbol{j}_T(\boldsymbol{r}, t), \tag{3.37}$$

where $\boldsymbol{j}_T(\boldsymbol{r}, t)$ is the transverse current, which is used instead of the normal current $\boldsymbol{j}(\boldsymbol{r}, t)$ to maintain causality in the Coulomb gauge. It is given by

$$\boldsymbol{j}_T(\boldsymbol{r}, t) = \boldsymbol{j}(\boldsymbol{r}, t) + \frac{1}{4\pi}\nabla\left(\nabla\cdot\int d^3r'\frac{\boldsymbol{j}(\boldsymbol{r}', t)}{|\boldsymbol{r}-\boldsymbol{r}'|}\right). \tag{3.38}$$

The total effective current in this case can be easily obtained by rearranging the second equation in eq. 3.12 and is given by

$$\boldsymbol{j}\left(\boldsymbol{r},t\right)=\boldsymbol{j}_f\left(\boldsymbol{r},t\right)+c\nabla\times\boldsymbol{M}\left(\boldsymbol{r},t\right)+\partial_t\boldsymbol{P}\left(\boldsymbol{r},t\right). \tag{3.39}$$

While formulating the equations is quite simple, there are numerous problems in practice. First, one would need to have a good approximation for $\boldsymbol{A}_{\mathrm{xc}}\left(\boldsymbol{r},t\right)$ to ensure that $\boldsymbol{j}_f\left(\boldsymbol{r},t\right)$ reproduces the correct current at every time step. Good approximations are, however, not available. Second, there is currently no trivial way to obtain the polarization as a functional of the density and it would become necessary to also treat the polarization as an extra variable. Lastly, even if we would assume the contribution from the polarization to be negligible and would use the KS current as a rough approximation to the real current, $\boldsymbol{j}\left(\boldsymbol{r},t\right)=\boldsymbol{j}_s\left(\boldsymbol{r},t\right)$, solving Maxwell's equations along the KS system would remain very impractical. The vector potential is then no longer given by a plain wave, thus the dipole approximation does not hold any more. As the laser pulse propagates much faster than electronic currents, an extremely large system would be required to keep track of the spatial dependence of both, the laser pulse and the electrons. This is computationally not feasible. A solution to this could be our ultra long-range approach (cf. chapter 4).

3.3.4 The time propagation

The first step in evaluating all of our systems is performing a self-consistent, time-independent DFT ground state calculation of the system, from which we will obtain the ground state charge and magnetization densities as well as the ground state KS orbitals and occupation numbers. As stated previously, we use the APW+LO basis along with periodic boundary conditions, for which the eigenstates are given by Bloch orbitals. We then perform a time evolution of the system according to eq. 3.30, where the external laser pulse drives the system out of equilibrium. As we are propagating in real-time, we capture non-linear effects. We do not change any details or convergence parameters in our system for the time evolution, i.e. the boundary conditions, the basis and all convergence parameters (e.g. $\boldsymbol{k}$-points) remain the same. Therefore, a rather large number of empty states has to be added already to the ground state calculation into which electrons can be excited during the time propagation. As discussed in section 2.5, the core states remain unchanged throughout the time-propagation. For the actual time-propagation, we use the method by Dewhurst et. al [58]. Starting from the ground state KS orbitals φ_i^{G}, the time propagation up to a final time T with time steps Δt is achieved by:

1. Set $\varphi_j\left(\boldsymbol{r},t\right)=\sum_i c_{ij}\left(t\right)\varphi_i^{\mathrm{G}}\left(\boldsymbol{r}\right)$.
2. Compute $\rho\left(\boldsymbol{r},t\right)$ and $\boldsymbol{m}\left(\boldsymbol{r},t\right)$.
3. Compute $v_s\left(\boldsymbol{r},t\right),\boldsymbol{B}_s\left(\boldsymbol{r},t\right),\boldsymbol{A}_{\mathrm{ext}}\left(t\right)$ to obtain $\hat{H}\left(t\right)$ (eq. 3.30).
4. Compute $H_{ij}=\left\langle\varphi_i^{\mathrm{G}}\middle|\hat{H}\left(t\right)\middle|\varphi_j^{\mathrm{G}}\right\rangle$.

5. Solve $H_{ik}d_{kj} = \epsilon_j d_{ij}$ for d and ϵ.
6. Compute $c_{ij}(t + \Delta t) = \sum_{kl} d^*_{jk} d_{lk} e^{-i\epsilon_k \Delta t} c_{il}(t)$.
7. If $t < T$ go to step 1.

For more details on the performance and stability of the algorithm, see [58].

3.4 Spin flips versus spin transport in optically excited transition metals

In this section we report on a joint theoretical and experimental effort aiming at achieving a better understanding of the physics underlying ultrafast demagnetization in thin films of Ni and Co. Our goal is unraveling whether spin transport or spin-flips are the dominating contribution in UFD. The experimental contributions were made by the group of Jean-Yves Bigot in Strasbourg, only the theoretical work was made within the framework of this thesis. The joint results have been published [59].

Experimentally, four different samples are measured: For each material (Ni,Co) two samples with thicknesses of 10 and 40 nm are measured. A magneto-optical pump-probe setup is employed which pumps the system at the front face (F) of a sample and measures the signal at both, front and back face (B) of the sample. From this the complex Voigt vector $\tilde{Q} = Qe^{i\varphi_q} = -i\epsilon_{xy}/\epsilon_{xx}$ is constructed. The modulus Q of the Voigt vector is proportional to the magnetization, which can be seen from our considerations on the Faraday effect (subsection 3.2.2) and the MOKE (subsection 3.2.3). A polar geometry is chosen. The experimental pump pulse has a wavelength of 800 nm, a fluence of $5 \times 10^{-2}\,\mathrm{mJ\,cm^{-2}}$ and a duration of 10 fs.

The central experimental results are shown in fig. 3.4. For the 10 nm Ni film we observe a larger demagnetization at the back face (≈ 1.9 times), indicating that spins have propagated through the material. The simultaneous demagnetization of both the front and the back face cannot be explained by a flow of only majority spins. This is in strong contrast with the superdiffusive model, which suggests that only majority spins are moving. For the 40 nm thick film we see a smaller demagnetization at the back face (≈ 0.7 times), which is most likely a result of electron scattering/spin-flips as electrons are propagating through the sample. A very different situation is observed in Co: During the first 50 fs a clear sign inversion is visible on the back face of the 10 nm film, which implies that during this time predominantly majority spins are arriving at the back face. This sign inversion is not present for the 40 nm film suggesting again that scattering and spin-flips are more important in the thicker sample. Experimentally, the estimated typical propagation length on which spin-flips occur in Co was estimated to be 25 ± 3 nm. The estimate was made by performing the same experiment on samples of different thicknesses.

For a better in-depth, microscopic understanding, we perform TD-SDFT calculations of Ni and Co thin films employing the Hamiltonian given in eq. 3.30. In all our calculations, our thin films are seven **m**ono **l**ayers (ML) thick, as only minor

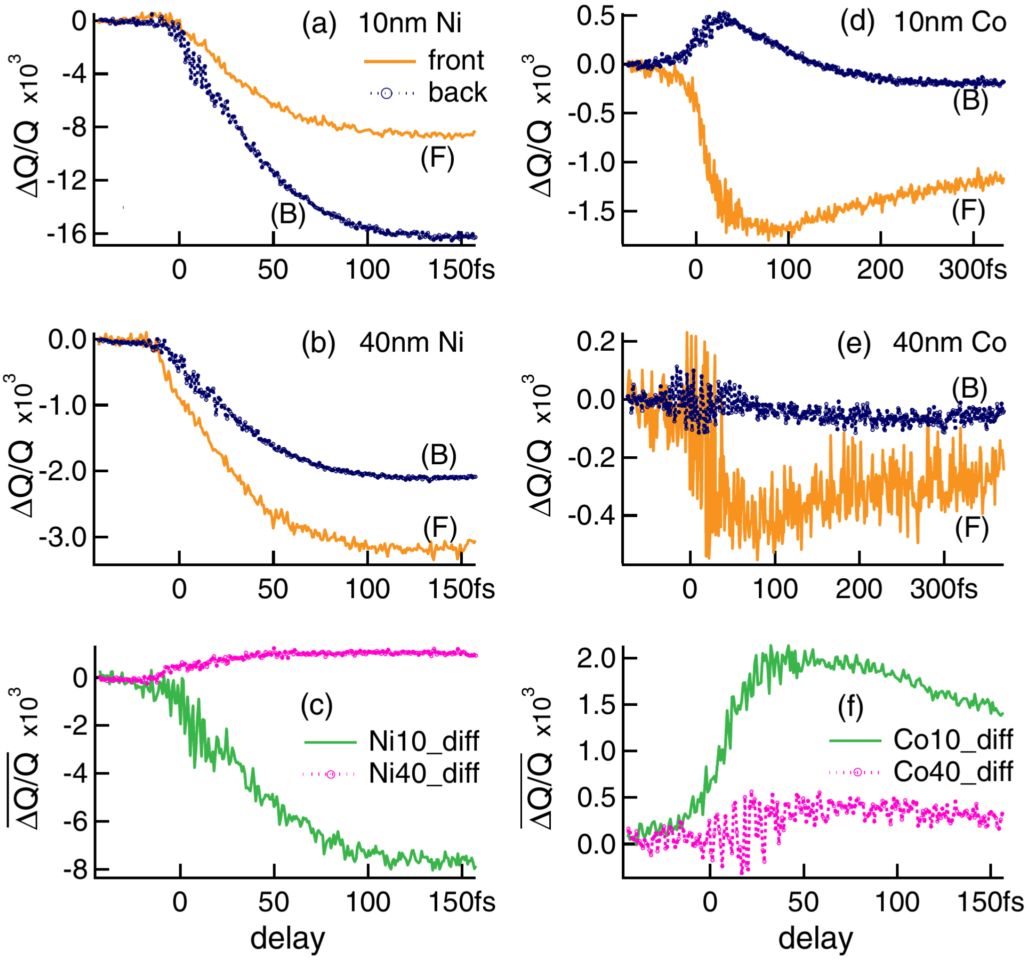

Figure 3.4
Experimental ultrafast magnetization dynamics of Ni and Co films excited with 10 fs pulses probed on their front (*F*) and back (*B*) faces. Results are for a) 10 nm Ni, b) 40 nm Ni, d) 10 nm Co, e) 40 nm Co samples. Panels c) and f) are the differences between the *B* and *F* faces for Ni and Co samples, respectively.

changes were observed as long as the films were at least five ML thick. The laser pulse we use is polarized along the sample plane, has a FWHM of 16 fs a frequency of 1.55 eV corresponding to $\approx 800\,\mathrm{nm}$ and an average power density of $10^{12}\,\mathrm{W\,cm^{-2}}$. Our power density is ten times larger than in the experiment. This is in order to make the effects more easily visible as we are using a smaller system. We note that our observations hold for weaker pulses. We use a regular $8 \times 8 \times 1$ $\boldsymbol{k}$-point grid, an angular momentum cutoff of 8 for the orbitals and 7 for densities and potentials. Our time step for the time evolution is $\Delta t = 0.05$.

In fig. 3.5 we present the change in majority and minority charge averaged over all 7 layers as a function of time, $\Delta n\,(t) = n_{\mathrm{maj/min}}(t) - n_{\mathrm{maj/min}}\,(t=0)$. We calculated the changes in both spin channels from the total charge and the magnitude of the magnetization inside the MTs (eq. 2.51). Our results clearly show that the occupation in both spin channels is changing significantly, supporting the experimental findings. Such a change in majority and minority spins is in strong contrast with the super diffusive model. We present further analysis of the time-dependent phenomena in fig. 3.6, which shows the normalized total (a) and c)) and layer resolved (b) and d)) moment for Ni and Co, $|M\,(t)|\,/\,|M\,(t=0)|$. In the case of the layer resolved results, we performed two calculations, one with SOC (last term in eq. 3.30) and one without SOC. Without SOC, the only possible mechanism for demangetization is due to flow of spin-currents, similar to what is proposed by the superdiffusive model. Including SOC adds the contributions from spin flips and spin canting. We clearly find that, like in the experiment, Ni demagnetizes more than Co. This could be due to the almost completely filled d orbital in Ni, therefore any change in the minority spin occupation leads to a large change in the moment. Our layer resolved results (figs. 3.6b), d)) show that the contribution of spin diffusion in the case of Ni is very small and spin flips occur already at very early times. In Co, however, a clear distinction between a purely diffusive and a spin flip model only occurs at later times: A saturation of the diffusive contribution is reached after ~20 fs, at which point spin flips become the dominant contribution. In this early time ($< 20\,\mathrm{fs}$), the magnetization dynamics in Co are thus different than that of Ni, as Co shows significant diffusion of majority spins. This difference explains the experimental findings: In the early times, majority spins accumulate at the back face of Co, leading to an increased magnetic moment. Shortly afterwards, spin flips start to become the significant contribution resulting in a global demagnetization. Ni is in contrast to this, the temporal separation between spin currents and spin flips is small and spin flips, which cause a global demagnetization, dominate the demagnetization process already at early times.

We conclude that both, our theoretical and experimental observations cannot be described by the superdiffusive model alone. Furthermore, we generally conclude that a model that takes into account majority spins only, will not be able to describe UFD in both, Co and Ni. Only the combination of spin-currents and SOC mediated spin-flips is capable of explaining both systems. Finally, we note that our results for Ni can also explain previous experimental findings [60].

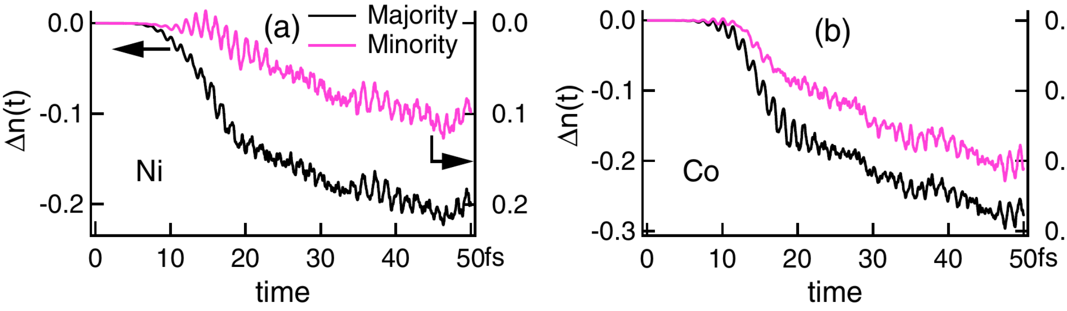

Figure 3.5
Layer averaged majority (left axis) and minority (right axis) as a function of time (in femtoseconds). The results for Ni are shown in the left panel and for Co in the right panel. As compared to the t=0 case there is a decrease in the majority and an increase in the minority spins. The difference in the change of the spin channels of ≈ 0.1 can be attributed to delocalized electrons, which are no longer associated with a layer.

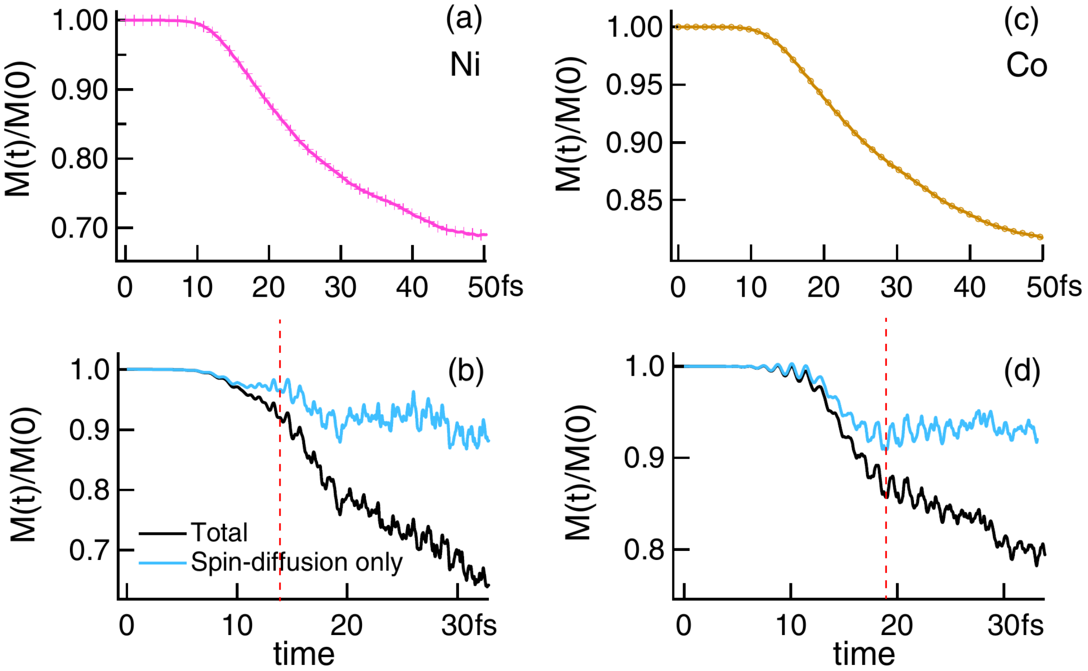

Figure 3.6
Total a),c) and layer resolved b),d) normalized magnetic moment for Ni and Co films as a function of time (in femtoseconds). The layer resolved results are calculated in two ways: 1) by time propagating the full Hamiltonian (black) and (2) by leaving out the spin-orbit contribution (blue). The layer resolved data are for a representative layer (third layer) of a seven ML thick film. The vertical dotted lines in panels b) and d) show the time at which demagnetization due to spin diffusion starts to saturate.

3.5 Competing spin transfer and dissipation at Co/Cu(001) interfaces

In a second joint experimental/theoretical study, we examine the effect of interfaces between different materials on UFD. The experimental work presented in this section was not carried out as a part of this thesis. All experimental results were obtained by the group of Prof. Uwe Bovensiepen at the University of Duisburg-Essen. The content of this section has been published previously [61].

The system we investigate is the ferromagnetic-paramagnetic (FM/PM) interface Co/Cu(001). Experimentally, femtosecond time-resolved MSHG is employed, which is specifically sensitive to the interface, where the inversion symmetry is broken (cf. subsection 3.2.4). Theoretically, we again use TD-SDFT with an added SOC term (eq. 3.30). We treat very similar systems in both cases: Experimentally, an ultrathin film of 3 or 5 **m**ono **l**ayers (ML) of Co on top of Cu(001) is measured. In our theoretical calculation, we simulate 3 or 5 ML of Co on top of 7 ML of Cu(001). This makes a quantitative comparison between experiment and theory possible and enables us to distinguish all relevant microscopic processes at times $t < 100\,\mathrm{fs}$ at the Co/Cu(001) interface. We find a competition of photoexcited spin transfer from Co to Cu and back transfer from Cu to Co as well as a demagnetization by SOC-mediated spin flips.

In the experiment Co/Cu(001) films with epitaxial, atomically sharp interfaces are prepared, characterized and measured in situ at room temperature in ultrahigh vacuum at a pressure smaller than $1 \times 10^{-10}\,\mathrm{mbar}$. A pump probe MSHG experiment with 35 fs (FWHM) laser pulses with 800 nm wavelength is performed and the laser-induced magnetization dynamics at 400 nm wavelength are analyzed. The incident pump fluence is $F = 4 \pm 2\,\mathrm{mJ\,cm^{-2}}$. All films are magnetized parallel to the sample surface, perpendicular to the optical plane and the second harmonic generated by the probe pulse is detected in transversal geometry (figs. 3.3, 3.7).

From the measured second harmonic intensities $I^{\uparrow,\downarrow}$ for opposite orientations of the magnetization $\boldsymbol{M}$, the second harmonic fields

$$\left|E^{2\omega}_{\text{even}}\right| \approx \frac{1}{\sqrt{2}}\sqrt{(I^{\uparrow} + I^{\downarrow})}, \quad \left|E^{2\omega}_{\text{odd}}\right| \approx \frac{I^{\uparrow} - I^{\downarrow}}{4\left|E^{2\omega}_{\text{even}}\right|} \tag{3.40}$$

are obtained, which behave even and odd with reversal of $\boldsymbol{M}$, respectively. They are considered magnetization independent and magnetization dependent for $E^{2\omega}_{\text{even}} \gg E^{2\omega}_{\text{odd}}$ [62, 63]. The time-dependent changes are normalized to their respective values before laser excitation and are represented by

$$\Delta^{2\omega}_{\text{even,odd}} = \frac{E^{2\omega}_{\text{even,odd}}(t)}{E^{2\omega}_{\text{even,odd}}(t < 0)} - 1, \tag{3.41}$$

which measure charge and spin dynamics separately. Further experimental details can be found in ref. [64].

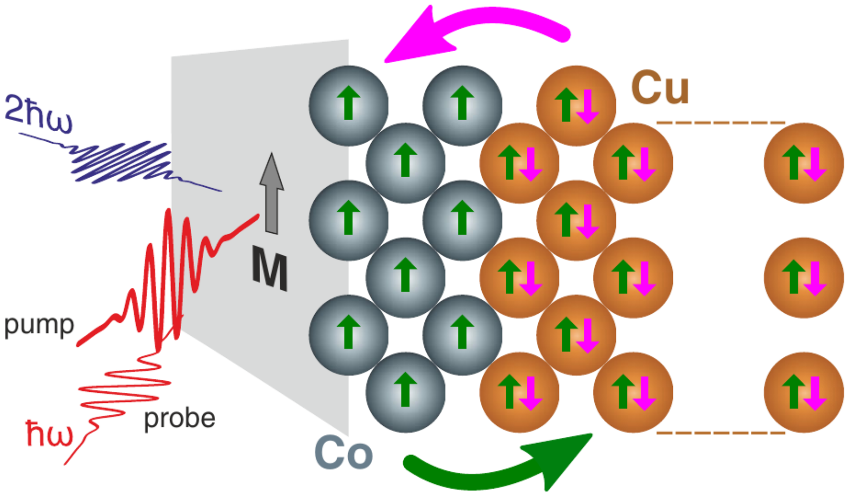

Figure 3.7
Illustration of the epitaxial model interface Co/Cu(001), the interface-sensitive pump-probe experiment and spin transfer dynamics. Vertical arrows indicate spins and magnetic order in Co. Cu carries negligible spin polarization before optical excitation. Horizontal arrows indicate spin transfer across the interface. The Co magnetization M is oriented perpendicular to the optical plane. Pump and probe pulses are s polarized and p polarized, respectively.

As mentioned above, our TD-SDFT calculations were performed for slabs of 3 or 5 ML Co on top of 7 ML Cu(001). We use a pump laser pulse of 35 fs (FWHM) pulse length, 800 nm wavelength (1.55 eV) and an incident pump fluence of $F = 0.25\,\mathrm{mJ\,cm^{-2}}$. This fraction corresponds to the fluence absorbed by the Co/Cu(001) heterostructure in the experiment. In this way, we properly account for the fact that $\approx 94\%$ of the incident pump fluence is rejected from the sample surface. While it is in principle possible to include the reflection from the surface in our simulation by coupling our time-dependent system to Maxwell's equations, this is not feasible in practice (cf. subsection 3.3.3). In our simulation, we monitor the change in the spin-integrated charge density n and the magnetic moment μ:

$$\Delta n = \frac{n\,(t)}{n\,(t<0)} - 1, \quad \Delta\mu = \frac{\mu\,(t)}{\mu\,(t<0)} - 1. \tag{3.42}$$

In fig. 3.8a we present experimental and theoretical results for three and five layers of cobalt on top of Cu(001) (bulk substrate experimentally, 7 ML theoretically). The experimental results are presented together with the pump-probe cross-correlation (CC) measured on the sample surface, which indicates the experimental time resolution. The experimental charge dynamics, reflected by $\Delta^{2\omega}_{\mathrm{even}}$ (fig. 3.8a), show an immediate response already at $t < 0$, due to the finite duration of the laser pulse. The maximum change is reached at about 50 fs. A full recovery of $\Delta^{2\omega}_{\mathrm{even}}$ to the value before pump excitation is measured to take around 700 fs.

The TD-SDFT results in fig. 3.8a analyze the relative change in the spin-integrated charge carrier number in the Co film, $n_{\mathrm{Co}}(t)$. As the total charge is conserved, $n_{\mathrm{Co}}(t)$ quantifies the flow of optically excited, spin-integrated charge carriers across the Co/Cu(001) interface. $n_{\mathrm{Co}}(t)$ and $\Delta^{2\omega}_{\mathrm{even}}$ show a different evolution with t, which could be caused by not simulating a full pump-probe experiment in TD-DFT. However, $n_{\mathrm{Co}}(t)$ and $\Delta^{2\omega}_{\mathrm{even}}$ share the same temporal profile and reach, within uncertainties, their respective minimum at the same time. We thus conclude that the change in $\Delta^{2\omega}_{\mathrm{even}}$ is dominated by spin-integrated charge transfer across the interface. We observe that TD-SDFT even manages to capture the small difference in the magnitude between the 3 and 5 ML system. Lastly, The observed recovery of $n_{\mathrm{Co}}(t)$ starting at 30 fs most likely indicates a backflow of charge from Cu to Co.

Fig. 3.8b shows the results for $\Delta^{2\omega}_{\mathrm{odd}}$ and the calculated time-dependent change of the Co spin magnetic moment $\Delta\mu_{\mathrm{Co}}(t)$, where $\mu_{\mathrm{Co}} \propto \mu^{\uparrow}_{\mathrm{Co}} - \mu^{\downarrow}_{\mathrm{Co}}$ ($\uparrow, \downarrow$ correspond to majority/minority carriers, respectively). $\Delta^{2\omega}_{\mathrm{odd}}$ has a qualitatively different behavior compared to $\Delta^{2\omega}_{\mathrm{even}}$. The change starts at $t = 0$ and is slower than $\Delta^{2\omega}_{\mathrm{even}}$. $\Delta^{2\omega}_{\mathrm{odd}}$ only reaches its minimum after around 100 fs. This observation hints at additional processes observed in the dynamics of the interface magnetization probed by $\Delta^{2\omega}_{\mathrm{odd}}$, which is further supported by the slower recovery time (fig. 3.8b, inset) of $\Delta^{2\omega}_{\mathrm{odd}}$. The timescale and behavior of $\Delta^{2\omega}_{\mathrm{odd}}$ matches $\Delta\mu_{\mathrm{Co}}(t)$ excellently.

Based on the agreement between theory and experiment, we can derive further information which is not accessible by the experiment alone. Fig. 3.9 (left) compares $\Delta^{2\omega}_{\mathrm{odd}}$ for 3 ML Co/Cu(001) to three different calculated curves, which account for the spin moment change (i) in the full heterostructure ($\Delta\mu$), (ii) only the Co contribution ($\Delta\mu_{\mathrm{Co}}$) with SOC and (iii) the contribution of Co without SOC (last term in eq. 3.30). Without SOC, the total magnetization $\Delta\mu$ is conserved and the only change in the magnetization $\Delta\mu_{\mathrm{Co}}$ is due to transfer of local moments between Co and Cu. (ii) and (iii) coincide up to ≈ 35 fs, which indicates the time window during which spin-dependent charge transfer dominates the magnetization dynamics. Comparing (ii) and (iii) therefore quantifies the extent of spin-orbit mediated demagnetization. Without SOC, the loss in μ_{Co} levels off after ≈ 35 fs, while the system continues to lose magnetization up to ≈ 100 fs when SOC is included. Furthermore, including SOC roughly doubles the observed demagnetization. Our findings indicate that both, spin-transfer and SOC contribute to UFD with an approximately equal amount, but dominate on different, subsequent timescales. The quantitative agreement between theory and experiment thus allows us to identify a SOC mediated contribution to femtosecond demagnetization, as predicted by theory [6, 44, 65]. We, moreover, observe a larger pump-induced decrease in $\mu_{\mathrm{Co}}(t)$ than in $\mu(t)$ at any given t. The difference of $\mu(t)$ and $\mu_{\mathrm{Co}}(t)$ corresponds to the dynamics of the spin moment induced in Cu, $\mu_{\mathrm{Cu}}(t)$, shown in fig. 3.9 (right). $\mu_{\mathrm{Cu}}(t)$ reaches its maximum at $t = 35$ fs and recedes on longer times. Similar to Co, the reduction observed for $35\,\mathrm{fs} < t < 100\,\mathrm{fs}$ is due to the coupling of both spin channels via SOC. Electron-electron scattering than leads to spin-flip processes and spin moment loss. Based on our TD-SDFT calculations, we estimate the spin injection efficiency from Co to Cu before SOC mediates spin-flips start to dominate by $|\mu_{\mathrm{Cu}}(35\,\mathrm{fs}) - \mu_{\mathrm{Cu}}(t < 0)| \,/\, |\mu_{\mathrm{Co}}(35\,\mathrm{fs}) - \mu_{\mathrm{Co}}(t < 0)|$. We obtain a spin-injection

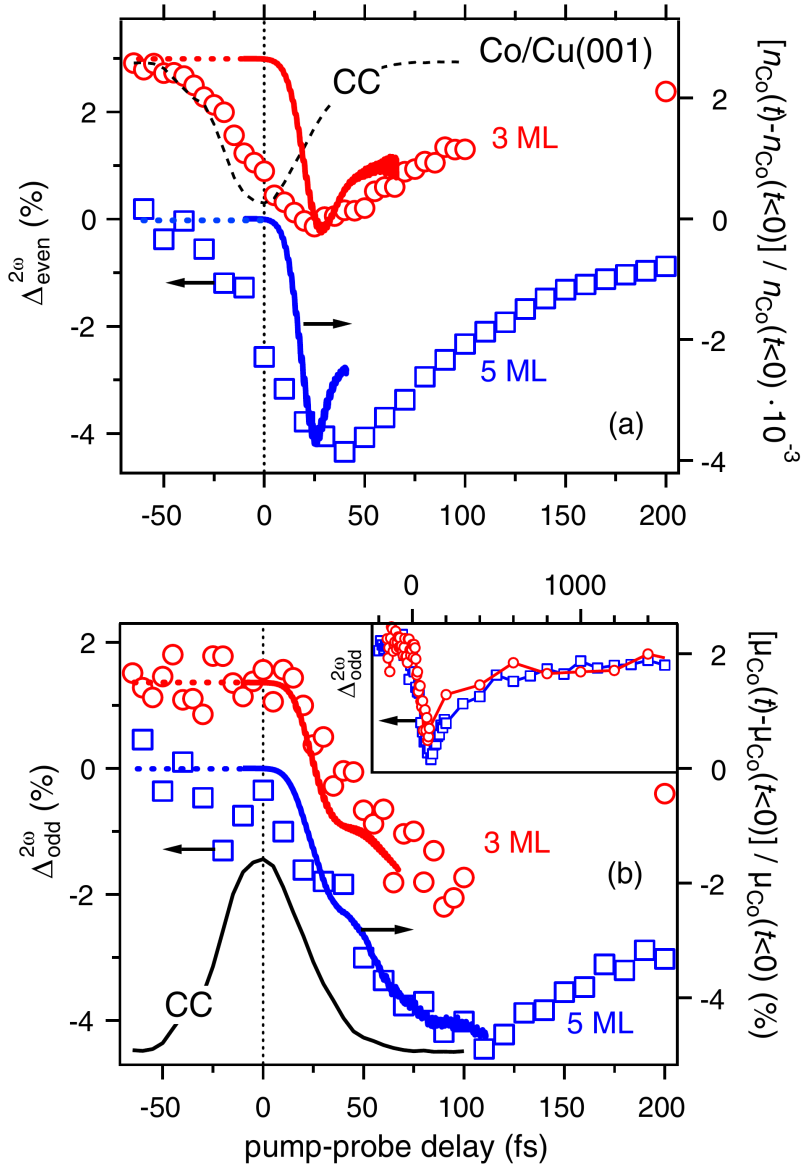

Figure 3.8
Pump-induced relative changes in second harmonic fields $\Delta^{2\omega}_{\mathrm{even}}$ (a) and $\Delta^{2\omega}_{\mathrm{odd}}$ (b) for 3 (circles) and 5 ML Co/Cu(001) (squares). Black lines indicate the pump-probe cross-correlation at the sample surface. It is shown inverted in (a). In addition, solid lines show (a) the relative change of spin-integrated charge carriers n_{Co} and (b) the relative change of the Co magnetic moment as calculated by TDDFT. Data for different Co thicknesses are vertically offset for display. The inset depicts $\Delta^{2\omega}_{\mathrm{odd}}$ for longer delays.

efficiency of 40% (25%) for 3 (5) ML Co/Cu(001).

The dynamics of the spin-integrated charge carriers in Cu shown in fig. 3.10a reinforces that the dynamics in the initial $\approx 35\,\mathrm{fs}$ are driven by charge transfer, as the pump induced charge saturates after this time. Fig. 3.10b displays the calculated time-dependent change of the number of majority (↑) and minority (↓) carriers in Co (n_{Co}) and Cu (n_{Cu}) layers. The increase of $n^{\uparrow}_{\mathrm{Cu}}$ simultaneous with the decrease of $n^{\uparrow}_{\mathrm{Co}}$ is a consequence of spin transfer from ferromagnetic Co to paramagnetic Cu. We observe a much weaker increase in Cu compared to the decrease in Co, indicating SOC driven spin flips, which limit the spin injection efficiency from Co to Cu. Additionally, we observe different rates of change in $n^{\uparrow}_{\mathrm{Co}}$ and $n^{\downarrow}_{\mathrm{Co}}$ before and after $\approx 35\,\mathrm{fs}$, which can again be attributed to SOC becoming the dominant process after this point in time. The turning point at $\approx 35\,\mathrm{fs}$ coincides with the length of the pump pulse, suggesting that spin transfer remains dominant as long as the pump pulse excites further carriers. We also note that $n^{\downarrow}_{\mathrm{Cu}}$ decreases more than $n^{\uparrow}_{\mathrm{Cu}}$ increases, pointing at back transfer of minority carriers from Cu to Co, enhancing the demagnetization in Co. This back transfer can be explained by a resonant optical excitation with the employed 1.5 eV pump photon energy from occupied Cu minority $3d$ states to unoccupied Co minority $3d$ states. The electronic density of states (fig 3.10c) supports such an optically driven minority spin back transfer from Cu to Co only directly at the interface, where hybridization of Cu and Co generates new Cu $3d$ states closer to the Fermi energy E_F than in bulk Cu [66, 67]. This finding is in accordance with previous observations that optically excited spin transfer is determined by the availability of empty states around E_F [52, 68, 69]. The amount of excitation can therefore be tuned by changing either the substrate or the pump pulse frequency.

Our results show that inclusion of spin-dependent charge transfer from the substrate and the actual electronic structure at the interface impact the dynamics of UFD. The back transfer of minority spins from Cu to Co is not captured in theories which only rely on spin-dependent life times as input for modeling laser-induced spin transport. It is important to properly include spin-dependent charge transfer excitations across the interface. We find that SOC mediated spin flips can occur on sub 100 fs time scales, as has been reported previously in model calculations without accounting for phonon excitations [44, 65]. As this timescale is much faster than Elliott-Yafet phonon-mediated spin-flip scattering [43], it might be closer to the rate-limiting process in UFD. On the other hand, SOC mediates the interaction of the magnetic moment with the lattice, which will inevitably act as a sink for the angular momentum [70].

In summary, we were thus able to identify three different processes dominating ultrafast demagnetization at Co/Cu(001) interfaces during subsequent time intervals: For $t < 35\,\mathrm{fs}$, spin transfer and back transfer between Co and Cu occur, followed by SOC mediated spin flips during $35\,\mathrm{fs} < t < 100\,\mathrm{fs}$, after which phonon-mediated process dominate. Phonon excitation can lead to both, further demagnetization [43, 71] or relaxation. In the experiments in our present study, the interaction with phonons leads to a relaxation of the magnetization due to energy transport from the FM layer to the PM substrate. Our finding of a minority spin back transfer from Cu to Co due to a resonant optical transition at the interface layers' density of states opens new possibilities for optical control of spin dynamics on femtosecond timescales via tunable laser pulses.

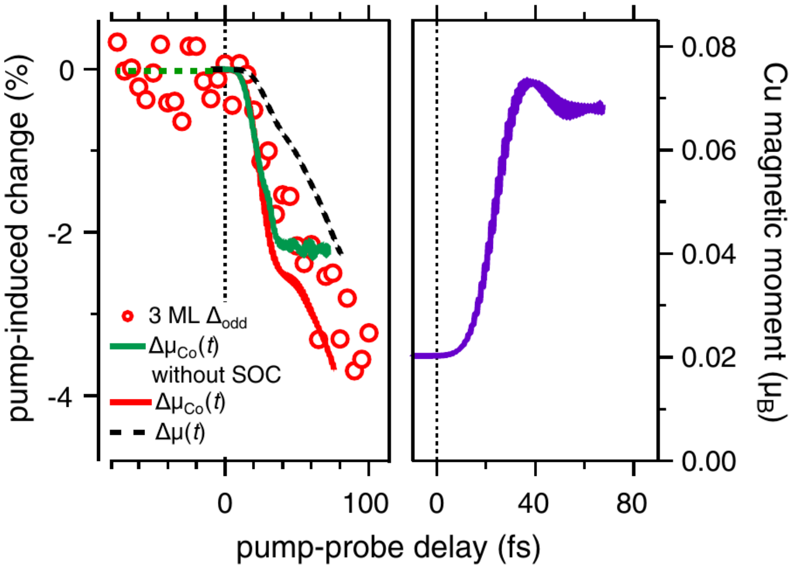

Figure 3.9
Left: Comparison of the time-dependent change of magnetic moment for 3 ML Co/Cu(001) as observed in experiment by $\Delta^{2\omega}_{\mathrm{odd}}$ and by TDDFT calculations. The relative changes (normalized to values $\mu\,(t<0)$ before excitation) of the total spin moment in Co/Cu(001) $\Delta\mu$ as well as of the Co contributions $\Delta\mu_{\mathrm{Co}}$ with and without SOC are given. Right: Magnetic moment induced in Cu, μ_{Cu}, by spin transfer across the interface.

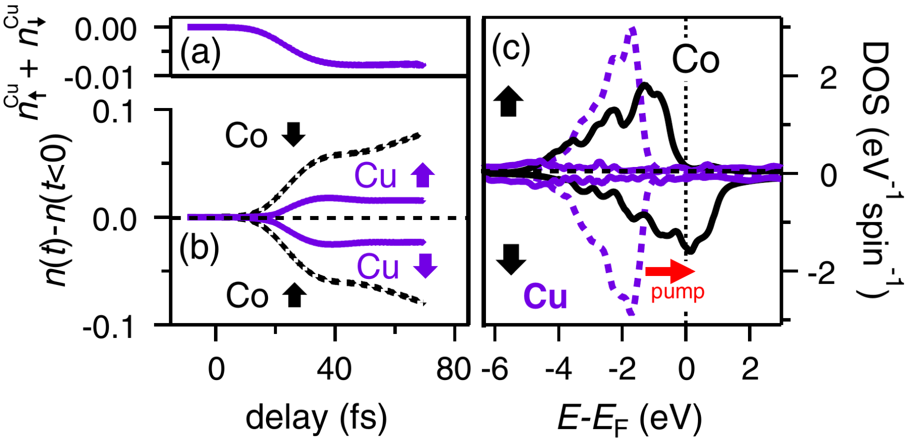

Figure 3.10
(a) Sum of spin polarized carriers in Cu. (b) Calculated change of number of excited majority and minority charge carriers $n_{\uparrow,\downarrow}$ localized at Co and Cu for 3 ML Co/Cu(001) as a function of pump-probe delay. (c) Electronic density of states (DOS) of Co and Cu layers at the interface (Cu d and sp states: dashed respectively solid lines). The horizontal arrow indicates the optical pump transition.

4. Density functional theory for ultra long-range phenomena

We have established in chapter 2 that, compared to traditional wave function approaches, a massive reduction in computational cost can be achieved by choosing the density as the fundamental quantity. While employing the KS approach has proven to be a highly successful trade-off between efficiency and accurately capturing the kinetic energy, solving the KS system still comes with some computational cost. This is typically not a problem for microscopic quantities, which can be derived from simple, periodic solids with only a few atoms in the atomic basis. Computational cost, however, will become a limiting factor if physical effects are to be considered with a periodicity much larger than the length of a single unit cell. Such effects may include light propagating through a solid (cf. subsection 3.3.3), long-ranged collective excitations, such as phonons, or large-scale magnetic structures, such as magnetic domains. The usual supercell (SC) approach, in which many adjacent unit cells are grouped together as a new basis, is no longer computationally viable for these systems. Each additional atom adds a full set of electronic states to be accounted for. In a typical calculation a matrix with a size proportional to the number of electronic states in the system has to be diagonalized, resulting in an overall scaling of the computational cost of approximately $\mathcal{O}\left(N_{\text{atom}}^3\right)$ (with the number of atoms in the system N_{atom}). This cubic scaling plagues all DFT codes with a systematic basis set and limits computations to systems containing a maximum of ≈ 1000 atoms. While recently proposed methods based on Chebyshev filtering [72, 73] or linear scaling ($\mathcal{O}\left(N_{\text{atom}}\right)$) approaches [74] were able to increase the computable system size considerably, these methods come with their own difficulties: Although Chebyshev filtering reduces the number of $\mathcal{O}\left(N_{\text{atom}}^3\right)$ steps in a self-consistent cycle, it of course does not negate the cubic scaling completely, which will ultimately be the limiting factor. Linear scaling approaches, on the other hand, require a “nearsightedness” of the system and assume that couplings inside the material drop off exponentially. While this might be fulfilled for effects strictly related to the charge density (i.e. XC potential and screened Coulomb interaction), this is certainly not fulfilled for large magnetic systems, such as magnetic domains.

In this chapter, we propose a fundamentally different approach to drastically extend the length scale of DFT calculations without significantly increasing the computational cost. Our **u**ltra **l**ong-**r**ange (ULR) approach relies on altered Bloch states and can be understood as a generalization of the spin-spiral ansatz [75, 76], which emerges as a special case of our ansatz. In the spin-spiral ansatz, a spin-dependent phase is added to the normal Bloch state. It then becomes possible to compute a large, extended spiraling magnetic moment within a single unit cell. While this is computationally very efficient, it is, at the same time, the biggest limitation of the spin-spiral ansatz: It only allows for a change in the direction of the magnetization while the magnitude of the magnetization and the charge density remain unaltered. We overcome this limitation by introducing an additional sum in the Bloch states over a finer grid in reciprocal space around each $\boldsymbol{k}$-point. The resulting densities then become a Fourier series with a controllable periodicity, which may extend far beyond the length scale of a single unit cell.

Before formally introducing our method, we will first briefly revisit the MDI, which is known to contribute to non-trivial magnetic order on large scales, such as magnetic domains. We will then proceed to derive a general ultra long-range KS system including external fields, the Coulomb interaction and the MDI. We demonstrate the accuracy and efficiency of our method with two electrostatic benchmark calculations in bulk Si and Li. We directly compare our results in Si to results obtained from a SC calculation. In the case of Li, we manage to solve over 6000 unit cells within two days on 220 cores. We proof that our method is well capable of capturing subtle magnetic systems by computing the spin-spiral state in γ-Fe and the **s**pin-**d**ensity **w**ave state in bulk Cr. Finally, we will briefly discuss a generalization to the time-dependent case and how it could make a coupling of our ULR KS system to Maxwell's equation possible. The results of this section have been published previously [77].

4.1 The magnetic dipole interaction and magnetic domains

It is experimentally well established that inside a ferromagnetic material regions with a preferred magnetic direction, so-called magnetic domains, exist. The key energy terms are believed to be the XC magnetic field (eq. 2.56) and the MDI (eq. 2.72). In this section, we will revisit the MDI and discuss its effect on the formation of ferromagnetic domains. In section 2.4, we saw that the quantum mechanical MDI appears as a second order term in the relativistic $1/c$ expansion of quantum electrodynamics

$$
\begin{aligned}
H^{\mathrm{DP}} &\equiv H^{\mathrm{dip}} + H^{\mathrm{sc}}, \qquad (4.1)\\
H^{\mathrm{dip}} &= -\frac{1}{8c^2}\sum_{j\neq k}\left[\frac{3\left[\boldsymbol{\sigma}_j\cdot(\boldsymbol{r}_j-\boldsymbol{r}_k)\right]\left[(\boldsymbol{r}_j-\boldsymbol{r}_k)\cdot\boldsymbol{\sigma}_j\right]}{r_{jk}^5}-\frac{\boldsymbol{\sigma}_j\cdot\boldsymbol{\sigma}_k}{r_{jk}^3}\right],\\
H^{\mathrm{sc}} &= -\frac{\pi}{3c^2}\sum_{j\neq k}\delta\left(\boldsymbol{r}_j-\boldsymbol{r}_k\right)\boldsymbol{\sigma}_j\cdot\boldsymbol{\sigma}_k,
\end{aligned}
$$

where we defined the non-local contribution H^{dip} and the local spin-contact contribution H^{sc}. The quantum mechanical MDI is analogous to the classical magnetostatic interaction between two magnetic dipoles. While it is the leading order magnetic-magnetic interaction in the expansion, the MDI is almost always neglected in DFT calculations. This is because the effective XC magnetic field (e.g. 2.56) arising from the Coulomb interaction and the Pauli exclusion principle is much stronger as it lacks the prefactor of $1/c^2$. The XC magnetic field is, however, inherently very short-ranged and is zero for electrons with non-overlapping wave functions. The MDI on the other hand has "infinite"-range, as it drops of as $\approx 1/r^3$. In a ferromagnet, the XC field directly competes with the MDI: Whereas the XC field heavily favors a local alignment of magnetic moments, the MDI favors a global anti-alignment. It is this competition which is believed to be the origin of the formation of magnetic domains. Magnetic domains, however, are very large and may extend up to the low micron regime. Therefore, despite having the underlying interactions readily at hand, ab-initio calculations of magnetic domains are not computationally feasible and no such calculation exists. Usually one therefore resorts to a semi-classical treatment of magnetic domains via the Landau-Lifshitz-Gilbert equation [5]. The method we introduce in the remainder of this chapter will enable large scale DFT calculations, and maybe even calculations of magnetic domains in particular.

For now, however, we focus on general properties of the MDI and show how to compute it in practice. It is straight forward to calculate the classical magnetostatic energy contribution of the MDI, which reads:

$$E^{\mathrm{DP}}\left[\boldsymbol{m}\right] = -\frac{\mu_{\mathrm{B}}^2}{2}\int \mathrm{d}\boldsymbol{r}\int \mathrm{d}\boldsymbol{r}'\frac{3\left(\boldsymbol{m}\left(\boldsymbol{r}\right)\cdot\boldsymbol{e}_{\boldsymbol{r},\boldsymbol{r}'}\right)\left(\boldsymbol{m}\left(\boldsymbol{r}'\right)\cdot\boldsymbol{e}_{\boldsymbol{r},\boldsymbol{r}'}\right)-\boldsymbol{m}\left(\boldsymbol{r}\right)\boldsymbol{m}\left(\boldsymbol{r}'\right)}{\left|\boldsymbol{r}-\boldsymbol{r}'\right|^3} - \frac{4\pi}{3}\mu_B^2\int \mathrm{d}\boldsymbol{r}\,\boldsymbol{m}^2\left(\boldsymbol{r}\right). \tag{4.2}$$

Here $\boldsymbol{e}_{\boldsymbol{r},\boldsymbol{r}'} = \left(\boldsymbol{r}-\boldsymbol{r}'\right)/\left|\boldsymbol{r}-\boldsymbol{r}'\right|$. The magnetic field associated with the magnetization $\boldsymbol{m}\left(\boldsymbol{r}'\right)$ is then given by the functional derivative with respect to $\mu_{\mathrm{B}}\boldsymbol{m}\left(\boldsymbol{r}\right)$,

$$\boldsymbol{B}^{\mathrm{DP}}\left(\boldsymbol{r}\right) = -\mu_{\mathrm{B}}\int \mathrm{d}\boldsymbol{r}'\frac{3\left(\boldsymbol{m}\left(\boldsymbol{r}'\right)\cdot\boldsymbol{e}_{\boldsymbol{r},\boldsymbol{r}'}\right)\boldsymbol{e}_{\boldsymbol{r},\boldsymbol{r}'}-\boldsymbol{m}\left(\boldsymbol{r}'\right)}{\left|\boldsymbol{r}-\boldsymbol{r}'\right|^3} - \frac{8\pi}{3}\mu_B\boldsymbol{m}\left(\boldsymbol{r}\right). \tag{4.3}$$

$\boldsymbol{B}^{\mathrm{DP}}\left(\boldsymbol{r}\right)$ can be easily calculated by first evaluating the vector potential associated with the MDI [57]:

$$\boldsymbol{A}^{\mathrm{DP}}\left(\boldsymbol{r}\right) = \mu_{\mathrm{B}}\int \mathrm{d}\boldsymbol{r}'\frac{\nabla\times\boldsymbol{m}\left(\boldsymbol{r}'\right)}{\left|\boldsymbol{r}-\boldsymbol{r}'\right|}, \tag{4.4}$$

for which the usual relation $\nabla\times\boldsymbol{A}^{\mathrm{DP}}\left(\boldsymbol{r}\right) = \boldsymbol{B}^{\mathrm{DP}}\left(\boldsymbol{r}\right)$ holds. Each component of $\boldsymbol{A}^{\mathrm{DP}}\left(\boldsymbol{r}\right)$ is given by a Poisson equation, which can be solved easily by most DFT codes. We use the method by Weinert [78] for solving Poisson's equation in the Elk code. We note that the vector potential also bears physical meaning and will yield a kinetic energy contribution due to a Lorentz force created by the spin-magnetic field. Therefore, in the most general case, both the vector potential and the magnetic field should be added to a Schrödinger equation.

We conclude our considerations on the MDI with the special case of a system with a homogeneous magnetization. It is easy to show that the mean-field energy of the non-local term $\boldsymbol{H}^{\mathrm{dip}}$ (eq. 4.1) vanishes in this case. If, for example, we choose $\boldsymbol{m}(\boldsymbol{r}) = m\boldsymbol{e}_z$ and make the shift $\boldsymbol{r} \to \boldsymbol{r} + \boldsymbol{r'}$ we obtain

$$E^{\mathrm{dip}}[\boldsymbol{m}] = -\frac{\mu_B^2}{2}\boldsymbol{m}^2 \int \mathrm{d}\boldsymbol{r} \int \mathrm{d}\boldsymbol{r'} \frac{3\cos\theta^2 - 1}{|\boldsymbol{r}|^3} \tag{4.5}$$

where θ is the angle between $\boldsymbol{e}_z$ and $\boldsymbol{e}_{\boldsymbol{r}}$. The angular integration now corresponds to a full angular integration over a spherical harmonic and thus vanishes. Therefore, for homogeneous systems, only the contact interaction contributes.

4.2 Ultra long-range ansatz

We will formally introduce our ULR method in this section. We consider a system which can be described by the following KS equations:

$$\hat{H}_0 = -\frac{\nabla^2}{2} + v_s(\boldsymbol{r}) + \mu_B \boldsymbol{B}_s(\boldsymbol{r}) \cdot \boldsymbol{\sigma} + 2i\mu_B (\boldsymbol{A}_{\mathrm{ext}}(\boldsymbol{r}) \cdot \nabla) + 2\mu_B^2 \boldsymbol{A}_{\mathrm{ext}}^2(\boldsymbol{r}). \tag{4.6}$$

The KS potential $v_s(\boldsymbol{r}) = v_{\mathrm{ext}}(\boldsymbol{r}) + v_{\mathrm{H}}(\boldsymbol{r}) + v_{\mathrm{xc}}(\boldsymbol{r})$ consists of an external potential v_{ext}, a Hartree potential v_{H} and an XC potential v_{xc}. Similarly, the KS magnetic field $\boldsymbol{B}_s(\boldsymbol{r}) = \boldsymbol{B}_{\mathrm{ext}}(\boldsymbol{r}) + \boldsymbol{B}_{\mathrm{xc}}(\boldsymbol{r}) + \boldsymbol{B}_{\mathrm{DP}}(\boldsymbol{r})$ can be decomposed into an external field $\boldsymbol{B}_{\mathrm{ext}}$, an XC-field $\boldsymbol{B}_{\mathrm{xc}}$ and a magnetic dipole field $\boldsymbol{B}_{\mathrm{DP}}$ (eq. 4.3). Finally, $\boldsymbol{A}_{\mathrm{ext}}$ is an external vector potential in the Coulomb gauge.

In this section, we will extend eq. 4.6 to large length scales. We will first derive a generalization of the Bloch state from which long-ranged charge and magnetization densities follow. From these densities, we will infer an ULR Hamiltonian and derive all matrix elements of said Hamiltonian explicitly.

4.2.1 Wave function and densities

The central idea of our approach relies on a generalization of the Bloch state. A similar idea was put forward with the spin-spiral ansatz [75, 76], which will emerge as a special case of our approach. While in the spin-spiral ansatz only a spin-dependent phase is added to the spinor Bloch state, we in addition introduce a full set of momentum-dependent expansion coefficients, enabling also a change in the magnitude of the magnetization and charge densities. For a fixed $\boldsymbol{k}$-vector our Bloch state reads:

$$\Phi_\alpha^{\boldsymbol{k}}(\boldsymbol{r}) = \frac{1}{\sqrt{N_u}} \sum_{j\boldsymbol{\kappa}} c_{j\boldsymbol{k}+\boldsymbol{\kappa}}^{\alpha} \begin{pmatrix} u_{j\boldsymbol{k}}^{\uparrow}(\boldsymbol{r}) \\ u_{j\boldsymbol{k}}^{\downarrow}(\boldsymbol{r}) \end{pmatrix} e^{i(\boldsymbol{k}+\boldsymbol{\kappa})\cdot\boldsymbol{r}}. \tag{4.7}$$

where $u_{j\boldsymbol{k}}^{\uparrow\downarrow}$ are the normalized orbitals of a lattice-periodic system, j is a band index and $\boldsymbol{k}$ a reciprocal space vector. $c_{j\boldsymbol{k}+\boldsymbol{\kappa}}^{\alpha}$ are complex coefficients to be determined

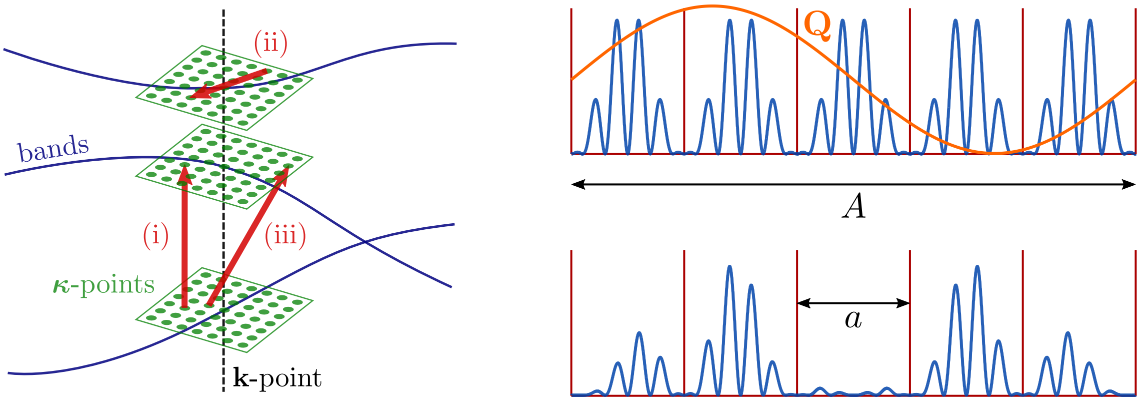

(a) **(b)**

Figure 4.1
a) Schematic of the $\boldsymbol{\kappa}$-point grid. For each $\boldsymbol{k}$-point (black dashed line) all bands (blue) are augmented with a fine grid of $\boldsymbol{\kappa}$-points (green). Three different types of couplings between $\boldsymbol{\kappa}$-points corresponding to different length scales are possible. a) A coupling between different $\boldsymbol{\kappa}$-points sharing the same band index, b) a coupling between two identical $\boldsymbol{\kappa}$-points but with different band indices and c) a coupling between different $\boldsymbol{\kappa}$-points with different band indices. The maximum length scale of the calculation may be choosen by adjusting the $\boldsymbol{\kappa}$-point grid. b) A schematic of the long range approach. The red lines indicate unit cells. The lattice periodic density $n_{\boldsymbol{Q}}$ (blue) is altered by a $\boldsymbol{Q}$-dependent modulation (orange) with a different periodicity. The result (lower graph) depends on both, the long-range modulation and the lattice periodic solution. a is the lattice constant of a unit cell and A is the lattice constant of the ultra cell, which is the smallest cell that contains the full long-range solution.

variationally. $\alpha = 1, \ldots, n_{\boldsymbol{\kappa}} \times n_j$ is a state index and $\boldsymbol{\kappa}$ is the index of an additional, finer grid around each $\boldsymbol{k}$-point in reciprocal space (fig. 4.1a), which we use to sample long-range effects. Finally N_u is a normalization factor which is equal to the number of unit cells on which $\Phi_{\alpha}^{\boldsymbol{k}}$ is periodic. We have used the lattice periodic parts of the orbitals at $\boldsymbol{k}$ and not $\boldsymbol{k}+\boldsymbol{\kappa}$ here. In principle, both are complete basis sets capable of expanding any lattice-periodic function. In practice, the choice of using $u_{j\boldsymbol{k}}^{\uparrow\downarrow}$ over $u_{j\boldsymbol{k}+\boldsymbol{\kappa}}^{\uparrow\downarrow}$ is more efficient for determining the density, magnetization and Hamilton matrix elements.

From this wave function, we can construct a charge and magnetization density:

$$n\left(\boldsymbol{r}\right) = \frac{1}{N_k} \sum_{\boldsymbol{k},\alpha} f_{\alpha}^{\boldsymbol{k}} \Phi_{\alpha}^{\boldsymbol{k}\dagger}\left(\boldsymbol{r}\right) \Phi_{\alpha}^{\boldsymbol{k}}\left(\boldsymbol{r}\right), \tag{4.8}$$

$$\boldsymbol{m}\left(\boldsymbol{r}\right) = \frac{1}{N_k} \sum_{\boldsymbol{k},\alpha} f_{\alpha}^{\boldsymbol{k}} \Phi_{\alpha}^{\boldsymbol{k}\dagger}\left(\boldsymbol{r}\right) \boldsymbol{\sigma} \Phi_{\alpha}^{\boldsymbol{k}}\left(\boldsymbol{r}\right), \tag{4.9}$$

with the number of $\boldsymbol{k}$-points $N_{\boldsymbol{k}}$ and the ultra long-range occupation numbers $f_{\alpha}^{\boldsymbol{k}}$ associated with the orbitals $\Phi_{\alpha}^{\boldsymbol{k}}$. The charge and magnetization densities obtained

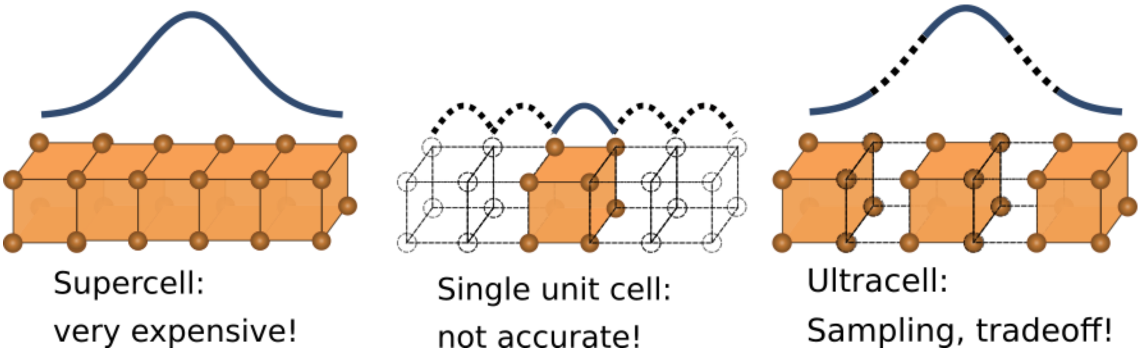

Figure 4.2
A simplified real space picture of the ultra cell. A supercell is very expensive for large systems and a single, lattice periodic unit cell can lead to loss of physical features. The ultra cell approach allows for sampling only a subset of the total system which is considered. An arbitrary number of unit cells can be left out in between.

from this wave function take the form

$$n\left(\boldsymbol{r}\right)=\sum_{\boldsymbol{Q}} n_{\boldsymbol{Q}}\left(\boldsymbol{r}\right)e^{i\boldsymbol{Q}\cdot\boldsymbol{r}},\quad \boldsymbol{m}\left(\boldsymbol{r}\right)=\sum_{\boldsymbol{Q}} \boldsymbol{m}_{\boldsymbol{Q}}\left(\boldsymbol{r}\right)e^{i\boldsymbol{Q}\cdot\boldsymbol{r}}, \tag{4.10}$$

with $\boldsymbol{Q}=\boldsymbol{\kappa}-\boldsymbol{\kappa}'$. The partial densities $n_{\boldsymbol{Q}}, \boldsymbol{m}_{\boldsymbol{Q}}$ in eq. 4.10 are generally complex and act as lattice-periodic Fourier coefficients. The resulting total densities $n, \boldsymbol{m}$ are real functions, which, depending on the values of $\boldsymbol{Q}$, will have a periodicity far larger than the length scale of a unit cell (fig. 4.1b). By adjusting the underlying $\boldsymbol{\kappa}$-lattice, it is therefore possible to change the $\boldsymbol{Q}$-vectors and hence allow for variations of arbitrary length in the system. The $\boldsymbol{Q}=0$ term deserves special mention, as it corresponds to the full lattice periodic solution. We emphasize that there is no restriction on the magnitude of $n_{\boldsymbol{Q}}, \boldsymbol{m}_{\boldsymbol{Q}}$ and we are thus able to expand arbitrary modulations in the charge and magnetization densities. This is a key difference compared to the spin-spiral ansatz [75, 76]. The Fourier coefficients $n_{\boldsymbol{Q}}, \boldsymbol{m}_{\boldsymbol{Q}}$ can be calculated efficiently by first calculating the wave function (eq. 4.7) for a subset of unit cells, given by a set of real-space lattice vectors $\{\boldsymbol{R}_i\}$. We choose the $\boldsymbol{R}_i$-vectors to be the conjugated real-space vectors of the $\boldsymbol{Q}$-vectors. The wave function in a single unit cell is then given by a sum over the states j and a Fourier transform in $\boldsymbol{\kappa}$ of the coefficients $c^{\alpha}_{j\boldsymbol{k}+\boldsymbol{\kappa}}$:

$$\Phi^{\boldsymbol{k}}_{\alpha}\left(\boldsymbol{r}+\boldsymbol{R}_i\right)\approx\sum_j \begin{pmatrix} u^{\uparrow}_{j\boldsymbol{k}}\left(\boldsymbol{r}\right) \\ u^{\downarrow}_{j\boldsymbol{k}}\left(\boldsymbol{r}\right)\end{pmatrix}\sum_{\boldsymbol{\kappa}} c^{\alpha}_{j\boldsymbol{k}+\boldsymbol{\kappa}}e^{i\boldsymbol{\kappa}\cdot\boldsymbol{R}_i} \tag{4.11}$$

where $\boldsymbol{r}$ is restricted to a single unit cell and we have assumed that $|\boldsymbol{\kappa}\cdot\boldsymbol{r}|\ll 1$, which is typically fulfilled for large systems. From this we compute a set of charge and magnetization densities on the same grid, i.e. $n_i=n\left(\boldsymbol{r}+\boldsymbol{R}_i\right), \boldsymbol{m}_i=\boldsymbol{m}\left(\boldsymbol{r}+\boldsymbol{R}_i\right)$. This set can then be partially Fourier transformed to reciprocal space to obtain

$n_{\boldsymbol{Q}}(\boldsymbol{r}), \boldsymbol{m}_{\boldsymbol{Q}}(\boldsymbol{r})$:

$$n_{\boldsymbol{Q}}(\boldsymbol{r}) = \frac{1}{N_{\boldsymbol{R}}} \sum_i n(\boldsymbol{r} + \boldsymbol{R}_i) e^{-i\boldsymbol{Q}\cdot\boldsymbol{R}_i}, \boldsymbol{m}_{\boldsymbol{Q}}(\boldsymbol{r}) = \frac{1}{N_{\boldsymbol{R}}} \sum_i \boldsymbol{m}(\boldsymbol{r} + \boldsymbol{R}_i) e^{-i\boldsymbol{Q}\cdot\boldsymbol{R}_i}. \quad (4.12)$$

Here $N_{\boldsymbol{R}}$ denotes the number of $\boldsymbol{R}$-vectors chosen. With the definition of $\boldsymbol{R}$, it is illustrative to think about the ULR ansatz in a real-space picture: Our ansatz corresponds to a sampling of unit cells in real space, followed by a Fourier interpolation between the sampled cells (fig. 4.2). With the densities at hand, we will now focus on generalizing the Hamiltonian such that meaningful, non-trivial values for the expansion coefficients $c^{\alpha}_{j\boldsymbol{k}+\boldsymbol{\kappa}}$ (eq. 4.7) are obtained.

4.2.2 Ultra long-range Hamiltonian

Our ULR Hamiltonian retains the full lattice periodic KS Hamiltonian $\hat{H}_0$ (eq. 4.6) but has an added, additional “modulation” Hamiltonian

$$\hat{H} = \hat{H}_0 + \sum_{\boldsymbol{Q}\neq 0} \hat{H}_{\boldsymbol{Q}}(\boldsymbol{r}) e^{i\boldsymbol{Q}\cdot\boldsymbol{r}} \equiv \hat{H}_0 + \hat{H}_{\boldsymbol{Q}\neq 0}, \quad (4.13)$$

where we introduced the general notation $O_{\boldsymbol{Q}\neq 0} \equiv \sum_{\boldsymbol{Q}\neq 0} O_{\boldsymbol{Q}}(\boldsymbol{r}) e^{i\boldsymbol{Q}\cdot\boldsymbol{r}}$. The total Hamiltonian $\hat{H}$ is thus decomposed in the same way as the charge and magnetization densities (eq. 4.10). For a KS system like eq. 4.6, our “modulation”-Hamiltonian reads

$$\hat{H}_{\boldsymbol{Q}\neq 0} = \sum_{\boldsymbol{Q}\neq 0} e^{i\boldsymbol{Q}\cdot\boldsymbol{r}} \Big[v_{\boldsymbol{Q}}(\boldsymbol{r}) + \mu_B \boldsymbol{B}_{\boldsymbol{Q}}(\boldsymbol{r}) \cdot \boldsymbol{\sigma} + 2i\mu_B \left(\boldsymbol{A}^{\text{ext}}_{\boldsymbol{Q}}(\boldsymbol{r}) \cdot \boldsymbol{\nabla} \right) + 2\mu_B^2 \tilde{A}_{\boldsymbol{Q}}(\boldsymbol{r}) \Big], \quad (4.14)$$

$v_{\boldsymbol{Q}}(\boldsymbol{r}), \boldsymbol{B}_{\boldsymbol{Q}}(\boldsymbol{r}), \boldsymbol{A}^{\text{ext}}_{\boldsymbol{Q}}(\boldsymbol{r}), \tilde{A}_{\boldsymbol{Q}}(\boldsymbol{r})$ are again complex, lattice periodic Fourier coefficients and contribute to long-ranged versions of the scalar potential, the magnetic field and the vector potential, respectively. In the following we will discuss these coefficients and how to compute them in more detail. We will start with the scalar potential, which can again be decomposed into a Hartree potential $v^{\text{H}}_{\boldsymbol{Q}}(\boldsymbol{r})$ an XC-potential $v^{\text{xc}}_{\boldsymbol{Q}}(\boldsymbol{r})$ and an external potential $v^{\text{ext}}_{\boldsymbol{Q}}(\boldsymbol{r})$. The coefficients for the ULR Hartree potential $v^{\text{H}}_{\boldsymbol{Q}}(\boldsymbol{r})$ are obtained by evaluating the Hartree potential for the long-range density $n(\boldsymbol{r})$ (eq. 4.10):

$$v^{\text{H}}_{\boldsymbol{Q}\neq 0}(\boldsymbol{r}) = \sum_{\boldsymbol{Q}\neq 0} e^{i\boldsymbol{Q}\cdot\boldsymbol{r}} \int d^3r' \frac{n_{\boldsymbol{Q}}(\boldsymbol{r'})}{|\boldsymbol{r} - \boldsymbol{r'}|} e^{-i\boldsymbol{Q}\cdot(\boldsymbol{r}-\boldsymbol{r'})} = \sum_{\boldsymbol{Q}\neq 0} v^{\text{H}}_{\boldsymbol{Q}}(\boldsymbol{r}) e^{i\boldsymbol{Q}\cdot\boldsymbol{r}}. \quad (4.15)$$

The coefficients associated with the XC-interaction $v^{\text{xc}}_{\boldsymbol{Q}}(\boldsymbol{r})$ cannot be directly obtained from $n_{\boldsymbol{Q}}(\boldsymbol{r})$. The main difference compared to the Hartree potential is that the XC-functional is inherently non-linear, therefore the naive approach $v^{\text{xc}}_{\boldsymbol{Q}}(\boldsymbol{r}) = v^{\text{xc}}[n_{\boldsymbol{Q}}]$ may introduce a mixing of the real and imaginary part of $n_{\boldsymbol{Q}}$. We will therefore evaluate the XC-potential for each $\boldsymbol{R}$-vector individually followed by a Fourier transform to $\boldsymbol{Q}$-space to obtain $v^{\text{XC}}_{\boldsymbol{Q}}(\boldsymbol{r})$:

$$v^{\text{XC}}_{\boldsymbol{Q}}(\boldsymbol{r}) = \frac{1}{N_{\boldsymbol{R}}} \sum_i v^{\text{xc}}[n](\boldsymbol{r} + \boldsymbol{R}_i) e^{-i\boldsymbol{Q}\cdot\boldsymbol{R}_i}. \quad (4.16)$$

It is worth noting that defining the long-range XC-functional this way does not change how local an XC-functional inherently is, it is merely a Fourier interpolation. Lastly, $v_{\boldsymbol{Q}}^{\text{ext}}\left(\boldsymbol{r}\right)$ are the coefficients of an external, long-ranged potential and can be freely chosen. While our current method assumes a lattice-periodic underlying system, changes to the electrostatic potential due to a shift in the nuclei can be expanded and added perturbatively to $v_{\boldsymbol{Q}}^{\text{ext}}\left(\boldsymbol{r}\right)$.

The magnetic field $\boldsymbol{B}^{\boldsymbol{Q}}\left(\boldsymbol{r}\right)$ in eq. 4.14 consists of an external field, an XC-field and a dipole-dipole field:

$$\boldsymbol{B}_{\boldsymbol{Q}}\left(\boldsymbol{r}\right) = \boldsymbol{B}_{\boldsymbol{Q}}^{\text{ext}}\left(\boldsymbol{r}\right) + \boldsymbol{B}_{\boldsymbol{Q}}^{\text{XC}}\left(\boldsymbol{r}\right) + \boldsymbol{B}_{\boldsymbol{Q}}^{\text{D}}\left(\boldsymbol{r}\right). \tag{4.17}$$

Again, the external magnetic field may be chosen arbitrarily and the XC-field can be computed analogously to the XC-potential:

$$\boldsymbol{B}_{\boldsymbol{Q}}^{\text{XC}}\left(\boldsymbol{r}\right) = \frac{1}{N_{\boldsymbol{R}}}\sum_{i}\boldsymbol{B}^{\text{XC}}\left[n,\boldsymbol{m}\right]\left(\boldsymbol{r}+\boldsymbol{R}_i\right)e^{-i\boldsymbol{Q}\cdot\boldsymbol{R}_i}. \tag{4.18}$$

The last term corresponds to the magnetic field associated with the MDI:

$$\boldsymbol{B}_{\boldsymbol{Q}}^{\text{D}}\left(\boldsymbol{r}\right) = -\mu_B\int d^3r'\frac{3\left(\boldsymbol{m}_{\boldsymbol{Q}}\left(\boldsymbol{r'}\right)\cdot\boldsymbol{e}_{\boldsymbol{r},\boldsymbol{r'}}\right)\boldsymbol{e}_{\boldsymbol{r},\boldsymbol{r'}} - \boldsymbol{m}_{\boldsymbol{Q}}\left(\boldsymbol{r'}\right)}{\left|\boldsymbol{r}-\boldsymbol{r'}\right|^3}e^{-i\boldsymbol{Q}\left(\boldsymbol{r}-\boldsymbol{r'}\right)} - 8\pi\mu_B\boldsymbol{m}_{\boldsymbol{Q}}\left(\boldsymbol{r}\right), \tag{4.19}$$

which is a long-ranged version of eq. 4.3 and should therefore contribute to non-trivial magnetic order. Similarly to the Coulomb interaction, we expect also an exchange contribution arising from the MDI. We derive a truly non-local exchange functional for the MDI in chapter 5.

Finally, $\boldsymbol{A}_{\boldsymbol{Q}}^{\text{ext}}\left(\boldsymbol{r}\right), \tilde{A}_{\boldsymbol{Q}}\left(\boldsymbol{r}\right)$ in eq. 4.14 are the contributions of a vector potential in the Coulomb gauge. $\tilde{A}_{\boldsymbol{Q}}\left(\boldsymbol{r}\right)$ corresponds to the term arising due to the square of the vector potential. As this term is also non-linear, it should be evaluated in real-space first as well:

$$\tilde{A}_{\boldsymbol{Q}}\left(\boldsymbol{r}\right) = \frac{1}{N_{\boldsymbol{R}}}\sum_{i}\left(\boldsymbol{A}_{\text{ext}}\left(\boldsymbol{r}+\boldsymbol{R}_i\right)\right)^2 e^{-i\boldsymbol{Q}\cdot\boldsymbol{R}_i}. \tag{4.20}$$

While this makes it possible to treat the vector potential fully non-perturbatively, we note that the term $2\mu_B^2\boldsymbol{A}^2\left(\boldsymbol{r}\right)$ is commonly neglected in calculations as it is typically small in comparison with the term $2\mu_B\boldsymbol{A}\left(\boldsymbol{r}\right)\cdot\nabla$.

We conclude with a remark on the kinetic energy. The kinetic energy operator $\hat{\boldsymbol{p}}^2/2$ does not explicitly depend on the periodicity of the problem at hand. As the kinetic energy operator is already included in $\hat{H}_0$ (eqs. 4.6,4.13), it should not be included in $\hat{H}_{\boldsymbol{Q}\neq 0}$ (eq. 4.14) again. It is important to note, however, that the kinetic energy is sensitive to the shifts in reciprocal space of the wave function (eq. 4.7) $\boldsymbol{k}\rightarrow\boldsymbol{k}+\boldsymbol{\kappa}$. The total kinetic energy in the long range system $\hat{H}$ is thus generally different than the total kinetic energy in the lattice periodic system $\hat{H}_0$.

4.2.3 Hamiltonian Matrix Elements

Our goal is to diagonalize the full Hamiltonian (eq. 4.13) which consists of a lattice-periodic part and a modulation part. For that we compute the matrix elements for a fixed $\boldsymbol{k}$-point in the basis $c^{\alpha}_{j\boldsymbol{k}+\boldsymbol{\kappa}} = \delta_{\alpha,j\boldsymbol{\kappa}}$, i.e. we use the orbitals

$$\varphi_{j\boldsymbol{k}}\left(\boldsymbol{r}\right) = \frac{1}{\sqrt{N_u}} \begin{pmatrix} u^{\uparrow}_{j\boldsymbol{k}}\left(\boldsymbol{r}\right) \\ u^{\downarrow}_{j\boldsymbol{k}}\left(\boldsymbol{r}\right) \end{pmatrix} e^{i(\boldsymbol{k}+\boldsymbol{\kappa})\cdot\boldsymbol{r}} \tag{4.21}$$

to evaluate

$$\left\langle\varphi_{j\boldsymbol{k}}\right| \hat{H}_0 + \hat{H}_{\boldsymbol{Q}\neq 0} \left|\varphi_{j'\boldsymbol{k}}\right\rangle = \delta_{\kappa\kappa'} \left(O^{\dagger}_{\boldsymbol{k}+\boldsymbol{\kappa},\boldsymbol{k}} \epsilon^0_{\boldsymbol{k}} O_{\boldsymbol{k}+\boldsymbol{\kappa},\boldsymbol{k}}\right)_{jj'} + \left\langle\varphi_{j\boldsymbol{k}}\right| \hat{H}_{\boldsymbol{Q}\neq 0} \left|\varphi_{j'\boldsymbol{k}}\right\rangle . \tag{4.22}$$

Here $\epsilon^0_{\boldsymbol{k}+\boldsymbol{\kappa}}$ is the diagonal matrix of eigenvalues of $\hat{H}_0$ at $\boldsymbol{k}+\boldsymbol{\kappa}$ and $O_{\boldsymbol{k}+\boldsymbol{\kappa},\boldsymbol{k}}$ is the unitary overlap matrix between the orbitals at $\boldsymbol{k}$ and $\boldsymbol{k}+\boldsymbol{\kappa}$, i.e.

$$\left(O_{\boldsymbol{k}+\boldsymbol{\kappa},\boldsymbol{\kappa}}\right)_{jj'} = \sum_s \int \mathrm{d}\boldsymbol{r}\, u^{*}_{sj\boldsymbol{k}+\boldsymbol{\kappa}}\left(\boldsymbol{r}\right) e^{-i\boldsymbol{\kappa}\cdot\boldsymbol{r}} u_{sj'\boldsymbol{k}}\left(\boldsymbol{r}\right), \tag{4.23}$$

where $s = \uparrow, \downarrow$ is a spin index. This overlap matrix is required because our chosen basis is the set of orbitals at $\boldsymbol{k}$ and not those at $\boldsymbol{k}+\boldsymbol{\kappa}$. The overlap matrix $O_{\boldsymbol{k}+\boldsymbol{\kappa},\boldsymbol{\kappa}}$ may however not be strictly unitary. This may be due to the basis being finite or numerical inaccuracies. As unitarity is necessary for preserving the eigenvalues $\epsilon^0_{\boldsymbol{k}+\boldsymbol{\kappa}}$, we ensure this by first performing a singular value decomposition $O_{\boldsymbol{k}+\boldsymbol{\kappa},\boldsymbol{\kappa}} = U\Sigma T^{\dagger}$ and then making the substitution $O_{\boldsymbol{k}+\boldsymbol{\kappa},\boldsymbol{\kappa}} \to UT^{\dagger}$. It is possible to show that this new matrix is the closest - in the sense of the Frobenius norm - unitary matrix to the original [79].

What remains to be done is the calculation of the matrix elements of $\hat{H}_{\boldsymbol{Q}\neq 0}$ (eq. 4.14). We start with the the scalar potential and find:

$$\begin{aligned}
\left\langle\varphi_{j\boldsymbol{k}}\right| v_{\boldsymbol{Q}\neq 0} \left|\varphi_{j'\boldsymbol{k}}\right\rangle &= \sum_s \frac{1}{N_u} \int_{\text{ultra}} d^3r\, u^{*}_{js\boldsymbol{k}}\left(\boldsymbol{r}\right) e^{-i\boldsymbol{Q}'\cdot\boldsymbol{r}} v_{\boldsymbol{Q}\neq 0}\left(\boldsymbol{r}\right) u_{j's\boldsymbol{k}}\left(\boldsymbol{r}\right) \\
&= \sum_s \frac{1}{N_u} \int_{\text{unit}} \mathrm{d}^3r \sum_{\boldsymbol{R}_u} u^{*}_{js\boldsymbol{k}}\left(\boldsymbol{r}\right) u_{j's\boldsymbol{k}}\left(\boldsymbol{r}\right) e^{-i\boldsymbol{Q}'(\boldsymbol{r}+\boldsymbol{R}_u)} \\
&\qquad\qquad \times \sum_{\boldsymbol{Q}} v_{\boldsymbol{Q}}\left(\boldsymbol{r}\right) e^{i\boldsymbol{Q}(\boldsymbol{r}+\boldsymbol{R}_u)} \\
&= \sum_s \int_{\text{unit}} \mathrm{d}^3r\, u^{*}_{js\boldsymbol{k}}\left(\boldsymbol{r}\right) u_{j's\boldsymbol{k}}\left(\boldsymbol{r}\right) v_{\boldsymbol{Q}}\left(\boldsymbol{r}\right).
\end{aligned} \tag{4.24}$$

In the first step we converted the integral over the ultra cell into an integral over a unit cell and a sum over all unit cells in the ultra cell $\int_{\text{ultra}} \mathrm{d}^3r \to \int_{\text{unit}} \mathrm{d}^3r \sum_{\boldsymbol{R}_u}$ and made use of the lattice periodicity of $u_{j\boldsymbol{k}}\left(\boldsymbol{r}\right)$. In the second step we then carried out the sum over $\boldsymbol{R}_u$ followed by the sum over $\boldsymbol{Q}$. The matrix elements for the ultra cell can thus be expressed by a simple unit cell integration. Similarly we find for the magnetic field contribution:

$$\begin{aligned}
\left\langle\varphi_{j\boldsymbol{k}}\right| \boldsymbol{B}_{\boldsymbol{Q}\neq 0} \cdot \boldsymbol{\sigma} \left|\varphi_{j'\boldsymbol{k}}\right\rangle = \int_{\text{unit}} \mathrm{d}^3r\, & u^{*}_{\uparrow j\boldsymbol{k}}\left(\boldsymbol{r}\right) u_{\downarrow j'\boldsymbol{k}}\left(\boldsymbol{r}\right) \left(B^{x}_{\boldsymbol{Q}}\left(\boldsymbol{r}\right) - iB^{y}_{\boldsymbol{Q}}\left(\boldsymbol{r}\right)\right) \\
&+ u^{*}_{\downarrow j\boldsymbol{k}}\left(\boldsymbol{r}\right) u_{\uparrow j'\boldsymbol{k}}\left(\boldsymbol{r}\right) \left(B^{x}_{\boldsymbol{Q}}\left(\boldsymbol{r}\right) + iB^{y}_{\boldsymbol{Q}}\left(\boldsymbol{r}\right)\right) \\
&+ \left(u^{*}_{\uparrow j\boldsymbol{k}}\left(\boldsymbol{r}\right) u_{\uparrow j'\boldsymbol{k}}\left(\boldsymbol{r}\right) - u^{*}_{\downarrow j\boldsymbol{k}}\left(\boldsymbol{r}\right) u_{\downarrow j'\boldsymbol{k}}\left(\boldsymbol{r}\right)\right) B^{z}_{\boldsymbol{Q}}\left(\boldsymbol{r}\right).
\end{aligned} \tag{4.25}$$

And finally we have for the vector potential:

$$\langle\varphi_{j\boldsymbol{k}}|\sum_{\boldsymbol{Q}}\frac{i}{c}\left(\boldsymbol{A}^{\mathrm{ext}}_{\boldsymbol{Q}}\left(\boldsymbol{r}\right)\cdot\boldsymbol{\nabla}\right)+\frac{1}{2c^2}\tilde{A}_{\boldsymbol{Q}}\left(\boldsymbol{r}\right)|\varphi_{j'\boldsymbol{k}}\rangle=\frac{1}{c}\sum_s\int_{unit}\mathrm{d}^3r\;u^*_{sj\boldsymbol{k}}\left(\boldsymbol{r}\right)$$
$$\times\left[i\boldsymbol{A}^{\mathrm{ext}}_{\boldsymbol{Q}}\left(\boldsymbol{r}\right)\cdot\boldsymbol{\nabla}-\boldsymbol{A}^{\mathrm{ext}}_{\boldsymbol{Q}}\left(\boldsymbol{r}\right)\cdot\left(\boldsymbol{k}+\boldsymbol{\kappa}'\right)+\frac{1}{2c}\tilde{A}_{\boldsymbol{Q}}\left(\boldsymbol{r}\right)\right]u_{sj'\boldsymbol{k}}\left(\boldsymbol{r}\right). \tag{4.26}$$

4.3 Numerical implementation

In this section we will address how to implement the ultra long-range ansatz in practice. The discussions in this section are based on our implementation in the ELK electronic structure code [38].

4.3.1 Self-consistent solution

$\hat{H}$ (eq. 4.13) is a KS system in which the potentials are functionals of the partial densities $n_{\boldsymbol{Q}}\left(\boldsymbol{r}\right),\boldsymbol{m}_{\boldsymbol{Q}}\left(\boldsymbol{r}\right)$ (eq. 4.12) which in turn depend on the orbitals $\Phi^{\boldsymbol{k}}_{\alpha}\left(\boldsymbol{r}\right)$ (eq. 4.7). eq. 4.13 thus needs to be solved self-consistently. We employ an iteration scheme as it is usually done when solving KS systems:

1. Solve the lattice periodic ground state (eq. 4.6) and obtain the spinor orbitals $\begin{pmatrix}u^{\uparrow}_{j\boldsymbol{k}}\left(\boldsymbol{r}\right)\\u^{\downarrow}_{j\boldsymbol{k}}\left(\boldsymbol{r}\right)\end{pmatrix}$ as well as all eigenenergies $\epsilon^0_{j\boldsymbol{k}+\boldsymbol{\kappa}}$ associated with the $\boldsymbol{k}+\boldsymbol{\kappa}$-points.
2. Initialize the external long-range potentials via $v_{\boldsymbol{Q}},\boldsymbol{B}_{\boldsymbol{Q}},\boldsymbol{A}_{\boldsymbol{Q}}$ and the occupation numbers $f^{\boldsymbol{k}}_{\alpha}$.
3. (a) Compute the matrix elements of $\hat{H}_{\boldsymbol{Q}\neq 0}$ (eq. 4.14). Diagonalize $\hat{H}$ (eq. 4.13) to obtain the expansion coefficients $c^{\alpha}_{j\boldsymbol{k}+\boldsymbol{\kappa}}$ as well as the long-range eigenenergies $\epsilon^{\boldsymbol{k}}_{\alpha}$.
   (b) Concurrently with the step above, construct the long-range densities $n_{\boldsymbol{Q}}\left(\boldsymbol{r}\right)$ and $\boldsymbol{m}_{\boldsymbol{Q}}\left(\boldsymbol{r}\right)$ (eq. 4.12).
4. Calculate the new occupation numbers $f^{\boldsymbol{k}}_{\alpha}$.
5. Calculate new long-range potentials $v'_{\boldsymbol{Q}},\boldsymbol{B}'_{\boldsymbol{Q}},\boldsymbol{A}'_{\boldsymbol{Q}}$. Mix the new potentials with the potentials from the previous iteration. Monitor the relative change in the potentials.
6. Repeat steps 3 to 5 until the change in the potentials is sufficiently small.

We will discuss two steps in this self-consistent cycle in more detail. First we will explain why we calculate the energies $\epsilon^{\boldsymbol{k}}_{\alpha}$ and densities $n_{\boldsymbol{Q}}\left(\boldsymbol{r}\right),\boldsymbol{m}_{\boldsymbol{Q}}\left(\boldsymbol{r}\right)$ before the occupation numbers $f^{\boldsymbol{k}}_{\alpha}$. This seems counterintuitive, as the densities depend on the occupation numbers (eqs. 4.8,4.9). However, as we are performing a self-consistent cycle, the occupation numbers will converge to the correct value as self-consistency is achieved. Computing the occupation numbers last enables us to parallelize step 3 over the $\boldsymbol{k}$-point set in a single loop: For each $\boldsymbol{k}$-point, we diagonalize $\hat{H}^{\boldsymbol{k}} = \hat{H}_0^{\boldsymbol{k}} + \hat{H}_{\boldsymbol{Q}\neq 0}^{\boldsymbol{k}}$ and compute $n_{\boldsymbol{Q}}^{\boldsymbol{k}}(\boldsymbol{r}), \boldsymbol{m}_{\boldsymbol{Q}}^{\boldsymbol{k}}(\boldsymbol{r})$. Afterwards we carry out the $\boldsymbol{k}$-point sum over $n_{\boldsymbol{Q}}^{\boldsymbol{k}}(\boldsymbol{r}), \boldsymbol{m}_{\boldsymbol{Q}}^{\boldsymbol{k}}(\boldsymbol{r})$ to obtain $n_{\boldsymbol{Q}}(\boldsymbol{r}), \boldsymbol{m}_{\boldsymbol{Q}}(\boldsymbol{r})$. The central computational gain is that this ordering is much less demanding when it comes to memory: The expansion coefficients $c_{j\boldsymbol{k}+\boldsymbol{\kappa}}^{\alpha}$ no longer have to be stored but can be calculated and used on-the-fly instead.

Second, we note that some care has to be taken during the mixing, as only the coefficients $v_{\boldsymbol{Q}}(\boldsymbol{r})$, $\boldsymbol{B}_{\boldsymbol{Q}}(\boldsymbol{r}), \boldsymbol{A}_{\boldsymbol{Q}}(\boldsymbol{r})$ of a Fourier series are mixed. These coefficients are generally complex and are not subject to the same constraints as the actual real-space densities. We also want to emphasize that in a typical calculation a rather slow mixing should be applied. The Coulomb interaction in a large system will react very strongly to any external perturbation because of the $1/Q^2$ divergence, which can lead to substantial charge sloshing during convergence. This is an aspect of the method which would benefit from further investigation and improvement. One idea is to start with a screened Coulomb interaction to remove the divergence. During the self-consistent loop, the screening could then be slowly reduced to zero.

4.3.2 Efficient k-space grids

The underlying grids have to be carefully chosen in order to avoid computational artifacts and to achieve a most efficient calculation. Ideally, the distance between $\boldsymbol{k}$-points should be much bigger than the distance between $\boldsymbol{\kappa}$-points, $|\boldsymbol{k} - \boldsymbol{k}'| \gg |\boldsymbol{\kappa} - \boldsymbol{\kappa}'|$. This will ensure that the set $\boldsymbol{k} + \boldsymbol{\kappa}$ does not overlap for any two $\boldsymbol{k}$-points, which may lead to double counting and an overcomplete basis set. Physically speaking, the length scales in the system should be well separated, i.e. the modulation should be far larger than the size of a unit cell. If $|\boldsymbol{k} - \boldsymbol{k}'| \approx |\boldsymbol{\kappa} - \boldsymbol{\kappa}'|$, however, the system tends to have a size which can and should be solved with a supercell instead.

During a self-consistent iteration Fourier transformations need to be carried out multiple times: In $e^{i\boldsymbol{\kappa}\cdot\boldsymbol{R}_i}$ when calculating the wave function (eq. 4.11) and in $e^{-i\boldsymbol{Q}\cdot\boldsymbol{R}}$ when calculating the densities (eqs. 4.8, 4.9), the XC-potential and -field (eq. 4.16, 4.18) and the vector potential (eq. 4.20). For the computational performance it is therefore highly beneficial to carry out all Fourier transformations via a Fast Fourier Transform (FFT). This requires the underlying grid to be FFT compatible (having radices $2, 3, 5$ and 7 in our case). Due to $\boldsymbol{Q} = \boldsymbol{\kappa} - \boldsymbol{\kappa}'$ the $\boldsymbol{Q}$-point grid and the $\boldsymbol{\kappa}$-point grid are dependent on each other. The number of $\boldsymbol{Q}$-points $N_{\boldsymbol{Q}}$ along a given direction i is $N_{\boldsymbol{Q}}^i = 2N_{\boldsymbol{\kappa}}^i - 1$. In our implementation, we ensure that the input $\boldsymbol{Q}$-grid snaps to the next FFT compatible grid. We then choose the $\boldsymbol{\kappa}$-point grid such that $2N_{\boldsymbol{\kappa}}^i - 1 \leq N_{\boldsymbol{Q}}^i$. This grid choice can sometimes result in unmatched $\boldsymbol{Q}$-points, e.g. if $N_{\boldsymbol{Q}} = 20, N_{\boldsymbol{\kappa}} = 10$, the $\boldsymbol{Q}$-vectors are not symmetric around zero. While the unmatched $\boldsymbol{Q}$-point is "dead-weight" and remains zero throughout the calculation, the speed up obtained by using a FFT outweighs having additional $\boldsymbol{Q}$-points.

4.3.3 Computation of the Hartree and dipole interaction

We will briefly address how to calculate the complex integrals appearing in the scalar potential (eq. 4.15) and the magnetic dipole field (eq. 4.19). When computing the Hartree-potential (eq. 4.15, i.e. solving Poisson's equation), the integral may be performed efficiently by further Fourier transforming $n_{\boldsymbol{Q}}(\boldsymbol{r})$ to $n_{\boldsymbol{Q}}(\boldsymbol{G})$, where $\boldsymbol{G}$ is a reciprocal lattice vector (eq. 2.81). The Hartree potential is then determined directly via $V^{\mathrm{H}}_{\boldsymbol{Q}}(\boldsymbol{G}) = 4\pi n_{\boldsymbol{Q}}(\boldsymbol{G}) / |\boldsymbol{G}+\boldsymbol{Q}|^2$ and can be subsequently Fourier transformed back to real-space. This is easily extended to the case of the APW basis by using the method of Weinert [78].

The magnetic dipole field can be solved for in a similar way by evaluating Poisson's equation component-wise for the vector potential. From classical electrodynamics we now that the vector potential associated with a magnetization is given by:

$$\boldsymbol{A}^{\mathrm{dip}}(\boldsymbol{r}) = \mu_B \int \mathrm{d}\boldsymbol{r}' \frac{\nabla \times \boldsymbol{m}(\boldsymbol{r}')}{|\boldsymbol{r}-\boldsymbol{r}'|}. \tag{4.27}$$

We partially Fourier transform both sides and obtain:

$$\sum_{\boldsymbol{Q}} \boldsymbol{A}^{\mathrm{dip}}_{\boldsymbol{Q}}(\boldsymbol{r})\, e^{i\boldsymbol{Q}\cdot\boldsymbol{r}} = \mu_B \int \mathrm{d}\boldsymbol{r}' \frac{\nabla \times \sum_{\boldsymbol{Q}} \boldsymbol{m}_{\boldsymbol{Q}}(\boldsymbol{r}')\, e^{i\boldsymbol{Q}\cdot\boldsymbol{r}'}}{|\boldsymbol{r}-\boldsymbol{r}'|}. \tag{4.28}$$

We thus have for the coefficients of the vector potential:

$$A^{\mathrm{dip}}_{\boldsymbol{Q},j}(\boldsymbol{r}) = \mu_B \sum_{kl} \epsilon_{jkl} \int \mathrm{d}\boldsymbol{r}' e^{-i\boldsymbol{Q}\cdot(\boldsymbol{r}-\boldsymbol{r}')} \frac{\partial_k m_{\boldsymbol{Q},l}(\boldsymbol{r}') + iQ_k m_{\boldsymbol{Q},l}(\boldsymbol{r}')}{|\boldsymbol{r}-\boldsymbol{r}'|}. \tag{4.29}$$

Here j,k,l indicate vector components and ϵ_{jkl} is the Levi-Civita symbol. The coefficients $\boldsymbol{A}^{\mathrm{dip}}_{\boldsymbol{Q}}(\boldsymbol{r})$ now have the same form as the Hartree potential (eq. 4.15) and can also be computed by a complex version of Weinert's method [78]. From this it is easy to obtain the magnetic field of the dipole interaction via $\boldsymbol{B}^{\mathrm{dip}}(\boldsymbol{r}) = \nabla \times \boldsymbol{A}^{\mathrm{dip}}(\boldsymbol{r})$. We find for the coefficients:

$$B^{\mathrm{dip}}_{\boldsymbol{Q},j} = \sum_{kl} \epsilon_{jkl} \left[\partial_k A^{\mathrm{dip}}_{\boldsymbol{Q},l}(\boldsymbol{r}) + iQ_k A^{\mathrm{dip}}_{\boldsymbol{Q},l}(\boldsymbol{r})\right]. \tag{4.30}$$

We point out that if we were to consider an exact theory for the current density, the dipole vector potential (eq. 4.27) should be added to the total vector potential, corresponding to a Lorentz force generated by the MDI.

4.4 Ultra long-range results

In this section, we will present several calculations to benchmark our ultra long-range approach for both, accuracy and efficiency. We will start with two purely electrostatic calculations and conclude with two magnetic examples, spin spirals in γ-Fe and a spin-density wave in Cr.

4.4.1 Sawtooth potential in Silicon

In our first benchmark, we directly compare the results from an ultracell (UC) and a supercell (SC). Our system consists of 20 unit cells of bulk Si subjected to an external sawtooth potential applied along the (110) direction. For the SC we use 1x4x4 $\boldsymbol{k}$-points, 10 empty states per atom and expand the sawtooth microscopically with 750 $\boldsymbol{G}$-vectors (cf. section 2.5) along the direction of the electric field. For the UC we use 4x4x4 normal $\boldsymbol{k}$-points, a two-atomic basis and 10x1x1 $\boldsymbol{\kappa}$-points corresponding to 20x1x1 $\boldsymbol{Q}$-vectors (i.e. we employ the maximum of one $\boldsymbol{Q}$-point per unit cell). We use 60 empty states for both atoms in our atomic basis in order to obtain a large ultra long-range basis set. In the UC, we expand the external sawtooth potential in the coarse $\boldsymbol{Q}$-points. The potential for both, the SC and the UC is shown in fig. 4.3a. The potential is much closer to a real sawtooth in the SC, due to the larger number of basis functions. In fig. 4.3b, we show the resulting self-consistent density for the SC and the UC, plotted along the (110) direction. The plotting axis is slightly offset relative to the atomic positions to avoid numerical spikes in the plot. We observe very good agreement at the center and larger deviations at the edges, which can mostly be attributed to the difference in the potentials. In both cases, the external potential is screened, resulting in a seemingly periodic density in the center. Our results show that our ultra long-range approach is reasonably accurate already for a small $\boldsymbol{Q}$-point set. We expect an even better agreement for larger systems where we can employ more $\boldsymbol{Q}$-points to sample the potential.

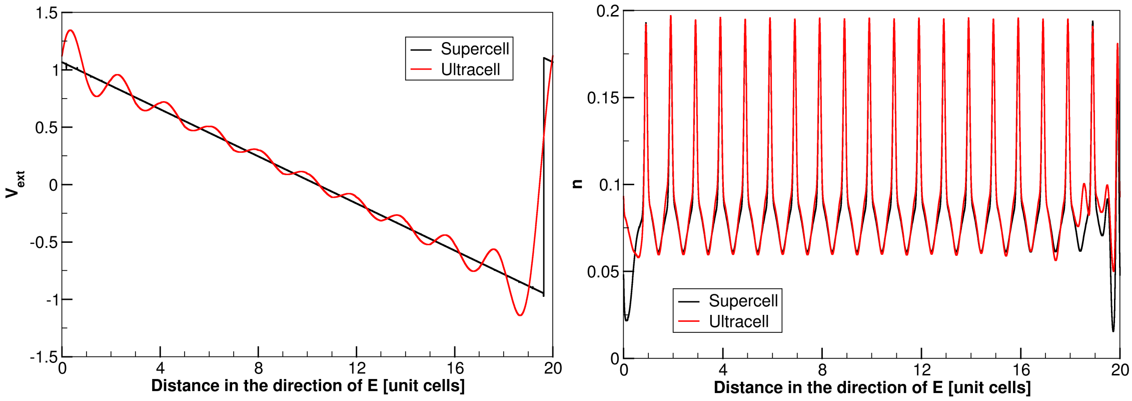

(a) **(b)**

Figure 4.3
a) The external potential applied to bulk Si along the (110) direction for the supercell and the ultracell. In the supercell, the potential is expanded microscopically in ***G***-vectors (750 ***G***-vectors). In the ultracell, the potential is expanded in coarsely sampled ***Q***-vectors (20 ***Q***-vectors), leading to visible remaining oscillations. b) A comparison of the self-consistent densities in bulk Si observed in the supercell and the ultracell along the direction of the electric field. The plotting axis is slightly offset relative to the atomic positions to avoid numerical spikes. We observe very good agreement in the center and worse agreement at the edges, which can be explained by the different sampling of the sawtooth.

4.4.2 “Planck” potential in Lithium

Ultimately, our aim is to have an efficient method for large systems. While we have seen in the previous section that our method can reproduce the results from a SC, we will focus on the performance of our method in this section. To that end, we consider bulk Li subjected to a large, extended electrostatic potential. The electrostatic potential we choose is what we refer to as the “Planck”-potential (fig. 4.4a). We constructed this potential by pixelating a black-white photo of Max Planck. We chose the size of our potential such that each pixel corresponds to a unit cell of bulk Li. To ensure a periodic potential, we multiplied the outcome with a smoothed version of the 2d rectangle function. The resulting potential is applied to 81x81x1 unit cells of bulk Li with a two atomic basis, corresponding to 13122 atoms in total. For our calculation we used 6x6x6 normal $\boldsymbol{k}$-points, 4 empty states and 27x27x1 $\boldsymbol{Q}$-points, corresponding to 14x14x1 $\boldsymbol{\kappa}$-points. The total computation time, including the ground state calculation and the plotting, was slightly under 50 hours on 220 cores. In fig. 4.4b we plot the self-consistent change in the density $\sum_{Q\neq 0} n_{\boldsymbol{Q}}\left(\boldsymbol{r}\right) e^{i\boldsymbol{Q}\cdot\boldsymbol{r}}$ due to the additional external field. The imprint of the potential is clearly visible. Upon a careful inspection, the nuclear positions can also be recognized as a fine grid. As the electronic density is mainly found close to the nuclei, those are the regions where the largest changes occur. This is even more visible in fig. 4.4c, where a magnification of a specific region of the self-consistent charge density is shown. When looking at the total self-consistent potential (fig. 4.4d), we observe that the magnitude is smaller compared to the external electric field, indicating that the electrons screen the external potential. Convergence was obtained after 399 self-consistent iterations and a steady convergence was observed.

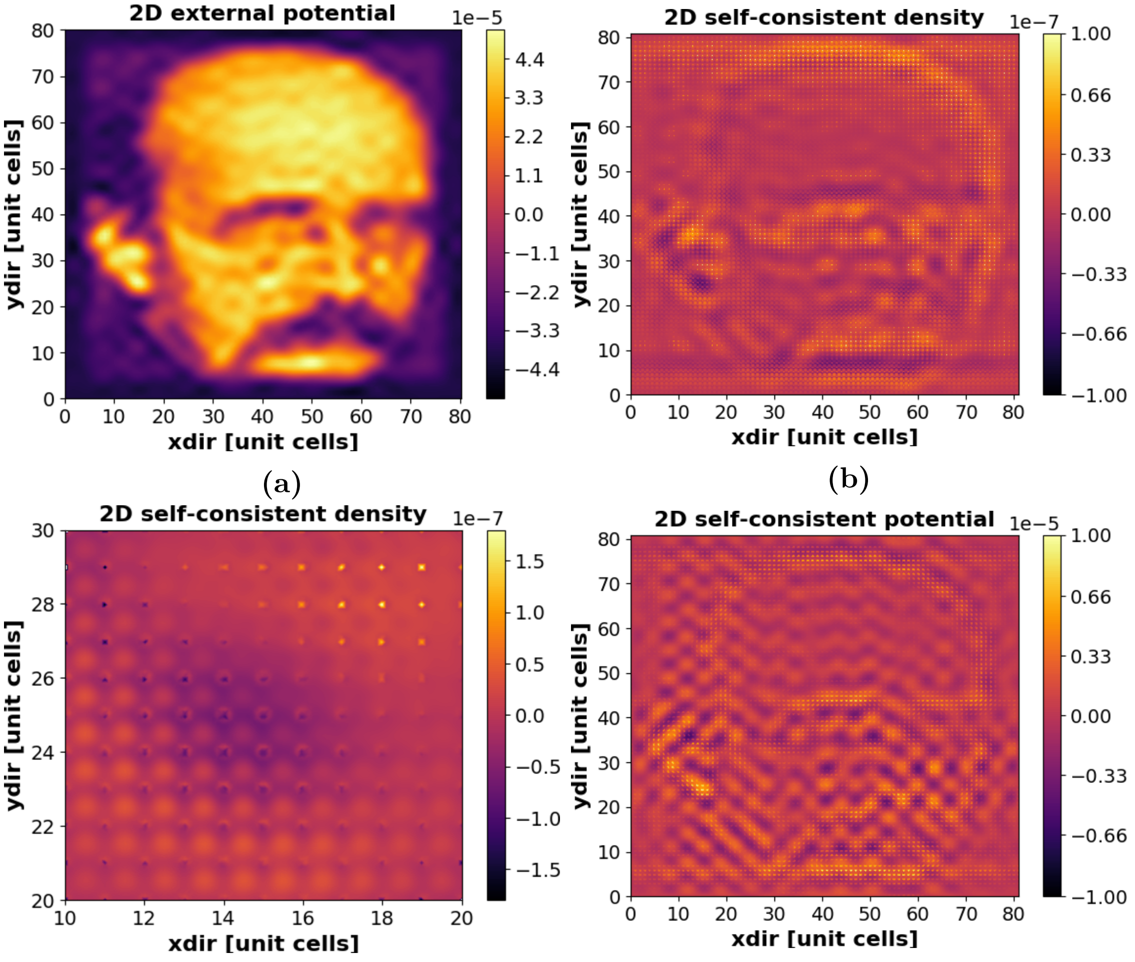

(a) (b)

(c) (d)

Figure 4.4
a) External “Planck”-potential. b) The change in the ground state of bulk Lithium due to the electric potential shown in fig. 4.4d. The electronic density roughly takes the shape of the external potential. The atomic positions show as a grid of small dots. c) Magnification of a small region of the density, the atomic positions are clearly visible. d) Total self-consistent electrostatic potential. The electrons arrange themselves such that the external potential is screened, resulting in a lower magnitude.

4.4.3 Spin-spirals in γ-Iron

Spin-spirals can arguably be considered to be the most basic test for our ULR method. As noted above, the spin-spiral state is a special case of the ULR ansatz. For a direct comparison, we performed a calculation on fcc-Fe (the "γ phase" of Fe) which is known to have a spiral configuration of the magnetization [80]. For the UC we used $1 \times 12 \times 12$ **k**-points, $32 \times 1 \times 1$ **Q**-points and $32 \times 1 \times 1$ unit cells. A single unit cell was used for the spin-spiral calculation with a $12 \times 12 \times 12$ **k**-point grid and a **Q**-vector of 1/32. An initial magnetic field is required to break spin symmetry. To ensure an unbiased calculation, we applied a random field to the UC calculation and subsequently reduced it to zero. Throughout the calculation, we enforce the constraint $\int_{\text{unit}} \mathrm{d}\boldsymbol{r}\, \boldsymbol{m}_{\boldsymbol{Q}=0}(\boldsymbol{r}) = 0$ to ensure that the system is not drawn to a lattice-periodic ferromagnetic solution. The magnetization converged to an ordered spin-spiral state where the magnitude was constant over the UC and only the direction varied (Fig. 4.5(a)). This corresponds precisely to the spin-spiral state. The overall magnitude of the magnetization is sensitive to the lattice parameter and undergoes a transition from $\sim 1\mu_B$ to $\sim 2.5\mu_B$ for this relatively small **Q**-vector. As may be seen in Fig. 4.5(b), this behavior is observed for both the UC and spin-spiral calculations.

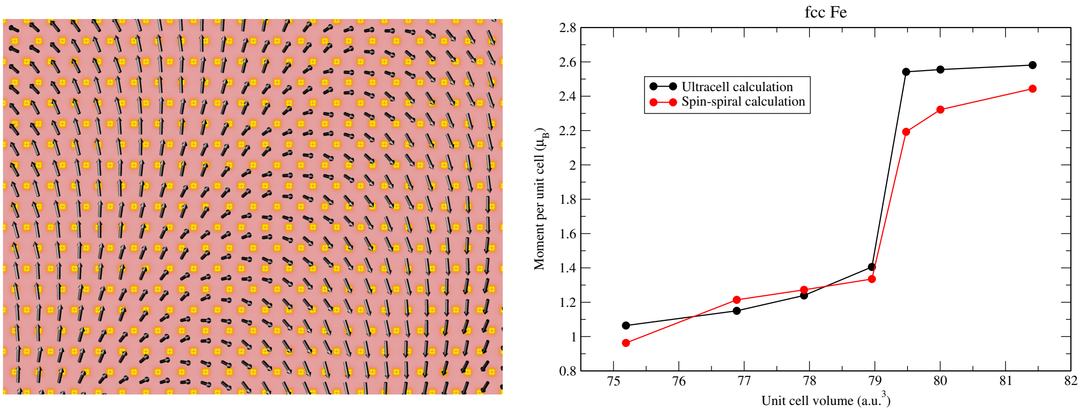

(a)

(b)

Figure 4.5
(a) Ultra long-range magnetization density of γ-Fe plotted in the plane perpendicular to [001]. The color indicates the magnitude of the magnetization and the arrows indicate direction. The modulation encompasses 32 unit cells in the [100] direction. (b) Plot of moment against unit cell volume for both the long-range and spin-spiral ansatz.

4.4.4 Spin-density wave in Chromium

Finally we aim at calculating the SDW state in Cr. The existence of a SDW in Cr is well known and first research dates back to around 1960 [81–83]. Despite this, computing the SDW state within DFT remains difficult and has been the topic of many studies [84–96], with partially conflicting results [97]. It is likely that a SDW is not the true ground state of Cr within DFT [98]. We will not focus on the inherent difficulties of the system in the following. Instead we will benchmark our ultra-long range approach against a direct calculation with a SC. Cr is an excellent test case, as the periodicity of the SDW is ≈ 20.83 unit cells, which is still well within computational reach of a conventional SC approach. This state is not achievable by the spin-spiral ansatz because the magnitude of the moment changes but not its direction, thus a SC calculation is required.

For our comparison, we use the LSDA and a lattice parameter of 2.905 Å as suggested by Cottenier et al. [97]. We consider $21 \times 1 \times 1$ unit cells of bulk Cr for both SC and UC calculations. For the SC we used a $1 \times 12 \times 12$ $\mathbf{k}$-point grid. A randomized symmetry breaking magnetic field was used to start the calculation and subsequently reduced to zero. Spin-orbit coupling was also applied. Our SC calculation reproduces the result by Cottenier et al. [97]. For the UC we also used a $1 \times 12 \times 12$ $\mathbf{k}$-point grid with a $21 \times 1 \times 1$ $\mathbf{Q}$-point grid corresponding to a grid of $11 \times 1 \times 1$ $\boldsymbol{\kappa}$-points to obtain the best possible sampling of the xc-potential and -field. Around 60 empty states in the lattice-periodic basis are used to provide enough degrees of freedom during the convergence. We start with a randomized initial field which we reduce during each step. Throughout the calculation, we enforce the constraint $\int_{\mathrm{MT}} \mathrm{d}\boldsymbol{r}\, \boldsymbol{m}_{\boldsymbol{Q}=0}(\boldsymbol{r}) = 0$ for each muffin-tin. This ensures that the system is not drawn to a lattice-periodic anti-ferromagnetic solution.

Our results are shown in Fig. 4.6. Specifically, Fig. 4.6(a) shows the comparison of the magnetization in the SDW state, as obtained from the SC and UC calculations. The maximum moment of the UC result is larger than that of the SC, 1.174 μ_B and 0.712 μ_B, respectively. We attribute this to the fact that the ULR calculation is performed in the basis of Kohn-Sham states and not in the original LAPW basis for which the linearization energies are optimally adjusted. It is also known that LSDA calculations of this system are particularly sensitive to the basis and the moment depends strongly on the lattice parameter [97].

In Fig. 4.6(b) we present the charge density wave (CDW) which is known to stabilize alongside the SDW with twice the period. While obtaining the CDW in the UC is straight-forward (as all $\rho_{\mathbf{Q}}(\mathbf{r})$ are known), it is numerically more challenging to extract it for the SC. We did this by subtracting the density from the calculation of a single unit cell. We obtain the same periodicity in both calculations as well as a comparable magnitude.

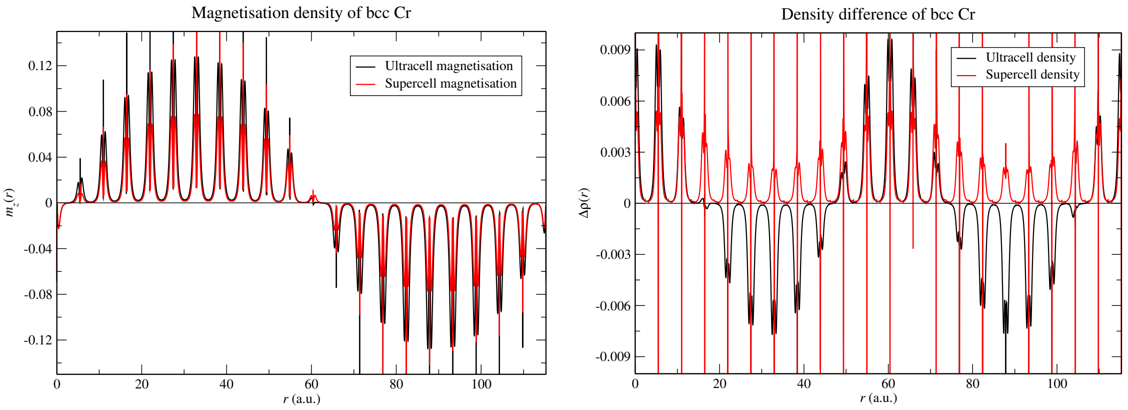

(a) **(b)**

Figure 4.6
(a) Magnetisation density for bcc Cr over 21 unit cells. (b) Change in density over the same range. For the ultracell, this was generated by setting $\rho_{\mathbf{Q}=0}(\mathbf{r})$ in eq. (4.12) to zero. For the supercell, the lattice-periodic density was subtracted leaving just the modulated density.

4.5 Time-dependent ultra long-range systems

We will conclude this chapter with some brief considerations about a possible future generalization of our ULR approach to time-dependent systems. Such a generalization can be easily achieved by considering explicitly time-dependent ULR orbitals

$$\Phi_\alpha^{\boldsymbol{k}}(\boldsymbol{r},t) = \frac{1}{\sqrt{N_u}} \sum_{j\boldsymbol{\kappa}} c^\alpha_{j\boldsymbol{k}+\boldsymbol{\kappa}}(t) \begin{pmatrix} u^\uparrow_{j\boldsymbol{k}}(\boldsymbol{r}) \\ u^\downarrow_{j\boldsymbol{k}}(\boldsymbol{r}) \end{pmatrix} e^{i(\boldsymbol{k}+\boldsymbol{\kappa})\cdot\boldsymbol{r}} \tag{4.31}$$

which result in time-dependent ULR densities:

$$n(\boldsymbol{r},t) = \sum_{\boldsymbol{Q}} n_{\boldsymbol{Q}}(\boldsymbol{r},t)\, e^{i\boldsymbol{Q}\cdot\boldsymbol{r}}, \quad \boldsymbol{m}(\boldsymbol{r},t) = \sum_{\boldsymbol{Q}} \boldsymbol{m}_{\boldsymbol{Q}}(\boldsymbol{r},t)\, e^{i\boldsymbol{Q}\cdot\boldsymbol{r}}. \tag{4.32}$$

It is then straight-forward to derive a time-dependent KS system analogous to the system we derived in section 4.2.2, which can be time-propagated with the algorithm presented in section 3.3.4.

An ULR time-dependent system seems specifically promising in the context of light-matter interactions. We will show in the following that it is very easy to couple such a system to Maxwell's equations. In section 3.3.3 we found that the vector potential in Coulomb gauge is given by

$$\Delta \boldsymbol{A}(\boldsymbol{r},t) - \frac{1}{c^2}\partial_t^2 \boldsymbol{A}(\boldsymbol{r},t) = -\frac{4\pi}{c}\boldsymbol{j}_T(\boldsymbol{r},t) \tag{4.33}$$

with the transverse current

$$\boldsymbol{j}_T(\boldsymbol{r},t) = \boldsymbol{j}(\boldsymbol{r},t) + \frac{1}{4\pi}\nabla\left(\nabla\cdot\int d^3r'\,\frac{\boldsymbol{j}(\boldsymbol{r'},t)}{|\boldsymbol{r}-\boldsymbol{r'}|}\right) \tag{4.34}$$

and the total effective current

$$\boldsymbol{j}\left(\boldsymbol{r},t\right)=\boldsymbol{j}_{f}\left(\boldsymbol{r},t\right)+c\mu_{\mathrm{B}}\nabla\times\boldsymbol{m}\left(\boldsymbol{r},t\right)+\frac{\partial\boldsymbol{P}\left(\boldsymbol{r},t\right)}{\partial t}. \tag{4.35}$$

We can very easily solve for the vector potential if we have the current in the ULR form

$$\boldsymbol{j}\left(\boldsymbol{r},t\right)=\sum_{\boldsymbol{Q}}\boldsymbol{j}_{\boldsymbol{Q}}\left(\boldsymbol{r},t\right)e^{i\boldsymbol{Q}\cdot\boldsymbol{r}}=\sum_{\boldsymbol{G},\boldsymbol{Q}}\boldsymbol{j}_{\boldsymbol{Q}}\left(t\right)e^{i(\boldsymbol{G}+\boldsymbol{Q})\cdot\boldsymbol{r}}, \tag{4.36}$$

where we transformed the lattice-periodic $\boldsymbol{r}$-dependence to a plain-wave basis. The coefficients for the transverse current $\boldsymbol{j}_{\boldsymbol{G},\boldsymbol{Q}}$ can then be derived analytically:

$$\boldsymbol{j}^{T}_{\boldsymbol{G},\boldsymbol{Q}}=\boldsymbol{j}_{\boldsymbol{G},\boldsymbol{Q}}-\frac{\left(\left(\boldsymbol{G}+\boldsymbol{Q}\right)\cdot\boldsymbol{j}_{\boldsymbol{G},\boldsymbol{Q}}\right)\left(\boldsymbol{G}+\boldsymbol{Q}\right)}{\left(\boldsymbol{G}+\boldsymbol{Q}\right)^{2}}. \tag{4.37}$$

With this we obtain for the vector potential (eq. 4.33)

$$\partial_{t}^{2}\boldsymbol{A}_{\boldsymbol{G},\boldsymbol{Q}}\left(t\right)=4\pi\boldsymbol{j}^{T}_{\boldsymbol{G},\boldsymbol{Q}}\left(t\right)-c^{2}\left(\left(\boldsymbol{G}+\boldsymbol{Q}\right)\cdot\boldsymbol{A}_{\boldsymbol{G},\boldsymbol{Q}}\left(t\right)\right)\left(\boldsymbol{G}+\boldsymbol{Q}\right), \tag{4.38}$$

which is an ordinary differential equation for the Fourier coefficients of the vector potential. A time propagation of the vector potential is thus very easy. While it remains difficult to accurately calculate $\boldsymbol{j}_{f}$ and $\boldsymbol{P}$, this approach makes coupling of a TD-KS to Maxwell's equations computationally much more feasible. Possible applications include real-time simulations of transmission and reflection or even real-time simulations of the Faraday effect and the MOKE. As the dipole approximation is often well fulfilled, it should suffice to only include the long-range contribution in most cases, i.e. setting $\boldsymbol{G}=0$, which will drastically reduce the number Fourier coefficients to describe the vector potential.

Finally, we note that if one is only interested in the time-dependent MDI, it is possible to just evaluate a set of instantaneous Poisson equations, analogously to the Hartree potential:

$$\boldsymbol{A}^{\mathrm{dip}}\left(\boldsymbol{r},t\right)=\mu_{\mathrm{B}}\int\mathrm{d}\boldsymbol{r'}\frac{\nabla\times\boldsymbol{m}\left(\boldsymbol{r'},t\right)}{\left|\boldsymbol{r}-\boldsymbol{r'}\right|}. \tag{4.39}$$

This is possible because the second term in eq. 4.34 vanishes for the MDI:

$$\int\mathrm{d}\boldsymbol{r'}\nabla_{\boldsymbol{r}}\cdot\frac{\nabla_{\boldsymbol{r'}}\times\boldsymbol{m}\left(\boldsymbol{r'},t\right)}{\left|\boldsymbol{r}-\boldsymbol{r'}\right|}=\int\mathrm{d}\boldsymbol{r'}\frac{1}{\left|\boldsymbol{r}-\boldsymbol{r'}\right|}\nabla_{\boldsymbol{r'}}\cdot\left(\nabla_{\boldsymbol{r'}}\times\boldsymbol{m}\left(\boldsymbol{r'},t\right)\right)=0. \tag{4.40}$$

Here we employed integration by parts. A surface term does not appear as $\boldsymbol{m}$ is typically a smooth and well-behaved function. This makes physical sense: The second term in eq. 4.34 creates a current density at every point in space such that causality is kept (as the scalar potential is an instantaneous function of the density). The MDI interaction is purely magnetic and therefore not affected by a change in gauge of the scalar potential.

4.6 Limits of the ultra long-range method

Our ULR approach is of course an approximation to the exact result obtained by a SC. We will therefore discuss in the following, when we expect our approximation to break down. As mentioned in subsection 4.3.2, we expect our ansatz to perform poorly in situations where the UC has approximately the same size as the Born-von Karman cell. This is because the $\boldsymbol{k} + \boldsymbol{\kappa}$ points will overlap and not maintain strict orthogonality. Our results show, however, that the UC correctly reproduces the magnetization for both the spin-spiral in γ-Fe (subsection 4.4.3) and the SDW in Cr (subsection 4.4.4), which indicates that this problem might not be particularly severe. The larger difference observed in Cr might be due to the system being smaller and thus being more heavily effected by this. Due to only having two systems for comparison and Cr being very difficult for DFT, one has to be careful with drawing conclusions, though. Generally, a large separation of $\boldsymbol{k}$ and $\boldsymbol{\kappa}$ length-scales is still desirable.

We further expect the method to become inefficient in cases where both the UC is large and a high resolution of density modulations is required. This could be a limiting factor when, for example, trying to model defects or when perturbatively expanding the effect of atomic displacements in the external potential. The necessary number of $\boldsymbol{Q}$-vectors in these cases might be prohibitively large. Magnetic domain walls might also be challenging, as a domain wall is very small compared to the neighboring domains, hinting at a large number of required $\boldsymbol{Q}$-vectors. More generally speaking, if a very large number of Fourier components is necessary to accurately describe the ULR modulation, the method will become inefficient. We note, however, that there are currently no general alternatives to our approach for such systems.

Finally, we have not yet tested our method for time-dependent systems. While there are no mathematical restrictions, it remains to be seen how fast and accurate simulations will be in practice. It is also not obvious, how many $\boldsymbol{Q}$-vectors compared to a ground state calculation are necessary to faithfully capture the time evolution of a time-dependent system.

5. Exchange functional for the magnetic dipole interaction

In the previous chapter, we derived ULR KS equations and explicitly included the MDI. The general KS system we considered is given by eq. 4.6:

$$\hat{H}_0 = -\frac{\nabla^2}{2} + v_s\left(\boldsymbol{r}\right) + \mu_B \boldsymbol{B}_s\left(\boldsymbol{r}\right) \cdot \boldsymbol{\sigma} + 2i\mu_B\left(\boldsymbol{A}_{\text{ext}}\left(\boldsymbol{r}\right) \cdot \nabla\right) + 2\mu_B^2 \boldsymbol{A}_{\text{ext}}^2\left(\boldsymbol{r}\right).$$

with $v_s\left(\boldsymbol{r}\right) = v_{\text{ext}}\left(\boldsymbol{r}\right) + v_{\text{H}}\left(\boldsymbol{r}\right) + v_{\text{xc}}\left(\boldsymbol{r}\right)$ and $\boldsymbol{B}_s\left(\boldsymbol{r}\right) = \boldsymbol{B}_{\text{ext}}\left(\boldsymbol{r}\right) + \boldsymbol{B}_{\text{xc}}\left(\boldsymbol{r}\right) + \boldsymbol{B}_{\text{DP}}\left(\boldsymbol{r}\right)$. From the basic considerations in chapter 2, it should be clear that adding an extra interaction (in our case the MDI) to the KS system leads to an additional contribution to the XC energy. This additional contribution then guarantees that the non-interacting KS system reproduces the charge and magnetization densities of a system interacting via both, the Coulomb interaction and the MDI.

In this chapter, we will derive an approximate functional for the contribution to the exchange energy arising from the MDI, which we will then be able use alongside the Coulomb XC functional. In the KS system, this will result in an extra term $\boldsymbol{B}_{\text{x}}^{\text{DP}}\left(\boldsymbol{r}\right)$ in the exchange field:

$$\boldsymbol{B}_{\text{xc}}\left(\boldsymbol{r}\right) = \boldsymbol{B}_{\text{xc}}^{\text{C}}\left(\boldsymbol{r}\right) + \boldsymbol{B}_{\text{x}}^{\text{DP}}\left(\boldsymbol{r}\right). \tag{5.1}$$

Our functional is specifically designed for long length-scales and is easy to use with the ultra long-range ansatz introduced in chapter 4. This should increase the accuracy when calculating large-scale magnetic structures. We will proceed as follows: We will first consider the non-local part of the MDI (eq. 4.1) and show that a LDA based on the homogeneous electron gas is always zero. We then consider a weakly inhomogeneous electron gas and obtain a finite exchange functional from perturbation theory. We discuss higher order energy contributions and derive the lowest order energy contribution of the non-local contribution to the homogeneous electron gas. Finally we show that a finite, local exchange energy contribution of the MDI arises from the spin-contact contribution (eq. 4.1). The results of this section have been partially published previously [99].

5.1 Exchange energy of the homogeneous electron gas

We want to derive an exchange energy for the MDI (eq. 2.72). We will for now focus solely on the first term, which for two particles is given by:

$$H^{\mathrm{dip}} = -\mu_{\mathrm{B}}^2 \left(\frac{3\left[(\boldsymbol{r}-\boldsymbol{r'})\cdot\boldsymbol{\sigma}\right]\left[(\boldsymbol{r}-\boldsymbol{r'})\cdot\boldsymbol{\sigma'}\right]}{\left|\boldsymbol{r}-\boldsymbol{r'}\right|^5} - \frac{\boldsymbol{\sigma}\cdot\boldsymbol{\sigma'}}{\left|\boldsymbol{r}-\boldsymbol{r'}\right|^3} \right). \tag{5.2}$$

An exchange functional for the spin-contact interaction (eq. 4.1) is derived in section 5.4. With eq. 5.2, we have for the exchange energy:

$$E_{\mathrm{x}}^{\mathrm{dip}} = -\frac{1}{2}\sum_{\boldsymbol{a},\boldsymbol{b}}\sum_{s_a,s_b} \left\langle \varphi_{\boldsymbol{a},s_a}\varphi_{\boldsymbol{b},s_b} \left| H^{\mathrm{dip}} \right| \varphi_{\boldsymbol{b},s_b}\varphi_{\boldsymbol{a},s_a} \right\rangle. \tag{5.3}$$

We use plane waves with a fixed spin as orbitals for the homogeneous electron gas:

$$\varphi_{\boldsymbol{k},\uparrow}(\boldsymbol{r}) = \frac{1}{\sqrt{V}} e^{i\boldsymbol{k}\cdot\boldsymbol{r}} \begin{pmatrix}1\\0\end{pmatrix}, \quad \varphi_{\boldsymbol{k},\downarrow}(\boldsymbol{r}) = \frac{1}{\sqrt{V}} e^{i\boldsymbol{k}\cdot\boldsymbol{r}} \begin{pmatrix}0\\1\end{pmatrix}. \tag{5.4}$$

We start by evaluating the expectation value $\left\langle \varphi_{\boldsymbol{a},s_a}\varphi_{\boldsymbol{b},s_b} \left| H^{\mathrm{dip}} \right| \varphi_{\boldsymbol{b},s_b}\varphi_{\boldsymbol{a},s_a} \right\rangle$. We will first consider the case where every spin is pointing upwards, $s_i = \uparrow$:

$$\begin{aligned}
\langle\uparrow\uparrow \left| H^{\mathrm{dip}} \right| \uparrow\uparrow\rangle &= -\mu_{\mathrm{B}}^2 \left\langle \varphi_{\boldsymbol{a}}\varphi_{\boldsymbol{b}} \left| \frac{3\left(r_z - r_z'\right)^2}{\left|\boldsymbol{r}-\boldsymbol{r'}\right|^5} - \frac{1}{\left|\boldsymbol{r}-\boldsymbol{r'}\right|^3} \right| \varphi_{\boldsymbol{b}}\varphi_{\boldsymbol{a}} \right\rangle \\
&= -\frac{\mu_{\mathrm{B}}^2}{V^2} \int \mathrm{d}\boldsymbol{r} \int \mathrm{d}\boldsymbol{r}' \left[\frac{3r_z^2}{r^5} - \frac{1}{r^3} \right] e^{i\boldsymbol{r}\cdot(\boldsymbol{a}-\boldsymbol{b})} \\
&= -\frac{\mu_{\mathrm{B}}^2}{V} \int \mathrm{d}\boldsymbol{r} \left[\frac{3r_z^2}{r^5} - \frac{1}{r^3} \right] e^{i\boldsymbol{r}\cdot(\boldsymbol{a}-\boldsymbol{b})} \\
&= -\frac{\mu_{\mathrm{B}}^2}{V}\frac{4\pi}{3} \left(1 - 3\frac{\left(a_z - b_z\right)^2}{\left(\boldsymbol{a}-\boldsymbol{b}\right)^2} \right) \\
&\equiv -\frac{\mu_{\mathrm{B}}^2}{V}\, \eta_z\left(\boldsymbol{a}-\boldsymbol{b}\right).
\end{aligned} \tag{5.5}$$

In the second line, we made the shift $\boldsymbol{r} \to \boldsymbol{r}+\boldsymbol{r'}$. The integral over $\boldsymbol{r'}$ then just yields a volume factor V. The remaining integral corresponds to the Fourier transform of the dipole interaction [100].

The following spin-combinations all yield the same result (no spin-flip occurs):

$$\langle\uparrow\uparrow \left| H^{\mathrm{dip}} \right| \uparrow\uparrow\rangle = \langle\downarrow\downarrow \left| H^{\mathrm{dip}} \right| \downarrow\downarrow\rangle = -\langle\uparrow\downarrow \left| H^{\mathrm{dip}} \right| \uparrow\downarrow\rangle = -\langle\downarrow\uparrow \left| H^{\mathrm{dip}} \right| \downarrow\uparrow\rangle. \tag{5.6}$$

We also have to consider the energy contribution when spin-flips occur:

$$\begin{aligned}
\langle\uparrow\downarrow \left|H^{\mathrm{dip}}\right| \downarrow\uparrow\rangle &= \langle\downarrow\uparrow \left|H^{\mathrm{dip}}\right| \uparrow\downarrow\rangle \\
&= -\mu_{\mathrm{B}}^2 \left\langle \varphi_{\boldsymbol{a}}\varphi_{\boldsymbol{b}} \middle| \begin{pmatrix} 1 \\ -i \\ 0 \end{pmatrix} \left[\frac{3\left(\boldsymbol{r}-\boldsymbol{r'}\right)\left(\boldsymbol{r}-\boldsymbol{r'}\right)}{\left|\boldsymbol{r}-\boldsymbol{r'}\right|^5} - \frac{1}{\left|\boldsymbol{r}-\boldsymbol{r'}\right|^3} \right] \begin{pmatrix} 1 \\ i \\ 0 \end{pmatrix} \middle| \varphi_{\boldsymbol{b}}\varphi_{\boldsymbol{a}} \right\rangle \\
&= -\mu_{\mathrm{B}}^2 \left\langle \varphi_{\boldsymbol{a}}\varphi_{\boldsymbol{b}} \middle| \left[\frac{3\left(\left(r_x-r'_x\right)^2+\left(r_y-r'_y\right)^2\right)}{\left|\boldsymbol{r}-\boldsymbol{r'}\right|^5} - \frac{2}{\left|\boldsymbol{r}-\boldsymbol{r'}\right|^3} \right] \middle| \varphi_{\boldsymbol{a}}\varphi_{\boldsymbol{b}} \right\rangle \\
&= -\frac{\mu_{\mathrm{B}}^2}{V}\left(\eta_x\left(\boldsymbol{a}-\boldsymbol{b}\right)+\eta_y\left(\boldsymbol{a}-\boldsymbol{b}\right)\right). \qquad (5.7)
\end{aligned}$$

with

$$\eta_x\left(\boldsymbol{q}\right) = \frac{4\pi}{3}\left(1-3\frac{q_x^2}{q^2}\right), \quad \eta_y\left(\boldsymbol{q}\right) = \frac{4\pi}{3}\left(1-3\frac{q_y^2}{q^2}\right). \qquad (5.8)$$

The total exchange energy contribution can now be calculated by evaluating the sum in eq. 5.3 for all contributing spin combinations, $\langle\uparrow\uparrow \left|H^{\mathrm{dip}}\right| \uparrow\uparrow\rangle$, $\langle\downarrow\downarrow \left|H^{\mathrm{dip}}\right| \downarrow\downarrow\rangle$, $\langle\uparrow\downarrow \left|H^{\mathrm{dip}}\right| \downarrow\uparrow\rangle$, $\langle\downarrow\uparrow \left|H^{\mathrm{dip}}\right| \uparrow\downarrow\rangle$. All other combinations do not conserve spin and do therefore not contribute. The energy is thus given by:

$$E_{\mathrm{x}}^{\mathrm{dip}} = -\frac{1}{2}\sum_{\boldsymbol{a},\boldsymbol{b}}\frac{\mu_{\mathrm{B}}^2}{V}2\left(\eta_x\left(\boldsymbol{a}-\boldsymbol{b}\right)+\eta_y\left(\boldsymbol{a}-\boldsymbol{b}\right)+\eta_z\left(\boldsymbol{a}-\boldsymbol{b}\right)\right), \qquad (5.9)$$

In the continuum limit $\sum_i \to V/\left(2\pi\right)^3 \int \mathrm{d}\boldsymbol{i}$ we obtain:

$$E_{\mathrm{x}}^{\mathrm{dip}} = -\frac{V\mu_{\mathrm{B}}^2}{\left(2\pi\right)^6}\left[\int \mathrm{d}\boldsymbol{a}\int \mathrm{d}\boldsymbol{b}\, 2\left(\eta_z\left(\boldsymbol{a}-\boldsymbol{b}\right)+\eta_x\left(\boldsymbol{a}-\boldsymbol{b}\right)+\eta_y\left(\boldsymbol{a}-\boldsymbol{b}\right)\right)\right] = 0. \qquad (5.10)$$

The dipole exchange energy of the homogeneous electron gas is zero as $\eta_x+\eta_y+\eta_y = 0$. Even for an arbitrary polarization, we find that the exchange energy is zero, as a full angular integration over any η_i vanishes:

$$\begin{aligned}
\int \mathrm{d}\boldsymbol{a}\int \mathrm{d}\boldsymbol{b}\ \eta_i\left(\boldsymbol{a}-\boldsymbol{b}\right) &= \int_{all}\mathrm{d}\boldsymbol{a}\int \mathrm{d}\boldsymbol{b}\ \eta_i\left(\boldsymbol{a}\right)\theta\left(k_f^2-\left(\boldsymbol{a}+\boldsymbol{b}\right)^2\right) \\
&= \int_{all}\mathrm{d}\boldsymbol{a}\int \mathrm{d}\boldsymbol{b}\ \eta_i\left(\boldsymbol{a}\right)\theta\left(k_f^2-a^2-b^2-2ab\cos\theta_b\right) \\
&= \int_{all}\mathrm{d}\boldsymbol{a}\ \eta_i\left(\boldsymbol{a}\right)h\left(\left|\boldsymbol{a}\right|\right) = 0. \qquad (5.11)
\end{aligned}$$

In the first step, we rewrote the integral over $\boldsymbol{a}$ as an integral over all space and made the shift $\boldsymbol{a} \to \boldsymbol{a}+\boldsymbol{b}$. The integration over $\boldsymbol{b}$ then results in a function $h\left(\left|\boldsymbol{a}\right|\right)$, which only depends on the magnitude of $\boldsymbol{a}$. It is then easy to see that the angular integration vanishes: In spherical coordinates $\eta_z\left(\boldsymbol{q}\right) = \frac{4\pi}{3}\left(1-3\cos^2\theta_q\right)$, which is a spherical harmonic. Due to the orthogonality of spherical harmonics, a full angular integration over any spherical harmonic is zero. From rotational invariance it follows that full angular integrations over η_x, η_y vanish as well. Constructing a local exchange functional for H^{dip} (eq. 5.2), similar to the LDA for the Coulomb interaction, is therefore not possible.

5.2 Perturbative exchange functional

Both the direct and the exchange interaction for H^{dip} (eq. 5.2) are zero in homogeneous systems. It is known, however, that the direct energy has a non-zero contribution for inhomogeneous systems. We thus expect that the exchange energy also has a finite contribution if the system is not homogeneous. We will, in this section, derive an exchange functional for H^{dip} based on a weakly inhomogeneous electron gas.

5.2.1 Functional form

We consider a homogeneous electron gas subjected to a spin-dependent perturbation which is given by:

$$\delta v_{\boldsymbol{Q}}^{\alpha}(\boldsymbol{r}) \equiv e^{i\boldsymbol{Q}\cdot\boldsymbol{r}}\sigma_{\alpha}\delta v_{\boldsymbol{Q}}, \tag{5.12}$$

where $\alpha = \{1, \ldots, 4\}$, $\sigma = (I_2, \boldsymbol{\sigma})$. We will proceed to calculate the change in the magnetic dipole exchange energy of the homogeneous electron gas due such an external perturbation, i.e. we will calculate the derivatives $\delta E_{\mathrm{x}}^{\mathrm{dip}}/\delta v_{\boldsymbol{Q}}^{\alpha}$. This can be achieved via the so-called Goldstone Diagrams, which are a diagrammatic approach to the Rayleigh-Schrödinger perturbation theory (cf. appendix A.1 for more details).

The first derivative of the exchange energy $E_{\mathrm{x}}^{\mathrm{dip}}$ is zero due to conservation of momentum (fig. 5.1). We thus have to calculate the change in the exchange energy to second order in the external perturbations, i.e. we have to evaluate

$$g_{\boldsymbol{Q}}^{\alpha,\beta} = \frac{\delta^2 E_{\mathrm{x}}^{\mathrm{dip}}}{\delta v_{\boldsymbol{Q}}^{\alpha}\delta v_{-\boldsymbol{Q}}^{\beta}}. \tag{5.13}$$

Assuming we would know the form of $g_{\boldsymbol{Q}}^{\alpha,\beta}$, we could derive the exchange kernel for the MDI via the chain rule

$$f_{\boldsymbol{Q}}^{\alpha\beta} \equiv \frac{\delta^2 E_{\mathrm{x}}^{\mathrm{dip}}}{\delta \rho_{\boldsymbol{Q}}^{\alpha}\delta \rho_{-\boldsymbol{Q}}^{\beta}} = \sum_{kl} \frac{\delta^2 E_{\mathrm{x}}^{\mathrm{dip}}}{\delta v_k \delta v_l} \left(\chi^{-1}\right)_{kj} \left(\chi^{-1}\right)_{li} = \sum_{kl} g_{kl} \left(\chi^{-1}\right)_{kj} \left(\chi^{-1}\right)_{li}, \tag{5.14}$$

where $\chi_{ij} = \delta\rho_i/\delta v_j$ is the response function of the system and $i, j, k, l \equiv (\alpha, \boldsymbol{Q})$ are compound indices. If we have the Fourier components of the change in the density of an actual system $\Delta\rho_{\boldsymbol{Q}}^{\alpha}$, we can then approximate the exchange energy by

$$E_{\mathrm{x}}^{\mathrm{dip}}[\rho] \approx \frac{1}{2}\sum_{\boldsymbol{Q}}\sum_{\alpha\beta} f_{\boldsymbol{Q}}^{\alpha\beta}\Delta\rho_{\boldsymbol{Q}}^{\alpha}\Delta\rho_{-\boldsymbol{Q}}^{\alpha}. \tag{5.15}$$

Therefore, the central quantity that needs to be calculated is g_{kl}, which we will do in the remainder of this section.

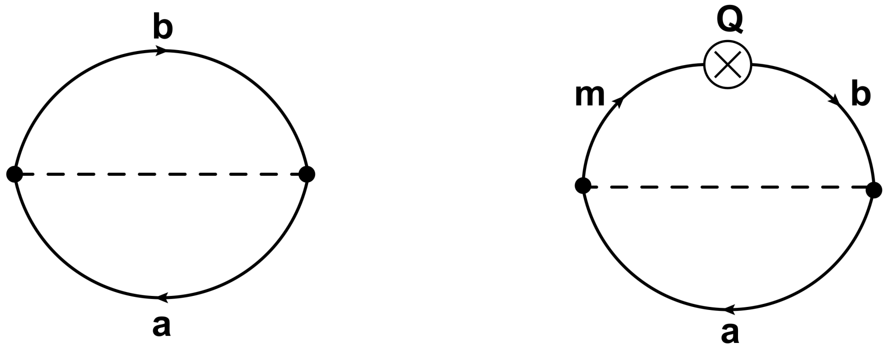

(a) (b)

Figure 5.1
a) Goldstone diagram for the exchange energy (eq. 5.3). The dashed line indicates the dipole-interaction. This diagram is zero for the homogeneous electron gas. b) An external perturbation, indicated by ⊗, is added to the exchange energy diagram. For a finite value of $\boldsymbol{Q}$, momentum is no longer conserved at each vertex. Thus there is no first order change in the exchange energy, i.e. $\delta E_{\mathrm{x}}^{\mathrm{dip}}/\delta v_{\boldsymbol{Q}}^{\alpha} = 0$.

5.2.2 Second order Goldstone Diagrams

We will use Goldstone diagrams which are second order in the external perturbation to evaluate the shift in the total exchange energy (i.e. g, eq. 5.13). All relevant Goldstone diagrams are shown in fig. 5.2. According to the Goldstone rules (cf. A.1), these diagrams are equal to:

$$a)\ S = \sum_{abnm} (-1)^3 \frac{\langle na|H|mb\rangle \langle b| - v_k|n\rangle \langle m| - v_l|a\rangle}{(\epsilon_b - \epsilon_n)(\epsilon_a - \epsilon_m)} \tag{5.16}$$

$$b)\ A = 2\sum_{abnm} (-1)^3 \frac{\langle nm|H|ab\rangle \langle b| - v_k|n\rangle \langle a| - v_l|m\rangle}{(\epsilon_b - \epsilon_n)(\epsilon_a + \epsilon_b - \epsilon_n - \epsilon_m)} \tag{5.17}$$

$$c)\ Y_1 = 2\sum_{abnm} (-1)^3 \frac{\langle ma|H|an\rangle \langle b| - v_k|m\rangle \langle n| - v_l|b\rangle}{(\epsilon_b - \epsilon_m)(\epsilon_b - \epsilon_n)} \tag{5.18}$$

$$d)\ Y_2 = 2\sum_{abcn} (-1)^4 \frac{\langle ba|H|ac\rangle \langle n| - v_k|b\rangle \langle c| - v_l|n\rangle}{(\epsilon_b - \epsilon_n)(\epsilon_c - \epsilon_n)} \tag{5.19}$$

$$e)\ F_1 = 2\sum_{abnm} (-1)^3 \frac{\langle ma|H|ab\rangle \langle b| - v_k|n\rangle \langle n| - v_l|m\rangle}{(\epsilon_b - \epsilon_m)(\epsilon_b - \epsilon_n)} \tag{5.20}$$

$$f)\ F_2 = 2\sum_{abcm} (-1)^4 \frac{\langle ma|H|ac\rangle \langle b| - v_k|n\rangle \langle c| - v_l|b\rangle}{(\epsilon_b - \epsilon_m)(\epsilon_c - \epsilon_m)} \tag{5.21}$$

All diagrams gain a prefactor of 2, as the interactions v_k and v_l are interchangeable (this compensates the factor 1/2 for symmetric diagrams). Some of the diagrams (e.g. the asymmetric diagram, fig. 5.2b) gain an additional prefactor of 2 as flipping these diagrams upside down produces an additional diagram with identical topology.

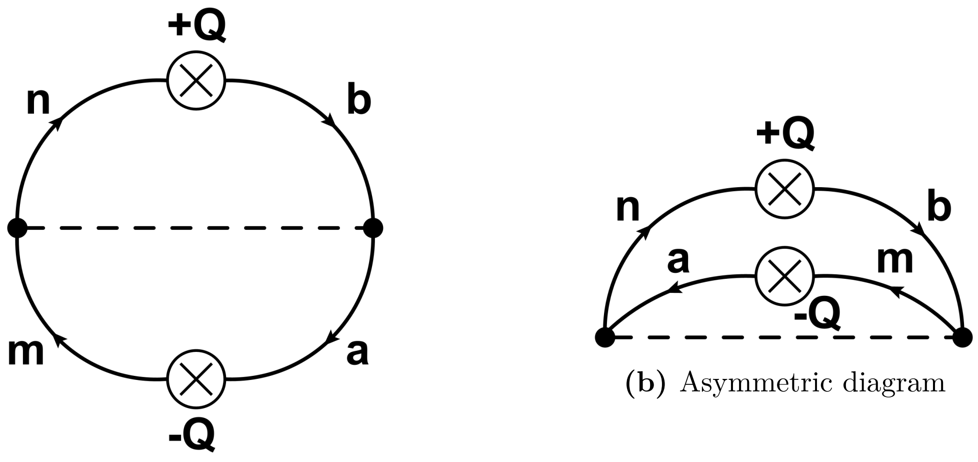

(a) Symmetric diagram

(b) Asymmetric diagram

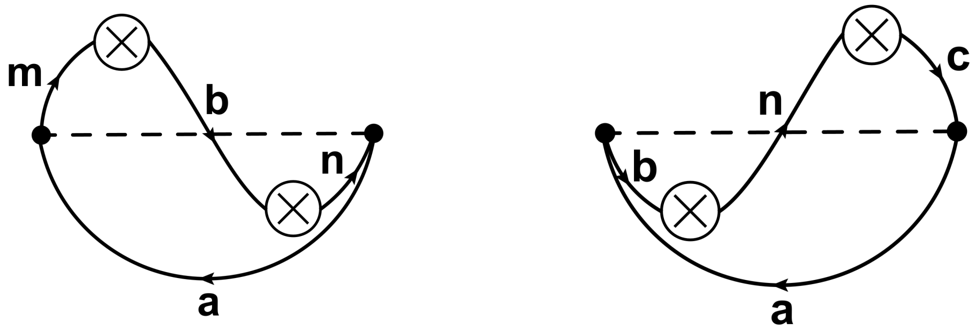

(c) Yin-Yang diagram

(d) Flipped Yin-Yang diagram

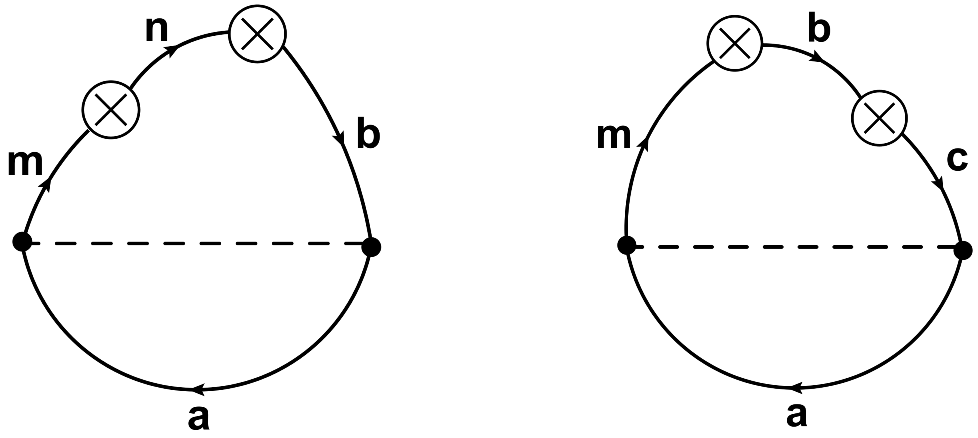

(e) Frog diagram

(f) Flipped frog diagram

Figure 5.2
All distinct second order Goldstone diagrams. Particles are labeled with n, m, l, holes are labeled with a, b, c. The external perturbation (eq. 5.12) is indicated by $\otimes$.

5.2.3 Spin Summation

As a first step, the summation over all possible spin combinations is considered. We will therefore only focus on the spin-dependent indices α, β of g (eq. 5.13) in this section. We distinguish between two different types of diagrams for the spin summation. The symmetric (S) (fig. 5.2a) and the asymmetric (A) (fig. 5.2b) diagram have one perturbation acting on each particle, whereas the Yin-Yang (Y) (fig. 5.2c,5.2d) and frog (F) (fig. 5.2e,5.2f) diagrams have two perturbations acting on the same particle. In both cases, we distinguish between conventional and unconventional processes. In conventional processes, the spin of the particles is unchanged by the external perturbation (eq. 5.12) whereas in unconventional processes the external perturbation may flip spins. In both, conventional and unconventional processes, the MDI may lead to an additional spin-flip of both particles simultaneously, which corresponds to the photon line carrying a spin of 1. We will account for all these processes and evaluate $g^{\alpha\beta}$ for every combination of v^{α} and v^{β} in the following. We start with carrying out the spin summations for the symmetric and the asymmetric diagram. All possible spin combinations are shown in table 5.1. Due to spin conservation, all matrix elements with only one spin-flip vanish (g^{01}, g^{02}, g^{13}, g^{23} and the corresponding transposed elements). The non-zero matrix elements are derived in table 5.2. In the case of a homogeneous, unpolarized electron gas, the system is invariant under inversion of all spins (e.g. $\uparrow\downarrow\uparrow\downarrow$ and $\downarrow\uparrow\downarrow\uparrow$ are identical). The remaining off-diagonal elements therefore also cancel. g_{AS} is then given by only three different matrix elements:

$$g_{\mathrm{AS}} = \begin{pmatrix} g_{\mathrm{AS}}^{00} & 0 & 0 & 0 \\ 0 & g_{\mathrm{AS}}^{11} & 0 & 0 \\ 0 & 0 & g_{\mathrm{AS}}^{11} & 0 \\ 0 & 0 & 0 & g_{\mathrm{AS}}^{33} \end{pmatrix}. \tag{5.22}$$

We will now carry out the spin-summations for the Yin-Yang and the frog diagrams. Diagram 5.2c (eq. 5.18) is used as an example, the other Yin-Yang diagram and the frog diagrams are analogous. In this diagram, there is no difference between conventional and unconventional processes. For the unconventional processes, conservation of spin at the vertices is only fulfilled if the second perturbation cancels the spin-flip of the first perturbation, therefore the result is the same as in the conventional case. Table 5.3 summarizes all possible spin combinations, all finite matrix elements are shown in table 5.4. As the spin of the hole b does not enter in the scalar product $\langle na|H|am\rangle$, its orientation does not change the absolute value of the matrix element. Consequently all spin combinations that only differ in the spin orientation of b have the same magnitude, e.g. $g^{00} = \uparrow\uparrow\uparrow\uparrow = g^{11} = \uparrow\downarrow\uparrow\uparrow$. Assuming a homogeneous, unpolarized system, the matrix for the Yin-Yang and frog diagrams

Table 5.1
All possible spin combinations for the symmetric and the asymmetric diagrams. Unconventional combinations are only possible if both perturbations flip the spin of the incoming particle. H^{dip} can lead to an overall spin-flip, in that case the photon line carries a spin of 1.

Spin combinations	a	b	n	m	Photon spin
conventional	↑	↑	↑	↑	0
	↓	↓	↓	↓	0
	↑	↓	↓	↑	1
	↓	↑	↑	↓	1
unconventional	↑	↓	↑	↓	0
	↓	↑	↓	↑	0

Table 5.2
All matrix elements of g which conserve spin at every vertex in the symmetric (S) and asymmetric (A) case. For homogeneous, unpolarized systems, the energy is invariant under an overall inversion of the spin, e.g. ↑↓↓↑ and ↓↑↑↓ are identical.

Matrix element	Spin terms (a b n m)
g_{SA}^{00}	↑↑↑↑ + ↓↓↓↓ + ↑↓↓↑ + ↓↑↑↓
g_{SA}^{30}	↑↑↑↑ − ↓↓↓↓ + ↑↓↓↑ − ↓↑↑↓
g_{SA}^{03}	↑↑↑↑ − ↓↓↓↓ − ↑↓↓↑ + ↓↑↑↓
g_{SA}^{33}	↑↑↑↑ + ↓↓↓↓ − ↑↓↓↑ − ↓↑↑↓
g_{SA}^{11}	↑↓↑↓ + ↓↑↓↑
g_{SA}^{21}	i ↑↓↑↓ $-i$ ↓↑↓↑
g_{SA}^{12}	$-i$ ↑↓↑↓ $+i$ ↓↑↓↑
g_{SA}^{22}	↑↓↑↓ + ↓↑↓↑

is given by a single matrix element:

$$g_{\mathrm{YF}} = g_{\mathrm{YF}}^{00} \begin{pmatrix} 1 & 0 & 0 & 0 \\ 0 & 1 & 0 & 0 \\ 0 & 0 & 1 & 0 \\ 0 & 0 & 0 & 1 \end{pmatrix} \tag{5.23}$$

Table 5.3
All possible spin combinations for the Yin-Yang and the frog diagrams. Conventional and unconventional processes are identical, due to conservation of spin. H^{dip} can lead to an overall spin-flip, in that case the photon line carries a spin of 1.

Spin combinations	a	b	n	m	Photon spin
conventional	↑	↑	↑	↑	0
	↓	↓	↓	↓	0
	↑	↓	↓	↓	1
	↓	↑	↑	↑	1
unconventional	↑	↓	↑	↑	0
	↓	↑	↓	↓	0
	↑	↑	↓	↓	1
	↓	↓	↑	↑	1

Table 5.4
All matrix elements of g which conserve spin at every vertex for the Yin-Yang (Y) and the frog (F) diagrams. For homogeneous, unpolarized systems, the energy is invariant under an overall inversion of the spin, e.g. ↑↓↑↓ and ↓↑↓↑ are identical.

Matrix element	Spin terms (a b n m)
g_{YF}^{00}	↑↑↑↑ + ↓↓↓↓ + ↑↓↓↓ + ↓↑↑↑
g_{YF}^{30}	↑↑↑↑ − ↓↓↓↓ + ↑↓↓↓ − ↓↑↑↑
g_{YF}^{03}	↑↑↑↑ − ↓↓↓↓ − ↑↓↓↓ + ↓↑↑↑
g_{YF}^{33}	↑↑↑↑ + ↓↓↓↓ + ↑↓↓↓ + ↓↑↑↑
g_{YF}^{11}	↑↓↑↑ + ↓↑↓↓ + ↑↑↓↓ + ↓↓↑↑
g_{YF}^{21}	i ↑↓↑↑ $-i$ ↓↑↓↓ $+i$ ↑↑↓↓ $-i$ ↓↓↑↑
g_{YF}^{12}	i ↑↓↑↑ $-i$ ↓↑↓↓ $-i$ ↑↑↓↓ $+i$ ↓↓↑↑
g_{YF}^{22}	↑↓↑↑ + ↓↑↓↓ + ↑↑↓↓ + ↓↓↑↑

5.2.4 Symmetric energy diagram

We will now explicitly evaluate the matrix elements $g_{\mathrm{S}}^{\alpha\beta}$ of the symmetric diagram (fig. 5.2a), which are given by eq. 5.16:

$$S = \sum_{abnm} (-1)^3 \frac{\langle na|H|mb\rangle \langle b| - v_k|n\rangle \langle m| - v_l|a\rangle}{(\epsilon_b - \epsilon_n)(\epsilon_a - \epsilon_m)}.$$

Without loss of generality, $v_k = v_{+\boldsymbol{Q}}$ and $v_l = v_{-\boldsymbol{Q}}$ is assumed. The second scalar product evaluates to

$$\langle b| - v_{+\boldsymbol{Q}}|n\rangle = -\int \mathrm{d}\boldsymbol{r}\, e^{i(\boldsymbol{b}-\boldsymbol{n}+\boldsymbol{Q})\cdot\boldsymbol{r}} = -\delta_{\boldsymbol{b}-\boldsymbol{n}+\boldsymbol{Q}}. \tag{5.24}$$

Similarly, we will find for the last one:

$$\langle m| - v_{-\boldsymbol{Q}}|a\rangle = -\int \mathrm{d}\boldsymbol{r}\, e^{i(\boldsymbol{m}-\boldsymbol{a}-\boldsymbol{Q})\cdot\boldsymbol{r}} = -\delta_{\boldsymbol{m}-\boldsymbol{a}-\boldsymbol{Q}}. \tag{5.25}$$

We can now carry out the sum over the particles n, m in eq. 5.16. This results in the constraints that $|\boldsymbol{a}+\boldsymbol{Q}| > k_f$, as $|\boldsymbol{m}| > k_f$ and $|\boldsymbol{b}+\boldsymbol{Q}| > k_f$, as $|\boldsymbol{n}| > k_f$ (with k_f being the Fermi wave vector):

$$S = \sum_{ab} \frac{\left\langle b+Qa|H^{\mathrm{dip}}|a+Qb\right\rangle}{(\epsilon_b - \epsilon_{b+Q})(\epsilon_a - \epsilon_{a+Q})} \Theta_{\boldsymbol{a}+\boldsymbol{Q}}\Theta_{\boldsymbol{b}+\boldsymbol{Q}}. \tag{5.26}$$

Here Θ is the Heaviside step function which restricts the summation to the correct values and we write $\Theta_{\boldsymbol{a}} = \Theta\left(\boldsymbol{a}^2 - k_f^2\right)$. In the continuum limit $\sum_i \to V/(2\pi)^3 \int \mathrm{d}\boldsymbol{i}$ we find:

$$S = \frac{4V^2}{(2\pi)^6} \int \mathrm{d}\boldsymbol{a} \int \mathrm{d}\boldsymbol{b} \frac{\left\langle b+Q\ a|H^{\mathrm{dip}}|a+Q\ b\right\rangle \Theta_{\boldsymbol{a}+\boldsymbol{Q}}\Theta_{\boldsymbol{b}+\boldsymbol{Q}}}{\left(b^2 - (\boldsymbol{b}+\boldsymbol{Q})^2\right)\left(a^2 - (\boldsymbol{a}+\boldsymbol{Q})^2\right)}. \tag{5.27}$$

a, b are holes to be integrated over a sphere from 0 to k_f. To calculate the total contribution of this diagram, it is necessary to solve the integral for the spin combinations shown in table 5.2. The remaining scalar product is given by eqs. 5.6, 5.7. The symmetric diagram for specific spin combinations is then:

$$S_{\uparrow\uparrow\uparrow\uparrow}, S_{\downarrow\downarrow\downarrow\downarrow}, -S_{\uparrow\downarrow\uparrow\downarrow}, -S_{\downarrow\uparrow\downarrow\uparrow} = \frac{4V\mu_{\mathrm{B}}^2}{(2\pi)^6} \int \mathrm{d}\boldsymbol{a} \int \mathrm{d}\boldsymbol{b} \frac{\eta_z(\boldsymbol{b}-\boldsymbol{a})\,\Theta_{\boldsymbol{a}+\boldsymbol{Q}}\Theta_{\boldsymbol{b}+\boldsymbol{Q}}}{\left(b^2 - (\boldsymbol{b}+\boldsymbol{Q})^2\right)\left(a^2 - (\boldsymbol{a}+\boldsymbol{Q})^2\right)}, \tag{5.28}$$

$$S_{\uparrow\downarrow\downarrow\uparrow}, S_{\downarrow\uparrow\uparrow\downarrow} = \frac{4V\mu_{\mathrm{B}}^2}{(2\pi)^6} \int \mathrm{d}\boldsymbol{a} \int \mathrm{d}\boldsymbol{b} \frac{(\eta_x(\boldsymbol{b}-\boldsymbol{a}) + \eta_y(\boldsymbol{b}-\boldsymbol{a}))\,\Theta_{\boldsymbol{a}+\boldsymbol{Q}}\Theta_{\boldsymbol{b}+\boldsymbol{Q}}}{\left(b^2 - (\boldsymbol{b}+\boldsymbol{Q})^2\right)\left(a^2 - (\boldsymbol{a}+\boldsymbol{Q})^2\right)}. \tag{5.29}$$

It is convenient to split these integrals into two parts:

$$S_{\uparrow\uparrow\uparrow\uparrow}, S_{\downarrow\downarrow\downarrow\downarrow}, -S_{\uparrow\downarrow\uparrow\downarrow}, -S_{\downarrow\uparrow\downarrow\uparrow} = \frac{\mu_{\mathrm{B}}^2}{12\pi^5} V\left(S_0 - 3S_z^q\right), \tag{5.30}$$

$$S_{\uparrow\downarrow\downarrow\uparrow}, S_{\downarrow\uparrow\uparrow\downarrow} = \frac{\mu_{\mathrm{B}}^2}{12\pi^5} V \left(2S_0 - 3S_x^q - 3S_y^q\right), \tag{5.31}$$

where

$$S_0 = \int \mathrm{d}\boldsymbol{a} \int \mathrm{d}\boldsymbol{b} \frac{\Theta_{\boldsymbol{a}+\boldsymbol{Q}} \Theta_{\boldsymbol{b}+\boldsymbol{Q}}}{\left(Q^2 + 2\boldsymbol{a}\cdot\boldsymbol{Q}\right)\left(Q^2 + 2\boldsymbol{b}\cdot\boldsymbol{Q}\right)}, \tag{5.32}$$

and

$$S_i^q = \int \mathrm{d}\boldsymbol{a} \int \mathrm{d}\boldsymbol{b} \frac{\left(q_i^2/q^2\right) \Theta_{\boldsymbol{a}+\boldsymbol{Q}} \Theta_{\boldsymbol{b}+\boldsymbol{Q}}}{\left(Q^2 + 2\boldsymbol{a}\cdot\boldsymbol{Q}\right)\left(Q^2 + 2\boldsymbol{b}\cdot\boldsymbol{Q}\right)}, \tag{5.33}$$

with $\boldsymbol{q} = \boldsymbol{a} - \boldsymbol{b}$. S_0 is evaluated first and the coordinate system is chosen such that $\boldsymbol{Q} \parallel \boldsymbol{e}_z$. We can then write in spherical coordinates

$$S_0 = \int \mathrm{d}\boldsymbol{a} \int \mathrm{d}\boldsymbol{b} \frac{\Theta\left(a^2 + Q^2 + 2aQx_a - k_f^2\right) \Theta\left(b^2 + Q^2 + 2bQx_b - k_f^2\right)}{\left(Q^2 + 2aQx_a\right)\left(Q^2 + 2bQx_b\right)}, \tag{5.34}$$

where the polar angle θ was substituted according to $x = \cos\theta$, hence $x \in [-1, 1]$. It is now easy to obtain the area of integration from the Heaviside function:

$$a^2 + Q^2 + 2k_aQx_a - k_f^2 > 0 \iff x_a > \frac{k_f^2 - a^2 - Q^2}{2aQ}. \tag{5.35}$$

But at the same time, $x \leq 1$ must be fulfilled, therefore:

$$\frac{k_f^2 - a^2 - Q^2}{2aQ} \leq 1 \iff a = -Q \pm k_f. \tag{5.36}$$

With a being strictly positive, only the positive solution $a = k_f - Q$ is relevant. Therefore the following integration boundaries are obtained

$$x = \cos\theta; x \in \left[\frac{k_f^2 - a^2 - Q^2}{2aQ}, 1\right]; a \in [k_f - Q, k_f]. \tag{5.37}$$

Thus the area of integration for holes is:

$$\int \mathrm{d}\boldsymbol{a}\ \Theta_{\boldsymbol{a}+\boldsymbol{Q}} = \int_{V_H} \mathrm{d}\boldsymbol{a} = \int_0^{2\pi} d\phi \int_{k_f - Q}^{k_f} \mathrm{d}a\ a^2 \int_{\left(k_f^2 - a^2 - Q^2\right)/(2aQ)}^{1} \mathrm{d}x. \tag{5.38}$$

We use this to rewrite eq. 5.34 as

$$S_0 = \int_{V_H} \mathrm{d}\boldsymbol{a} \int_{V_H} \mathrm{d}\boldsymbol{b} \frac{1}{\left(Q^2 + 2aQx_a\right)\left(Q^2 + 2bQx_b\right)}, \tag{5.39}$$

Computing S_0 is a rather easy task as the integrals for a and b are completely decoupled. We find:

$$S_0 = \left[\pi \frac{\left(4k_fQ + (-4k_f^2 + Q^2)\log\left[\left|\frac{2k_f - Q}{2k_f + Q}\right|\right]\right)}{8Q}\right]^2. \tag{5.40}$$

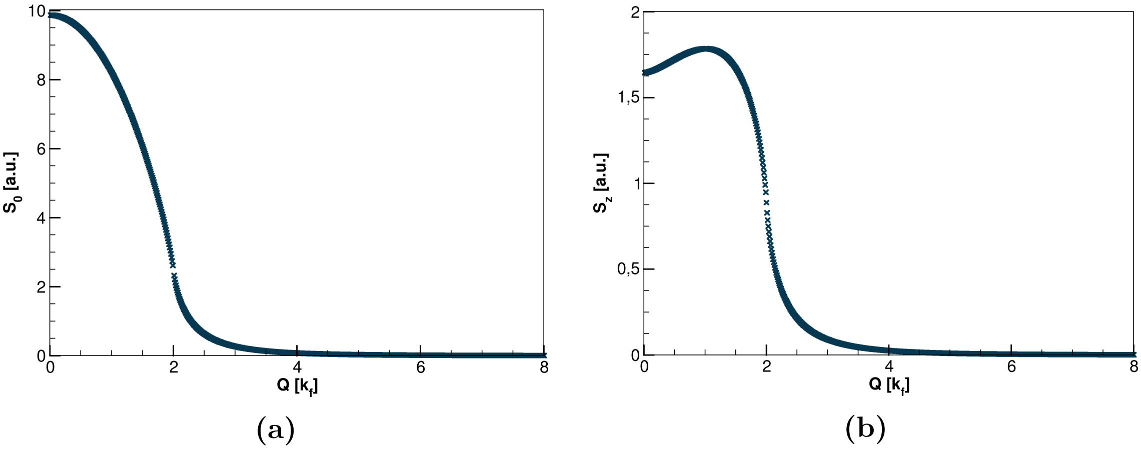

Figure 5.3
a) S_0 as a function of Q (eq. 5.40). The Fermi energy is set to 1. b) Numerical evaluation of the integral in eq. 5.45, as a function of Q. The Fermi energy is set to 1.

Fig. 5.3a shows S_0 as a function of Q for $k_f = 1$. When calculating S_i^q, it is important to realize that the denominator originating from the diagram does not depend on the angular coordinates ϕ, ϕ'. This holds for all other diagrams as well. It is therefore helpful to evaluate the angular integral first (in cylindrical coordinates):

$$\int_0^{2\pi} d\phi_a \int_0^{2\pi} d\phi_b \, \frac{q_z^2}{q^2} = \frac{4\pi^2 (z_a - z_b)^2}{\sqrt{\left(r_a^2 + r_b^2 + (z_a - z_b)^2\right)^2 - 4r_a^2 r_b^2}} \tag{5.41}$$

The integrals over q_x, q_y yield the same result due to the rotational invariance of the integrand:

$$\int_0^{2\pi} d\phi_a \int_0^{2\pi} d\phi_b \, \frac{q_{x/y}^2}{q^2} = 2\pi^2 \left(1 - \frac{(z_a - z_b)^2}{\sqrt{\left(r_a^2 + r_b^2 + (z_a - z_b)^2\right)^2 - 4r_a^2 r_b^2}} \right) \tag{5.42}$$

Comparing the results 5.41 and 5.42 shows that:

$$S_x^q = S_y^q = \frac{1}{2} S_0 - \frac{1}{2} S_z^q \implies S_x^q + S_y^q + S_z^q = S_0. \tag{5.43}$$

This is a very important result as it is valid for all other diagrams as well, as none of the other diagrams depends explicitly on ϕ or ϕ'. It is a direct consequence of the form of the η_i. The implication is that we only need to evaluate S_0 and S_z^q. The last step in evaluating the symmetric diagram is thus calculating S_z^q. This integral will be evaluated numerically. The correct area of integration for the remaining two coordinates is:

$$\int_{V_H,\mathrm{cyl}} d^2\mathrm{a} = \int_{-k_f}^{k_f} dz \int_0^{\sqrt{k_f^2 - z^2}} dr \, \Theta\left(r^2 + z^2 + 2Qz + Q^2 - k_f^2\right). \tag{5.44}$$

Combining eqs. 5.33, 5.41 and 5.44 yields:

$$S_z^q = \int_{V_H,\mathrm{cyl}} d^2\mathrm{a} \int_{V_H,\mathrm{cyl}} d^2\mathrm{b} \frac{1}{Q^2\left(Q+2z_a\right)\left(Q+2z_b\right)} \frac{4\pi^2(z_a-z_b)^2}{\sqrt{\left(r_a^2+r_b^2+\left(z_a-z_b\right)^2\right)^2-4r_a^2r_b^2}}. \tag{5.45}$$

The numerical results for this integral are shown in fig. 5.3b.

5.2.5 Asymmetric energy diagram

The asymmetric diagram (fig 5.2b) is given by eq. 5.17:

$$A = 2\sum_{abnm} (-1)^3 \frac{\left\langle nm|H^{\mathrm{dip}}|ab\right\rangle \langle b|-v_k|n\rangle \langle a|-v_l|m\rangle}{\left(\epsilon_b-\epsilon_n\right)\left(\epsilon_a+\epsilon_b-\epsilon_n-\epsilon_m\right)}. \tag{5.46}$$

Similar to the symmetric diagram, we arrive at

$$A = \frac{4V^2}{(2\pi)^6} \int_{V<V_f} \mathrm{d}\boldsymbol{a} \int_{V>V_f} \mathrm{d}\boldsymbol{n} \frac{\left\langle na+Q|H^{\mathrm{dip}}|an+Q\right\rangle \Theta_{\boldsymbol{a}+\boldsymbol{Q}}\Theta^*_{\boldsymbol{n}+\boldsymbol{Q}}}{\left(Q^2+2\boldsymbol{n}\cdot\boldsymbol{Q}\right)\left(\boldsymbol{n}\cdot\boldsymbol{Q}-\boldsymbol{a}\cdot\boldsymbol{Q}\right)}, \tag{5.47}$$

with $\Theta^*_{\boldsymbol{a}} = \Theta\left(k_f^2-\boldsymbol{a}^2\right)$. A key difference is that we are left with one hole integral (a) and one particle integral (n). The integral over n goes from k_f to ∞. As in the symmetric case, A is split according to

$$A_{\uparrow\uparrow\uparrow\uparrow}, A_{\downarrow\downarrow\downarrow\downarrow}, -A_{\uparrow\downarrow\uparrow\downarrow}, -A_{\downarrow\uparrow\downarrow\uparrow} = \frac{\mu_{\mathrm{B}}^2}{12\pi^5} V\left(A_0-3A_z^q\right), \tag{5.48}$$

$$A_{\uparrow\downarrow\downarrow\uparrow}, A_{\downarrow\uparrow\uparrow\downarrow} = \frac{\mu_{\mathrm{B}}^2}{12\pi^5} V\left(2A_0-3A_x^q-3A_y^q\right). \tag{5.49}$$

Due to eq. 5.43 it is sufficient to only evaluate A_0 and A_z^q:

$$A_0 = \int_{V<V_f} \mathrm{d}\boldsymbol{a} \int_{V>V_f} \mathrm{d}\boldsymbol{n} \frac{\Theta_{\boldsymbol{a}+\boldsymbol{Q}}\Theta^*_{\boldsymbol{n}+\boldsymbol{Q}}}{\left(Q^2+2\boldsymbol{n}\cdot\boldsymbol{Q}\right)\left(\boldsymbol{n}\cdot\boldsymbol{Q}-\boldsymbol{a}\cdot\boldsymbol{Q}\right)}, \tag{5.50}$$

$$A_z^q = \int_{V<V_f} \mathrm{d}\boldsymbol{a} \int_{V>V_f} \mathrm{d}\boldsymbol{n} \frac{\left(q_z^2/q^2\right)\,\Theta_{\boldsymbol{a}+\boldsymbol{Q}}\Theta^*_{\boldsymbol{n}+\boldsymbol{Q}}}{\left(Q^2+2\boldsymbol{n}\cdot\boldsymbol{Q}\right)\left(\boldsymbol{n}\cdot\boldsymbol{Q}-\boldsymbol{a}\cdot\boldsymbol{Q}\right)}. \tag{5.51}$$

Again, A_0 will be calculated first and $\boldsymbol{Q} \parallel \boldsymbol{e}_z$ is assumed. In contrast to the symmetric diagram, we are now left with the evaluation of one particle and one hole integration. The particle integration has, however, a different area of integration. In the same way as eq. 5.37 was derived earlier, we can derive the boundaries also for a particle integration. The result is:

$$x = \cos\theta; x \in \left[-1, \frac{k_f^2-k_n^2-Q^2}{2k_nQ}\right]; k_n \in [k_f, k_f+Q]. \tag{5.52}$$

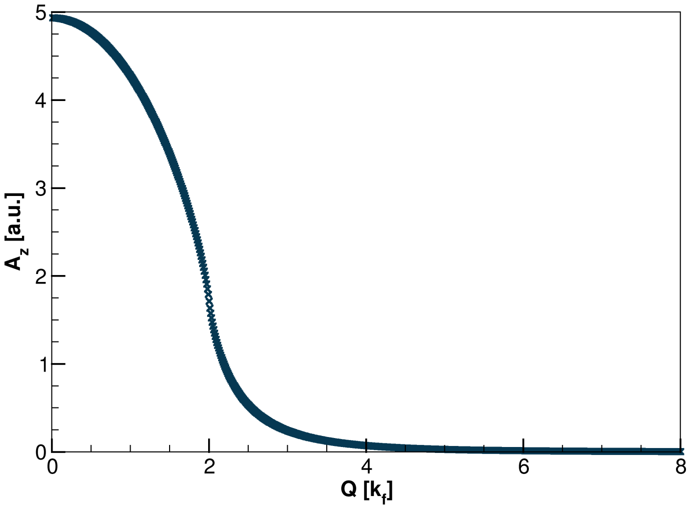

Figure 5.4
Numerical evaluation of the integral in eq. 5.56 as a function of Q. The Fermi energy is set to 1.

Therefore we obtain for the particle integration:

$$\int \mathrm{d}\boldsymbol{n}\ \Theta^*_{\boldsymbol{n}+\boldsymbol{Q}} = \int_{V_P} \mathrm{d}\boldsymbol{n} = \int_0^{2\pi} d\phi \int_{k_f}^{k_f+Q} \mathrm{d}\mathrm{n}\ n^2 \int_{-1}^{\left(k_f^2-n^2-Q^2\right)/(2nQ)} d\mathrm{x}. \tag{5.53}$$

A_0 is thus equivalent to:

$$\begin{aligned} A_0 &= \int_{V_H} \mathrm{d}\boldsymbol{a} \int_{V_P} \mathrm{d}\boldsymbol{n} \frac{1}{Q^2\left(Q+2nx_n\right)\left(nx_n-ax_a\right)} \\ &= \left[\pi \frac{\left(4k_fQ + (-4k_f^2+Q^2)\log\left[\left|\frac{2k_f-Q}{2k_f+Q}\right|\right]\right)}{8Q}\right]^2, \end{aligned} \tag{5.54}$$

which is the same result obtained for S_0 (eq. 5.40). We will evaluate A_z^q numerically. For the numerical integration, n is integrated over the area

$$\int_{V_P,\mathrm{cyl}} d^2\mathrm{a} = \int_{-\infty}^{\infty} \mathrm{dz} \int_0^{\infty} \mathrm{dr}\, \Theta\left(r^2+z^2-k_f^2\right) \Theta\left(k_f^2-r^2+z^2+2Qz+Q^2\right), \tag{5.55}$$

where the first Heaviside function constraints the integration to the particle region. From eqs. 5.41, 5.44, 5.51 and 5.55 follows:

$$A_z^q = \int_{V_H,\mathrm{cyl}} d^2\mathrm{a} \int_{V_P,\mathrm{cyl}} d^2\mathrm{n} \frac{4\pi^2\left(z_n-z_a\right)}{Q^2\left(Q+2z_n\right)\sqrt{\left(r_a^2+r_n^2+\left(z_a-z_n\right)^2\right)^2-4r_a^2r_n^2}} \tag{5.56}$$

The numerical evaluation of A_z^q is presented in fig. 5.4.

5.2.6 Yin-Yang and frog energy diagrams

The matrix in eq 5.23 only has one entry, $g^{00}_{\mathrm{YF}} = \uparrow\uparrow\uparrow\uparrow + \downarrow\downarrow\downarrow\downarrow + \uparrow\downarrow\downarrow\downarrow + \downarrow\uparrow\uparrow\uparrow$. We start with the derivation for the Yin-Yang diagrams, the result for the frog diagrams follows by analogy. We find that:

$$Y_{\uparrow\uparrow\uparrow\uparrow}, Y_{\downarrow\downarrow\downarrow\downarrow} = \frac{\mu_{\mathrm{B}}^2}{12\pi^5} V \left(Y_0 - 3Y_z^q\right), \tag{5.57}$$

$$Y_{\uparrow\downarrow\downarrow\downarrow}, Y_{\downarrow\uparrow\uparrow\uparrow} = \frac{\mu_{\mathrm{B}}^2}{12\pi^5} V \left(2Y_0 - 3Y_x^q - 3Y_y^q\right). \tag{5.58}$$

As the Yin-Yang diagrams do not have a denominator that depends on ϕ or ϕ', equation 5.43 holds, therefore:

$$g_Y^{00} = \frac{\mu_{\mathrm{B}}^2}{12\pi^5} V \left(-3Y_x^q - 3Y_y^q - 3Y_z^q + 3Y_0\right) = \frac{\mu_{\mathrm{B}}^2}{12\pi^5} V \left(-3Y_0 + 3Y_0\right) = 0. \tag{5.59}$$

It is simple to show that the frog diagrams vanish due to the same identity. The physical interpretation for this is that neither the Yin-Yang nor the frog diagram can spin-polarize the system, as conservation of spin forces them to undo any spin-flips. The result is that these diagrams do not contribute to a purely magnetic interaction.

5.2.7 Exact numerical and semi-analytical solution

All that is left to do is combining the results for the symmetric and the asymmetric diagram. Using the results from the previous chapters, the matrix g (eq. 5.22) can be calculated from eqs. 5.30, 5.31, 5.40, 5.45, 5.48, 5.49, 5.54, 5.56 and tbl. 5.2:

$$g^{00} = \frac{\mu_{\mathrm{B}}^2}{12\pi^5} V \left(-3S_x^q - 3S_y^q - 3S_z^q + 3S_0 - 3A_x^q - 3A_y^q - 3A_z^q + 3A_0\right) = 0 \tag{5.60}$$

$$g^{11} = -\frac{\mu_{\mathrm{B}}^2}{6\pi^5} V \left(S_0 + A_0 - 3S_z^q - 3A_z^q\right) \tag{5.61}$$

$$\begin{aligned} g^{33} &= \frac{\mu_{\mathrm{B}}^2}{12\pi^5} V \left[2\left(S_0 - 3S_z^q + A_0 - 3A_z^q\right) - 2\left(2S_0 - 3S_x^q - 3S_y^q + 2A_0 - 3A_x^q - 3A_y^q\right)\right] \\ &= \frac{2\mu_{\mathrm{B}}^2}{6\pi^5} V \left(\left(S_0 + A_0\right) - 3\left(S_z^q + A_z^q\right)\right) = -2g^{11} \end{aligned} \tag{5.62}$$

Here we used eq. 5.43 to simplify g^{33}.
With the definition $S + A = (S_0 + A_0) - 3\left(S_z^q + A_z^q\right)$ we obtain:

$$g = \frac{\mu_{\mathrm{B}}^2}{6\pi^5} V \begin{pmatrix} 0 & 0 & 0 & 0 \\ 0 & -(S+A) & 0 & 0 \\ 0 & 0 & -(S+A) & 0 \\ 0 & 0 & 0 & 2(S+A) \end{pmatrix}. \tag{5.63}$$

The total result for g^{33} shown in fig. 5.5. Fig. 5.5 also shows a comparison with a semi-analytic result, up to an integral, which was derived by a co-worker via

Feynman diagrams. This is possible because the second order change in the energy can be identified with the interacting response function, $\delta^2 E = \frac{1}{2}\chi\left(\boldsymbol{q}\right)\delta v_{\boldsymbol{q}}\delta v_{-\boldsymbol{q}}$, via the Hellmann-Feynman theorem [101]. In this case, only the Feynman exchange-diagram was evaluated. The semi-analytic result reads (with $q = Q/k_f$):

$$\begin{aligned} g^{33} = \frac{\mu_{\mathrm{B}}^2 k_f^2}{8\pi^3 q^2}\Bigg\{ & \frac{4}{45}\left(-18+11q^2\right)+\frac{4}{45}q^2\left(60+7q^2\right)\log\left[2/q\right] \\ & + \frac{2}{45q}\left(-144-20q^2+30q^3-15q^4+7q^5\right)\log\left[\left|1-q/2\right|\right] \\ & + \frac{2}{45q}(144+20q^2+30q^3+15q^4+7q^5)\log\left[\left|1+q/2\right|\right] \\ & + \frac{16}{3}q\Big(\left(1-q/2\right)^3\log\left[\left|1-2/q\right|\right]\log\left[\left|1-q/2\right|\right] \\ & -(1+q/2)^3\log\left(\left|1+2/q\right|\right]\log\left[\left|1+q/2\right|\right]\Big) \\ & - \frac{4}{3}\left(q+\left(1-q^2/4\right)\log\left[\left|\frac{2+q}{2-q}\right|\right]\right)^2 \\ & + \int_{q/2-1}^{q/2+1}\mathrm{d}z\,8z\log\left[\left|z\right|\right]\Bigg(\left(1-\frac{1}{4}\left(q-2z\right)^2\right)\log\left[\left|\frac{q-2z-2}{q-2z+2}\right|\right] \\ & + \left(1-\frac{1}{4}\left(q+2z\right)^2\right)\log\left[\left|\frac{q+2z-2}{q+2z+2}\right|\right]\Bigg)\Bigg\}. \end{aligned} \tag{5.64}$$

We achieve an excellent agreement between the numerical and the analytical results, which have been derived independently with separate methods. As we are mostly interested in large length-scales, we are interested in the behavior of g^{33} for small $\boldsymbol{Q}$. We fit the function $f\left(x\right) = a + bx^2 + cx^2\log\left|x\right|$ to the numerical data of g^{33} close to $\boldsymbol{Q} = 0$. Neither a constant nor a linear term are expected. A constant term would violate that the energy contribution vanishes as $Q \to 0$, while a linear term would imply that the direction of the perturbation to the homogeneous electron gas matters. The result of the fit is shown in fig. 5.6a. The parameters obtained from the fit are:

$$S + A = -1,2\cdot 10^{-12} - 2.015\cdot 10^{-3}\left(\frac{Q}{k_f}\right)^2 + 7.16\cdot 10^{-4}\left(\frac{Q}{k_f}\right)^2\log\left|\frac{Q}{k_f}\right|. \tag{5.65}$$

We can compare our results to a taylor expansion of the analytic result (eq. 5.64), for which, as $q \to 0$, we find that:

$$g^{33} = k_f^2\frac{\left[127+60\log\left(2\right)-60\log\left(q\right)\right]}{2700\pi^3}q^2 + \mathcal{O}\left(q^4\right) \tag{5.66}$$

$$\overset{k_f=1}{\approx} -2.014\cdot 10^{-3}\left(\frac{Q}{k_f}\right)^2 + 7.17\cdot 10^{-4}\left(\frac{Q}{k_f}\right)^2\log\left|\frac{Q}{k_f}\right|, \tag{5.67}$$

which agrees very well with the numerical values obtained in this thesis. An interesting observation is that g is continuous, but non-analytic at $Q = 0$ due to the

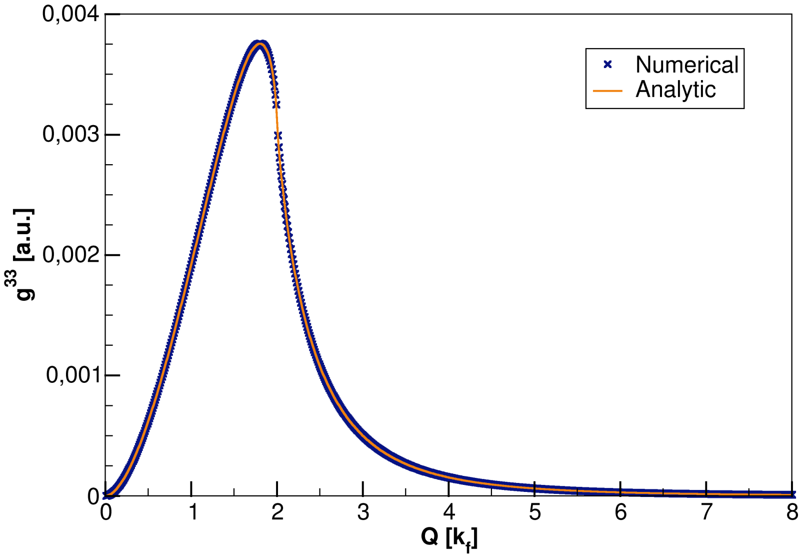

Figure 5.5
Comparison g^{33} (eqs. 5.14, 5.62), obtained with a numerical evaluation of the Goldstone diagrams and with an analytical result obtained via Feynman diagrams for $k_f = 1$. Excellent agreement is obtained.

term $q^2 \log(|q|)$. This term does keep the correct symmetry and is even dominant for small values of q. It can therefore not be neglected. This should, however, not result in any practical limitations for the use of our functional. For completeness, we also compute the expansion in the $q \to \infty$ limit and find:

$$g^{33} = \frac{32k_f^2}{27\pi^3 q^4} + \mathcal{O}\left(\frac{1}{q^6}\right), \tag{5.68}$$

g is connected with the exchange kernel via the response function (eq. 5.14). The response of a non-interacting, homogeneous electron gas is well studied in various literature. For a plane wave perturbation, like in this case, the non-interacting response function is given by the Lindhard susceptibility [102]:

$$\chi_0(\boldsymbol{Q}) = -\frac{k_f}{2\pi^2}\left[\frac{1}{2} + \frac{4k_f^2 - Q^2}{8k_f Q}\ln\left|\frac{2k_f + Q}{2k_f - Q}\right|\right]. \tag{5.69}$$

In the homogeneous, paramagnetic case, the non-interacting response matrix reads [102]:

$$\chi_0 = \chi_0(\boldsymbol{Q})\begin{pmatrix}1 & 0 & 0 & 0\\ 0 & 1 & 0 & 0\\ 0 & 0 & 1 & 0\\ 0 & 0 & 0 & 1\end{pmatrix}. \tag{5.70}$$

Thus the exchange kernel for H^{dip} (eq. 5.2) is approximately (eq. 5.14):

$$f_x = g\,(\chi_0)^{-1}\,(\chi_0)^{-1}. \tag{5.71}$$

The energy functional for the dipole exchange energy is then given by equation 5.15. When using the Lindhard function, due to the prefactor k_f, f_x can be expressed solely by $q = Q/k_f$. The result for f_x^{33} is shown in fig. 5.6b. As we are interested in the long-range behavior, we calculate the matrix f_x in the $q \to 0$ limit and find:

$$f_x = \frac{1}{675}\pi \left(127 + 60 \log\left(2\right) - 60 \log\left[q\right]\right) q^2 \begin{pmatrix} 0 & 0 & 0 & 0 \\ 0 & 1 & 0 & 0 \\ 0 & 0 & 1 & 0 \\ 0 & 0 & 0 & 2 \end{pmatrix} + \mathcal{O}\left(q^4\right). \tag{5.72}$$

For completeness, we state f_x in the $q \to \infty$ limit:

$$f_x = \frac{8\pi}{3} - \frac{232\pi}{75q^2} \begin{pmatrix} 0 & 0 & 0 & 0 \\ 0 & 1 & 0 & 0 \\ 0 & 0 & 1 & 0 \\ 0 & 0 & 0 & 2 \end{pmatrix} + \mathcal{O}\left(\frac{1}{q^4}\right). \tag{5.73}$$

Together with eq. 5.15, eqs. 5.72, 5.73 are the final form of our functional. More sophisticated approximations are conceivable, for example one could try to use an interacting response function instead of the Lindhard function to obtain f_x from g (eq. 5.15).

We conclude by noting that a similar long-range functional can be easily derived for the Coulomb interaction. For this, one can use again the identity originating from the Hellman-Feynman theorem, $\delta^2 E = \frac{1}{2}\chi\left(\boldsymbol{q}\right)\delta v_{\boldsymbol{q}} \delta v_{-\boldsymbol{q}}$ [101], to obtain the change in energy from the response function and then use eqs. 5.14, 5.15. The exchange contribution to the response function has been derived previously [103–105]. Such a functional could be used alongside a local functional, e.g. the LDA, to account for long-range Coulomb exchange effects.

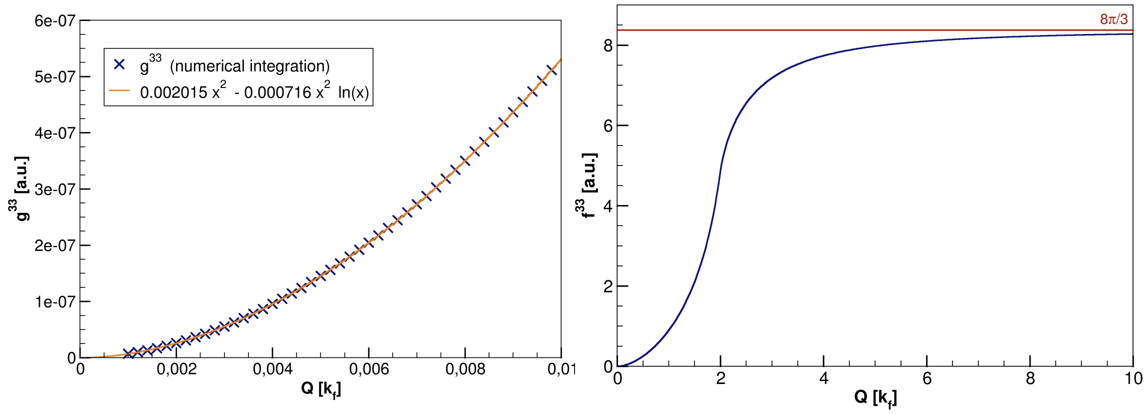

(a) (b)

Figure 5.6
a) Numerical evaluation of g_{33}. The Fermi energy is set to 1. The function $k_f(x) = a + bx^2 + cx^2 \log|x|$ is fitted to the data. The fit is restricted to small perturbations, $Q/k_f \leq 1/100$. All integrals were evaluated with a precision and accuracy of 8 digits. The fit shows excellent agreement with the numerical data. b) f_x^{33} (eq. 5.14) as a function of Q. The Lindhard function (eq. 5.69) was used as an approximation to obtain f_x^{33} from g^{33}. Due to the prefactor k_f of the Lindhard function, f_x^{33} only depends on Q/k_f.

5.3 Correlation energy and higher orders

We observed that in homogeneous systems both, the mean-field energy (eq. 4.5) and the exchange energy (eq. 5.10) of H^{dip} (eq. 5.2) are zero. In this section, we will investigate whether the H^{dip} has a finite contribution to the correlation energy for homogeneous systems. The lowest order Goldstone diagrams associated with the correlation energy are shown in fig. 5.7. Some of them include mixed Coulomb/dipole interactions. The H^{dip} is again indicated by a dashed line, whereas we use a wavy line for the Coulomb interaction.

Diagram a)

It turns out that the lowest order energy contribution to the homogeneous electron gas arising from H^{dip} is given by diagram 5.7a. The energy associated with this diagram is given by

$$E_a = \frac{(-1)^4}{4} \sum_{\boldsymbol{k},\boldsymbol{l},\boldsymbol{m},\boldsymbol{n}} \frac{\left\langle mn \left| H^{\mathrm{dip}} \right| kl \right\rangle \left\langle kl \left| H^{\mathrm{dip}} \right| mn \right\rangle}{\left(\epsilon_{\boldsymbol{k}} + \epsilon_{\boldsymbol{l}} - \epsilon_m - \epsilon_n\right)}, \tag{5.74}$$

which after carrying out spin summations (tbl. 5.5) becomes

$$E_a = \frac{1}{4} \frac{\mu_{\mathrm{B}}^4}{V^2} \sum_{\boldsymbol{k},\boldsymbol{l},\boldsymbol{q}} \frac{4\eta_z^2(\boldsymbol{q}) + 2\left(\eta_x(\boldsymbol{q}) + \eta_y(\boldsymbol{q})\right)^2}{\left(\epsilon_{\boldsymbol{k}} + \epsilon_{\boldsymbol{l}} - \epsilon_{\boldsymbol{k}+\boldsymbol{q}} - \epsilon_{\boldsymbol{l}-\boldsymbol{q}}\right)} \Theta_{\boldsymbol{k}+\boldsymbol{q}} \Theta_{\boldsymbol{l}-\boldsymbol{q}}, \tag{5.75}$$

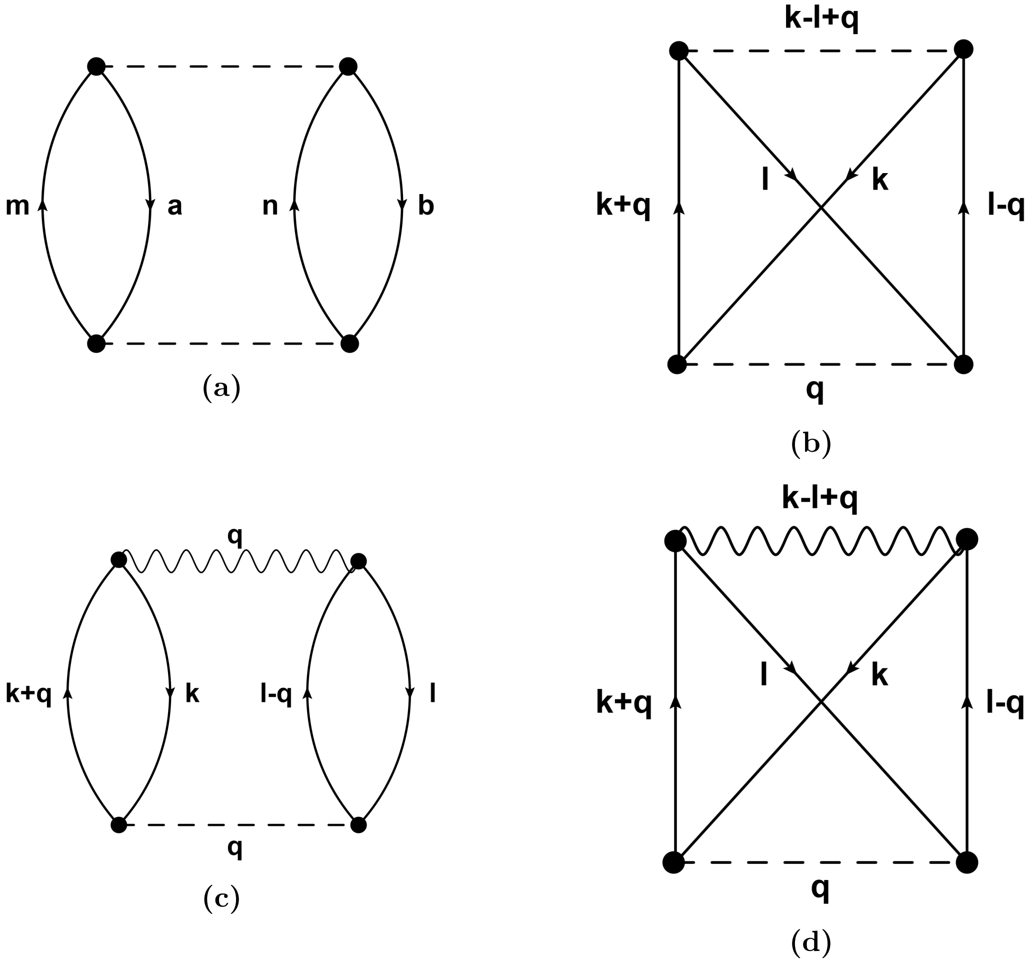
m
a
n
b
(a)
k-l+q
k+q
l
k
l-q
q
(b)
q
k+q
k
l-q
l
q
(c)
k-l+q
k+q
l
k
l-q
q
(d)

Figure 5.7
All distinct second order correlation energy diagrams. Dashed lines indicate dipole interactions, wiggly lines indicate Coulomb interactions.

Table 5.5
All possible spin combinations for diagram 5.7a.

k+q	k	l-q	l	contribution
↑	↑	↑	↑	η_z^2
↓	↓	↓	↓	η_z^2
↑	↑	↓	↓	η_z^2
↓	↓	↑	↑	η_z^2
↑	↓	↓	↑	$(\eta_x + \eta_y)^2$
↓	↑	↑	↓	$(\eta_x + \eta_y)^2$

where $|\boldsymbol{k}|, |\boldsymbol{l}| < k_f$, and $|\boldsymbol{q}| = \boldsymbol{m} - \boldsymbol{k} < 2k_f$. By using the continuum limit $\sum_i \rightarrow V/(2\pi)^3 \int \mathrm{d}\boldsymbol{i}$ for $\boldsymbol{k}, \boldsymbol{l}, \boldsymbol{q}$ and the dispersion relation of the homogeneous electron gas, $\epsilon_{\boldsymbol{k}} = \boldsymbol{k}^2/2$ we obtain:

$$E_a = -\frac{\mu_{\mathrm{B}}^4 V}{4(2\pi)^9} \int \mathrm{d}\boldsymbol{q} \int \mathrm{d}\boldsymbol{k} \int \mathrm{d}\boldsymbol{l} \frac{4\eta_z^2(\boldsymbol{q}) + 2(\eta_x(\boldsymbol{q}) + \eta_y(\boldsymbol{q}))^2}{q^2 + (\boldsymbol{k} - \boldsymbol{l}) \cdot \boldsymbol{q}} \Theta_{\boldsymbol{k}+\boldsymbol{q}} \Theta_{\boldsymbol{l}-\boldsymbol{q}}. \tag{5.76}$$

For the $\boldsymbol{k}$-integration we can again use the parametrization for hole integrals (eq. 5.37) and for the $\boldsymbol{l}$-integration we have

$$x_l = \cos\theta_l; x_l \in \left[-1, \frac{-k_f^2 + l^2 + Q^2}{2lQ},\right]; l \in [k_f, k_f + Q]. \tag{5.77}$$

Integrating the $\boldsymbol{l}, \boldsymbol{k}$-dependent parts yields

$$\int \mathrm{d}\boldsymbol{k} \int \mathrm{d}\boldsymbol{l} \frac{\Theta_{\boldsymbol{k}+\boldsymbol{q}} \Theta_{\boldsymbol{l}-\boldsymbol{q}}}{q^2 + (\boldsymbol{k} - \boldsymbol{l}) \cdot \boldsymbol{q}} = \frac{\pi^2}{120q^2} \left\{ \left(120k_f^4 q^2 - 20k_f^2 q^4 + \frac{3}{2}q^6\right) \ln\left[\frac{2k_f + q}{2k_f - q}\right] + \right.$$
$$\left. 2k_f \left(-3q^5 + 4k_f^2 q^3 (29 - 40\ln(2)) - 128k_f^4 q \ln(2) + 64k_f^4 q \ln\left[4 - \frac{q^2}{k_f^2}\right]\right)\right\}. \tag{5.78}$$

We can now solve the angular $\boldsymbol{q}$-integrations in equation 5.76 by introducing spherical harmonics:

$$\int_0^\pi \mathrm{d}\theta \int_0^{2\pi} \mathrm{d}\phi \sin(\theta) \left(4\eta_z^2(\boldsymbol{q}) + 2(\eta_x(\boldsymbol{q}) + \eta_y(\boldsymbol{q}))^2\right)$$
$$= \int_0^\pi \mathrm{d}\theta \int_0^{2\pi} \mathrm{d}\phi \sin(\theta) \frac{8\pi^2}{3} (1 + 3\cos(2\theta))^2 = \frac{512\pi^3}{15}. \tag{5.79}$$

Therefore the remaining integral from eq. 5.76 is

$$E_a = -\frac{\mu_{\mathrm{B}}^4 V}{4(2\pi)^9} \int_0^{2k_f} \mathrm{d}q \frac{512\pi^3}{15} \frac{\pi^2}{120} \left\{ \left(120k_f^4 q^2 - 20k_f^2 q^4 + \frac{3}{2}q^6\right) \ln\left[\frac{2k_f + q}{2k_f - q}\right] + \right.$$
$$\left. 2k_f \left(-3q^5 + 4k_f^2 q^3 (29 - 40\ln(2)) - 128k_f^4 q \ln(2) + 64k_f^4 q \ln\left[4 - \frac{q^2}{k_f^2}\right]\right) . \right\} \tag{5.80}$$

With the final result:

$$E_a = -\frac{4(43 - 46\ln(2))}{1575\pi^4} \mu_{\mathrm{B}}^4 k_f^7 V. \tag{5.81}$$

This is the lowest-order energy contribution of H^{dip} to the homogeneous electron gas.

Diagrams b), c), d)

We will show in the following that all other second-order correlation diagrams are zero. We start with diagram b) (5.7b), which is equivalent to

$$E_b = (-1)^3 \times \frac{\mu_{\mathrm{B}}^4}{4} \sum_{i \leq j} \sum_{\boldsymbol{q},\boldsymbol{k},\boldsymbol{l}} \frac{2\eta_i\left(\boldsymbol{q}\right)\eta_j\left(\boldsymbol{k}-\boldsymbol{l}+\boldsymbol{q}\right)}{\left(\epsilon_{\boldsymbol{k}}+\epsilon_{\boldsymbol{l}}-\epsilon_{\boldsymbol{k}+\boldsymbol{q}}-\epsilon_{\boldsymbol{l}-\boldsymbol{q}}\right)}, \tag{5.82}$$

where $i, j = x, y, z$. Taking the continuum limit for a given i, j yields

$$E_b^{i,j} = \frac{-\mu_{\mathrm{B}}^4}{\left(2\pi\right)^9} \int \mathrm{d}\boldsymbol{q}\; \eta_i\left(\boldsymbol{q}\right) \int \mathrm{d}\boldsymbol{k} \int \mathrm{d}\boldsymbol{l} \frac{\Theta_{\boldsymbol{k}+\boldsymbol{q}}\Theta_{\boldsymbol{l}-\boldsymbol{q}}}{q^2+\left(\boldsymbol{k}-\boldsymbol{l}\right)\cdot\boldsymbol{q}} \eta_j\left(\boldsymbol{k}-\boldsymbol{l}+\boldsymbol{q}\right), \tag{5.83}$$

which we can rewrite as an integral over all space by introducing additional Heaviside functions:

$$E_b^{i,j} = \frac{-\mu_{\mathrm{B}}^4}{\left(2\pi\right)^9} \int \mathrm{d}\boldsymbol{q}\; \eta_i\left(\boldsymbol{q}\right) \int_{all} \mathrm{d}\boldsymbol{k} \int_{all} \mathrm{d}\boldsymbol{l} \frac{\Theta_{\boldsymbol{k}+\boldsymbol{q}}\Theta_{\boldsymbol{l}-\boldsymbol{q}}\Theta^*_{\boldsymbol{k}}\Theta^*_{\boldsymbol{l}}}{q^2+\left(\boldsymbol{k}-\boldsymbol{l}\right)\cdot\boldsymbol{q}} \eta_j\left(\boldsymbol{k}-\boldsymbol{l}+\boldsymbol{q}\right). \tag{5.84}$$

Using the transformations $\boldsymbol{k} \to \boldsymbol{k} - \boldsymbol{q}/2$ and $\boldsymbol{l} \to \boldsymbol{l} + \boldsymbol{q}/2$ then results in:

$$E_b^{i,j} = \frac{-\mu_{\mathrm{B}}^4}{\left(2\pi\right)^9} \int \mathrm{d}\boldsymbol{q}\; \eta_i\left(\boldsymbol{q}\right) \int_{all} \mathrm{d}\boldsymbol{k} \int_{all} \mathrm{d}\boldsymbol{l} \frac{\Theta_{\boldsymbol{k}+\boldsymbol{q}/2}\Theta_{\boldsymbol{k}+\boldsymbol{q}/2}\Theta^*_{\boldsymbol{k}-\boldsymbol{q}/2}\Theta^*_{\boldsymbol{l}+\boldsymbol{q}/2}}{\boldsymbol{k}\cdot\boldsymbol{q}-\boldsymbol{l}\cdot\boldsymbol{q}} \eta_j\left(\boldsymbol{k}-\boldsymbol{l}\right). \tag{5.85}$$

Assuming $\boldsymbol{q} \parallel \boldsymbol{e}_z$ for the integrations over $\boldsymbol{k}, \boldsymbol{l}$ the following form is obtained

$$E_b^{i,j} = \frac{-\mu_{\mathrm{B}}^4}{\left(2\pi\right)^9} \int \mathrm{d}\boldsymbol{q}\; \eta_i\left(\boldsymbol{q}\right) h\left(\left|\boldsymbol{q}\right|\right) = 0, \tag{5.86}$$

where h is some function that only depends on the magnitude of $\boldsymbol{q}$. As a full angular integration over η_i vanishes, diagram 5.7b does not contribute to the correlation energy.

Similarly, it is possible to prove that all diagrams involving only one dipole interaction are zero (thus also the diagrams 5.7c, 5.7d). This can be seen by considering the diagram shown in fig. 5.8a. The continuum limit of such a diagram takes the following form

$$E \propto \int \mathrm{d}\boldsymbol{q} \left(1 - 3\frac{q_z^2}{q^2}\right) \int \mathrm{d}\boldsymbol{k} \int \mathrm{d}\boldsymbol{l} \int \mathrm{d}\boldsymbol{a}_1 \cdots \int \mathrm{d}\boldsymbol{a}_n \int \mathrm{d}\boldsymbol{m}_1 \cdots \int \mathrm{d}\boldsymbol{m}_n \frac{V_c}{D}, \tag{5.87}$$

where $\boldsymbol{a}$ and $\boldsymbol{m}$ are arbitrary hole and particle integrations, respectively. V_c is comprised of all occurring Coulomb interactions and D is the denominator of the diagram. When using plane waves, V_c and D share the property of being a product of squared momenta

$$V_c \propto \prod_n \frac{1}{\sum_i \boldsymbol{k}_i \sum_j \boldsymbol{k}_j}, D \propto \prod_n \left(\sum_i \boldsymbol{k}_i^2 - \sum_j \boldsymbol{k}_j^2\right), \tag{5.88}$$

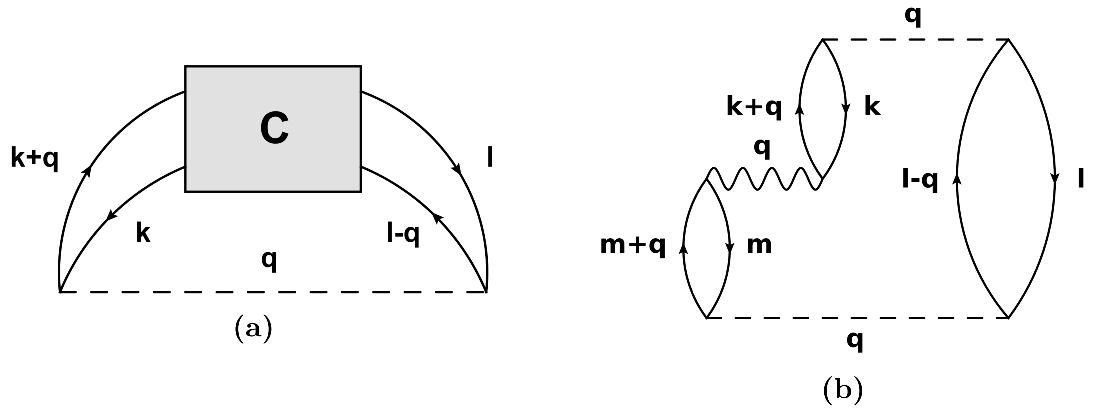

Figure 5.8
a) A general diagram consisting of a single dipole interaction and an arbitrary arrangement of Coulomb interactions (box). This diagram is zero due to the angular integration over the dipole interaction. b) A non-vanishing third order diagram that mixes the Coulomb and the dipole interaction.

where $\boldsymbol{k}_i$ are arbitrary particle or hole momenta. The only explicitly $\boldsymbol{q}$-dependent terms are therefore of the form q^2 and $\boldsymbol{q} \cdot \boldsymbol{k}_i$. Accordingly, when choosing the coordinate system such that $q \parallel \boldsymbol{e}_z$ for all integrals but the q-integration, the form of eq. 5.86 is always recovered. This is physically intuitive, as it was already observed for the exchange interaction that a single dipole interaction leads to integrating a spherical harmonic over all angles. As the Coulomb interaction is isotropic, no additional angular dependence is introduced, regardless of the number of Coulomb interactions. A finite mixing between the dipole and the Coulomb interaction can be observed at higher orders when more than a single dipole interaction are present. One example is given in fig. 5.8b.

5.4 Spin-contact interaction

We have seen that the lowest order energy contribution of the non-local part of the MDI (H^{dip} eq. 5.2) is the correlation energy. A finite exchange energy, does however, arise from the spin-contact contribution, which we will derive in the following. The spin-contact contribution is given by (eq. 4.1)

$$H^{\text{SC}} = -\frac{4\pi}{3}\mu_{\text{B}}^2 \sum_{i\neq j} \delta\left(\boldsymbol{r}_i - \boldsymbol{r}_j\right) \boldsymbol{\sigma}_i \cdot \boldsymbol{\sigma}_j, \tag{5.89}$$

with the the direct energy contribution (eq. 4.2)

$$E_{\text{D}}^{\text{xc}}\left[\boldsymbol{m}\right] = -\frac{4\pi}{3}\mu_B^2 \int \mathrm{d}\boldsymbol{r}\, \boldsymbol{m}^2\left(\boldsymbol{r}\right). \tag{5.90}$$

As stated previously, this term also appears in classical electrodynamics and guarantees the correct limit of the MDI as $\boldsymbol{r} \to \boldsymbol{r'}$ [37]. This term is similar to the more well-known “Fermi contact interaction”, which gives rise to the hyperfine splitting of electronic s states [57, 106]. In that case, however, one has to consider the overlap of the electronic spin with the nuclear spin instead of the overlap of two electronic spins.

In the present case of purely electronic interactions, exchange and correlation effects exist as well. The exchange energy for the spin-contact interaction can be evaluated exactly. We use the formula for the exchange energy (eq. 5.3) and find:

$$E_{\mathrm{x}}^{\mathrm{sc}} = \frac{4\pi}{3}\mu_{\mathrm{B}}^2 \sum_{\substack{i\neq j\\ ss'}} \int \mathrm{d}\boldsymbol{r} \int \mathrm{d}\boldsymbol{r'}\, \varphi_i^\dagger\left(\boldsymbol{r},s\right) \boldsymbol{\sigma}_j \varphi_j^\dagger\left(\boldsymbol{r'},s'\right) \delta\left(\boldsymbol{r}-\boldsymbol{r'}\right) \varphi_j\left(\boldsymbol{r},s'\right) \boldsymbol{\sigma}_i \varphi_i\left(\boldsymbol{r'},s\right). \tag{5.91}$$

Evaluating the trivial integral and summing over all spins yields:

$$\begin{aligned} E_{\mathrm{x}}^{\mathrm{sc}} = \frac{4\pi}{3}\mu_{\mathrm{B}}^2 \sum_{i\neq j} \int \mathrm{d}\boldsymbol{r}\, & 2\varphi_i^\dagger(\uparrow)\varphi_i(\uparrow)\varphi_j^\dagger(\downarrow)\varphi_j(\downarrow) + 2\varphi_i^\dagger(\downarrow)\varphi_i(\downarrow)\varphi_j^\dagger(\uparrow)\varphi_j(\uparrow) \\ & + \varphi_i^\dagger(\uparrow)\varphi_i(\uparrow)\varphi_j^\dagger(\uparrow)\varphi_j(\uparrow) + \varphi_i^\dagger(\downarrow)\varphi_i(\downarrow)\varphi_j^\dagger(\downarrow)\varphi_j(\downarrow). \end{aligned} \tag{5.92}$$

The exchange functional is then given by:

$$\begin{aligned} E_{\mathrm{x}}^{\mathrm{sc}} &= \frac{4\pi}{3}\mu_{\mathrm{B}}^2 \int \mathrm{d}\boldsymbol{r}\, 4n_\uparrow(\boldsymbol{r})\, n_\downarrow(\boldsymbol{r}) + n_\uparrow^2(\boldsymbol{r}) + n_\downarrow^2(\boldsymbol{r}) \\ &= \frac{4\pi}{3}\mu_{\mathrm{B}}^2 \int \mathrm{d}\boldsymbol{r}\, \frac{3}{2}\left(n_\uparrow + n_\downarrow\right)^2 - \frac{1}{2}\left(n_\uparrow - n_\downarrow\right)^2 \\ \Longrightarrow\ E_{\mathrm{x}}^{\mathrm{sc}}\left[n,\boldsymbol{m}\right] &= \frac{2\pi}{3}\mu_{\mathrm{B}}^2 \int \mathrm{d}\boldsymbol{r}\, 3n^2(\boldsymbol{r}) - \boldsymbol{m}^2(\boldsymbol{r}). \end{aligned} \tag{5.93}$$

It is easy to verify that there is no self-interaction for a one-electron system from eqs. 5.90 and 5.93, as is expected for the exact exchange energy functional:

$$E^{\mathrm{sc}} = E_{\mathrm{D}}^{\mathrm{sc}} + E_{\mathrm{x}}^{\mathrm{sc}} = 2\pi\mu_{\mathrm{B}}^2 \int \mathrm{d}\boldsymbol{r}\, n^2(\boldsymbol{r}) - \boldsymbol{m}^2(\boldsymbol{r}). \tag{5.94}$$

We emphasize, however, that the direct interaction is already included when solving eq. 4.4. It should therefore not be included again to avoid double counting. As the spin-contact exchange energy (eq. 5.93) does not only depend on the magnetization $\boldsymbol{m}$ but also depends on the electronic density n, one may consider to also include the Coulomb contact interaction (“two-particle Darwin-interaction”) (cf. 2.4):

$$H^{\mathrm{cc}} = -2\pi\mu_{\mathrm{B}}^2 \sum_{i\neq j} \delta\left(\boldsymbol{r_i} - \boldsymbol{r_j}\right). \tag{5.95}$$

By including this, the Coulomb and the MDI are treated consistently up to second order. We can easily derive the direct interaction and the exchange interaction for the two-particle Darwin-interaction:

$$\begin{aligned} E^{\mathrm{cc}}\left[n(\boldsymbol{r}),\boldsymbol{m}(\boldsymbol{r})\right] &= E_{\mathrm{D}}^{\mathrm{cc}} + E_{\mathrm{x}}^{\mathrm{cc}} \\ &= -2\pi\mu_{\mathrm{B}}^2 \int \mathrm{d}\boldsymbol{r}\, n^2(\boldsymbol{r}) + 2\pi\mu_{\mathrm{B}}^2 \int \mathrm{d}\boldsymbol{r}\, \frac{n^2(\boldsymbol{r}) + \boldsymbol{m}^2(\boldsymbol{r})}{2} \\ &= \pi\mu_{\mathrm{B}}^2 \int \mathrm{d}\boldsymbol{r}\, \boldsymbol{m}^2(\boldsymbol{r}) - n^2(\boldsymbol{r}). \end{aligned} \tag{5.96}$$

It is again easy to see that there is no self-interaction for a single particle. The contact interactions (eqs. 5.94, 5.96) have to be included to treat the Coulomb and the MDI consistently up to second order. Their contribution is expected to be negligible, however, as they are inherently local and will thus be dominated by the Hartree and the Coulomb exchange interaction.

6. Conclusion

The aim of this thesis was to obtain a more in-depth, microscopic understanding of magnetic effects relevant for future information technology. To that end we pursued two main approaches: First, we performed simulations of ultrafast demagnetization, which is among the fastest known effects of changing the magnetization in a sample. Second, we derived and implemented a system of ultra long-range Kohn-Sham equations which could make the quantum mechanical calculation of magnetic domains possible. It could also allow for improved calculations of ultrafast demagnetization and light-matter interactions in general, as a coupling to Maxwell's equations becomes computationally feasible.

We started with a general introduction into many-particle systems in chapter 2. We continued with a discussion on density functional theory and its time-dependent generalization, time-dependent density functional theory. We highlighted the most important relativistic terms up to second order and concluded the chapter with a brief description of our implementation.

In chapter 3, we started with a basic introduction into the field of ultrafast magneto-optics. We revisited some of the most common measurement techniques, including the Faraday effect, the magneto-optic Kerr effect and magnetic second harmonic generation. We motivated how a magnetization may lead to a change in the ellipticity and the orientation angle of transmitted or reflected polarized light. We then showcased our time-dependent spin density functional theory approach to ultrafast demagnetization and provided detailed explanations for all relevant approximations. The central results in the chapter were obtained by two joint experimental/theoretical studies. In our first study, we were able to explain the different observed demagnetization behavior in Ni and Co due to different spin-orbit coupling time scales. Furthermore, we found both experimental and theoretical evidence that ultrafast demagnetization generally cannot be described by a flow of majority spins alone. Our results thus strongly oppose the validity of the superdiffusive model but instead favor spin-orbit coupling mediated spin flips alongside spin currents in both spin channels as the central mechanisms. In our second study, we investigated thin films of Co on top of Cu(001). In the experiment, 3 or 5 layers of Co and a Cu bulk substrate were used. For our theoretical simulations, we considered 3 or 5 layers of Co on top of 7 layers of Cu. We achieved the hitherto best reported quantitative agreement between theoretical simulations and experimental magnetic second harmonic generation results. Furthermore, we were able to distinguish all relevant microscopic process at the interface during the early times $t < 100\,\mathrm{fs}$. During the first 35 fs, we find a flow of majority spins from Co to Cu and a backflow of minority spins from Cu to Co leading to an initial demagnetization. Between 35 fs and 100 fs we identified spin-orbit coupling as the main driving mechanism for further, subsequent demagnetization. These results are in accordance with the result obtained in our first study and rule out explanations of ultrafast demagnetization which take only a single spin channel into account.

In chapter 4 we presented a numerical approach for solving ultra long-range phenomena within density functional theory. Our approach relies on a length-scale separation in reciprocal space: In addition to the normal $\boldsymbol{k}$-point grid, we employ a closely packed $\boldsymbol{\kappa}$-point grid, which we use to sample effects on large length-scales. From this, we derived a set of self-consistent long range Kohn-Sham equations. All observables in our ultra long-range system are given by a Fourier series with lattice periodic Fourier coefficients. We demonstrated the accuracy of our approach via a direct comparison with supercell calculations. We found that our approach can quantitatively reproduce spin spirals in γ-Fe and still delivers good results for the very difficult case of spin-density waves in Cr. Our method is highly efficient and allowed us to solve over 6000 unit cells of bulk Li subjected to an external electric field in slightly under 50 hours. We also discussed a possible generalization to time-dependent systems and the limits of our approach.

Finally, in chapter 5, we derived an exchange functional for the magnetic dipole interaction to be used alongside with our ultra long-range Kohn-Sham system introduced in chapter 4. We showed that a local density approximation for the magnetic dipole interaction only arises from the spin-contact interaction. We then proceeded with calculating a perturbative exchange functional up to second order in external perturbations employing Goldstone diagrams. Furthermore, we managed to prove that the lowest order non-local energy contribution from the magnetic dipole interaction to the homogeneous electron gas is given by diagrams of second order in the interaction. Lastly, we derived exact functionals for the spin- and charge-contact interactions. Including these interactions results in a consistent treatment of the Coulomb interaction and the magnetic dipole interaction up to second order in the relativistic expansion.

A. Perturbative Energy diagrams

A.1 Goldstone diagram evaluation rules

We will briefly summarize the Goldstone diagram evaluation rules in this section. The rules and a detailed derivation can be found for example in the book by Lindgren [107]. It is important to note that Goldstone diagrams are time-ordered, i.e. the vertical order of the interactions in the diagram matters. The evaluation rules for closed Goldstone diagrams are given by:

1. Label the diagram with “hole” (down-arrow) and “particle” indices. A line that starts and ends at the same interaction is labeled with a hole index.
2. Add a matrix element for every interaction. For single-particle interactions, use $\langle \mathrm{out}| - V |\mathrm{in}\rangle$, for two-particle interactions use $\langle \text{left-out}, \text{right-out}| - V |\text{left-in}, \text{right-in}\rangle$
3. Draw a virtual line between two neighboring interactions. Add an energy denominator equal to $\sum_{\text{holes}} \epsilon_\alpha - \sum_{\text{particles}} \epsilon_i$, where the sum runs over all particles and holes crossed by the virtual line.
4. Sum over all hole and particle lines. Holes are summed over all energies smaller than the Fermi energy, particles are summed over all energies bigger than the Fermi energy.
5. Add a prefactor of $(-1)^{h+l}$, where h is the number of hole lines and l is the number of closed loops of orbital lines.
6. An overall factor 1/2 for each two-particle interaction and an equivalence factor equal to the number of equivalent diagrams represented by the diagram.
7. An overall factor 1/2 for each symmetry operation, such as reflection in a vertical plane or interchange of vertices of an interaction which transforms the diagram into itself or any other diagram appearing in the expansion.

Bibliography

[1] E. Beaurepaire, J.-C. Merle, A. Daunois, and J.-Y. Bigot. Ultrafast spin dynamics in ferromagnetic nickel. *Phys. Rev. Lett.*, 76:4250–4253, May 1996.

[2] J. Hohlfeld, E. Matthias, R. Knorren, and K. H. Bennemann. Nonequilibrium magnetization dynamics of nickel. *Phys. Rev. Lett.*, 78:4861–4864, Jun 1997.

[3] M. Aeschlimann, M. Bauer, S. Pawlik, W. Weber, R. Burgermeister, D. Oberli, and H. C. Siegmann. Ultrafast spin-dependent electron dynamics in fcc Co. *Phys. Rev. Lett.*, 79:5158–5161, Dec 1997.

[4] S. S. P. Parkin, M. Hayashi, and L. Thomas. Magnetic domain-wall racetrack memory. *Science*, 320(5873):190–194, 2008.

[5] T. L. Gilbert. A lagrangian formulation of the gyromagnetic equation of the magnetization field. *Phys. Rev.*, 100:1243, 1955.

[6] K. Krieger, J. K. Dewhurst, P. Elliott, S. Sharma, and E. K. U. Gross. Laser-induced demagnetization at ultrashort time scales: Predictions of TDDFT. *Journal of Chemical Theory and Computation*, 11(10):4870–4874, Oct 2015.

[7] E. Engel and R. M. Dreizler. *Density Functional Theory: An Advanced Course (Theoretical and Mathematical Physics).* Springer, 2011.

[8] P. Hohenberg and W. Kohn. Inhomogeneous electron gas. *Phys. Rev.*, 136:B864–B871, Nov 1964.

[9] W. Kohn. *Highlights of condensed-matter theory (Proceedings of the International School of Physics "Enrico Fermi").* 1985.

[10] R. M. Dreizler and E.K.U. Groß. *Density Functional Theory.* Springer Berlin Heidelberg, 2013.

[11] U. von Barth and L. Hedin. A local exchange-correlation potential for the spin polarized case. i. *Journal of Physics C: Solid State Physics*, 5(13):1629–1642, Jul 1972.

[12] G. Vignale and M. Rasolt. Current- and spin-density-functional theory for inhomogeneous electronic systems in strong magnetic fields. *Phys. Rev. B*, 37:10685–10696, Jun 1988.

[13] G. Vignale and W. Kohn. Current-dependent exchange-correlation potential for dynamical linear response theory. *Phys. Rev. Lett.*, 77:2037–2040, Sep 1996.

[14] J. A. Berger, P. Romaniello, R. van Leeuwen, and P. L. de Boeij. Performance of the Vignale-Kohn functional in the linear response of metals. *Phys. Rev. B*, 74:245117, Dec 2006.

[15] J. A. Berger, P. L. de Boeij, and R. van Leeuwen. Analysis of the vignale-kohn current functional in the calculation of the optical spectra of semiconductors. *Phys. Rev. B*, 75:035116, Jan 2007.

[16] J. P. Perdew and A. Zunger. Self-interaction correction to density-functional approximations for many-electron systems. *Phys. Rev. B*, 23:5048–5079, May 1981.

[17] D. M. Ceperley and B. J. Alder. Ground state of the electron gas by a stochastic method. *Phys. Rev. Lett.*, 45:566–569, Aug 1980.

[18] J. P. Perdew, K. Burke, and M. Ernzerhof. Generalized gradient approximation made simple. *Phys. Rev. Lett.*, 77:3865–3868, Oct 1996.

[19] J. Sun, A. Ruzsinszky, and J. P. Perdew. Strongly constrained and appropriately normed semilocal density functional. *Phys. Rev. Lett.*, 115:036402, Jul 2015.

[20] M. Gell-Mann and K. A. Brueckner. Correlation energy of an electron gas at high density. *Phys. Rev.*, 106:364–368, Apr 1957.

[21] E. Wigner. On the interaction of electrons in metals. *Phys. Rev.*, 46:1002–1011, Dec 1934.

[22] J. P. Perdew and Y. Wang. Accurate and simple analytic representation of the electron-gas correlation energy. *Phys. Rev. B*, 45:13244–13249, Jun 1992.

[23] G. Ortiz and P. Ballone. Correlation energy, structure factor, radial distribution function, and momentum distribution of the spin-polarized uniform electron gas. *Phys. Rev. B*, 50:1391–1405, Jul 1994.

[24] J. Kübler, K.-H. Höck, J. Sticht, and A. R. Williams. Local spin-density functional theory of noncollinear magnetism (invited). *Journal of Applied Physics*, 63(8):3482–3486, 1988.

[25] C. Ullrich. *Time-Dependent Density-Functional Theory: Concepts and Applications (Oxford Graduate Texts).* Oxford University Press, 2012.

[26] E. Runge and E. K. U. Gross. Density-functional theory for time-dependent systems. *Phys. Rev. Lett.*, 52:997–1000, Mar 1984.

[27] R. van Leeuwen. Mapping from densities to potentials in time-dependent density-functional theory. *Phys. Rev. Lett.*, 82:3863–3866, May 1999.

[28] R. van Leeuwen. Causality and symmetry in time-dependent density-functional theory. *Phys. Rev. Lett.*, 80:1280–1283, Feb 1998.

[29] K. Capelle, G. Vignale, and B. L. Györffy. Spin currents and spin dynamics in time-dependent density-functional theory. *Phys. Rev. Lett.*, 87:206403, Oct 2001.

[30] S. K. Ghosh and A. K. Dhara. Density-functional theory of many-electron systems subjected to time-dependent electric and magnetic fields. *Phys. Rev. A*, 38:1149–1158, Aug 1988.

[31] G. Vignale. Mapping from current densities to vector potentials in time-dependent current density functional theory. *Phys. Rev. B*, 70:201102, Nov 2004.

[32] M. A. L. Marques, N. T. Maitra, F. M. S. Nogueira, E. K. U. Gross, and A. Rubio. *Fundamentals of Time-Dependent Density Functional Theory (Lecture Notes in Physics, Vol. 837).* Springer, 2012.

[33] A. K. Rajagopal and J. Callaway. Inhomogeneous electron gas. *Phys. Rev. B*, 7:1912–1919, Mar 1973.

[34] A. K. Rajagopal. Inhomogeneous relativistic electron gas. *Journal of Physics C: Solid State Physics*, 11(24):L943–L948, dec 1978.

[35] A. H. MacDonald and S. H. Vosko. A relativistic density functional formalism. *Journal of Physics C: Solid State Physics*, 12(15):2977–2990, Aug 1979.

[36] T. Itoh. Derivation of Nonrelativistic Hamiltonian for Electrons from Quantum Electrodynamics. *Reviews of Modern Physics*, 37(1):159–165, Jan 1965.

[37] E. Parker. An apparent paradox concerning the field of an ideal dipole. *European Journal of Physics*, 38(2):025205, Jan 2017.

[38] “The Elk FP-LAPW Code”. http://elk.sourceforge.net/.

[39] E. Sjöstedt, L. Nordström, and D. J. Singh. An alternative way of linearizing the augmented plane-wave method. *Solid State Communications*, 114(1):15–20, 2000.

[40] D. Singh. *Planewaves, pseudopotentials, and the LAPW method.* Springer, 2006.

[41] D. D. Koelling and B. N. Harmon. A technique for relativistic spin-polarised calculations. *Journal of Physics C: Solid State Physics*, 10(16):3107–3114, Aug 1977.

[42] B. Koopmans, J. J. M. Ruigrok, F. Dalla Longa, and W. J. M. de Jonge. Unifying ultrafast magnetization dynamics. *Phys. Rev. Lett.*, 95:267207, Dec 2005.

[43] B. Koopmans, G. Malinowski, F. Dalla Longa, D. Steiauf, M. Fähnle, T. Roth, M. Cinchetti, and M. Aeschlimann. Explaining the paradoxical diversity of ultrafast laser-induced demagnetization. *Nature Materials*, 9:259 EP –, Dec 2009. Article.

[44] G. P. Zhang and W. Hübner. Laser-induced ultrafast demagnetization in ferromagnetic metals. *Phys. Rev. Lett.*, 85:3025–3028, Oct 2000.

[45] D. Steiauf and M. Fähnle. Elliott-yafet mechanism and the discussion of femtosecond magnetization dynamics. *Phys. Rev. B*, 79:140401, Apr 2009.

[46] M. Battiato, K. Carva, and P. M. Oppeneer. Superdiffusive spin transport as a mechanism of ultrafast demagnetization. *Phys. Rev. Lett.*, 105:027203, Jul 2010.

[47] A. M. Weiner. Femtosecond pulse shaping using spatial light modulators. *Review of Scientific Instruments*, 71(5):1929–1960, 2000.

[48] S. Sugano. *Magneto-Optics.* Springer Berlin Heidelberg, 2000.

[49] P. S. Pershan. Magneto-optical effects. *Journal of Applied Physics*, 38(3):1482–1490, 1967.

[50] Ru-Pin Pan, H. D. Wei, and Y. R. Shen. Optical second-harmonic generation from magnetized surfaces. *Phys. Rev. B*, 39:1229–1234, Jan 1989.

[51] T. Rasing. Nonlinear magneto-optical probing of magnetic interfaces. *Applied Physics B*, 68(3):477–484, Mar 1999.

[52] P. Elliott, T. Müller, J. K. Dewhurst, S. Sharma, and E. K. U. Gross. Ultrafast laser induced local magnetization dynamics in heusler compounds. *Scientific Reports*, 6:38911 EP –, Dec 2016. Article.

[53] K. Krieger, P. Elliott, T. Müller, N. Singh, J. K. Dewhurst, E. K. U. Gross, and S. Sharma. Ultrafast demagnetization in bulk versus thin films: an ab-initio study. *Journal of Physics: Condensed Matter*, 29(22):224001, Apr 2017.

[54] K. Krieger. *Spin-dynamics in strongly excited ferromagnetic systems.* PhD thesis, Martin-Luther-Universität Halle-Wittenberg, 2016.

[55] J. J. Sakurai. *Advanced quantum mechanics.* Addison-Wesley Pub. Co, 1967.

[56] A. Ludwig, J. Maurer, B. W. Mayer, C. R. Phillips, L. Gallmann, and U. Keller. Breakdown of the dipole approximation in strong-field ionization. *Phys. Rev. Lett.*, 113:243001, Dec 2014.

[57] J. D. Jackson. *Classical Electrodynamics Third Edition.* Wiley, 1998.

[58] J. K. Dewhurst, K. Krieger, S. Sharma, and E. K. U. Gross. An efficient algorithm for time propagation as applied to linearized augmented plane wave method. *Computer Physics Communications*, 209:92 – 95, 2016.

[59] V. Shokeen, M. S. Sanchez Piaia, J.-Y. Bigot, T. Müller, P. Elliott, J. K. Dewhurst, S. Sharma, and E. K. U. Gross. Spin flips versus spin transport in nonthermal electrons excited by ultrashort optical pulses in transition metals. *Phys. Rev. Lett.*, 119:107203, Sep 2017.

[60] A. J. Schellekens, W. Verhoeven, T. N. Vader, and B. Koopmans. Investigating the contribution of superdiffusive transport to ultrafast demagnetization of ferromagnetic thin films. *Applied Physics Letters*, 102(25):252408, 2013.

[61] J. Chen, U. Bovensiepen, A. Eschenlohr, T. Müller, P. Elliott, E. K. U. Gross, J. K. Dewhurst, and S. Sharma. Competing spin transfer and dissipation at Co/Cu(001) interfaces on femtosecond timescales. *Phys. Rev. Lett.*, 122:067202, Feb 2019.

[62] J. Güdde, U. Conrad, V. Jähnke, J. Hohlfeld, and E. Matthias. Magnetization dynamics of Ni and Co films on Cu(001) and of bulk nickel surfaces. *Phys. Rev. B*, 59:R6608–R6611, Mar 1999.

[63] U. Conrad, J. Güdde, V. Jähnke, and E. Matthias. Phase effects in magnetic second-harmonic generation on ultrathin Co and Ni films on Cu(001). *Phys. Rev. B*, 63:144417, Mar 2001.

[64] J. Chen, J. Wieczorek, A. Eschenlohr, S. Xiao, A. Tarasevitch, and U. Bovensiepen. Ultrafast inhomogeneous magnetization dynamics analyzed by interface-sensitive nonlinear magneto-optics. *Applied Physics Letters*, 110(9):092407, 2017.

[65] W. Töws and G. M. Pastor. Many-body theory of ultrafast demagnetization and angular momentum transfer in ferromagnetic transition metals. *Phys. Rev. Lett.*, 115:217204, Nov 2015.

[66] A. Nilsson, J. Stöhr, T. Wiell, M. Aldén, P. Bennich, N. Wassdahl, M. G. Samant, S. S. P. Parkin, N. Mårtensson, J. Nordgren, B. Johansson, and H. L. Skriver. Determination of the electronic density of states near buried interfaces: Application to Co/Cu multilayers. *Phys. Rev. B*, 54:2917–2921, Jul 1996.

[67] W. L. Ling, E. Rotenberg, H. J. Choi, J. H. Wolfe, F. Toyama, S. Paik, N. V. Smith, and Z. Q. Qiu. Double quantum well states in Cu/Co/Cu grown on Co(001). *Phys. Rev. B*, 65:113406, Feb 2002.

[68] J. K. Dewhurst, P. Elliott, S. Shallcross, E. K. U. Gross, and S. Sharma. Laser-induced intersite spin transfer. *Nano Letters*, 18(3):1842–1848, Mar 2018.

[69] J. K. Dewhurst, S. Shallcross, E. K. U. Gross, and S. Sharma. Substrate-controlled ultrafast spin injection and demagnetization. *Phys. Rev. Applied*, 10:044065, Oct 2018.

[70] C. Dornes, Y. Acremann, M. Savoini, M. Kubli, M. J. Neugebauer, E. Abreu, L. Huber, G. Lantz, C. A. F. Vaz, H. Lemke, E. M. Bothschafter, M. Porer, V. Esposito, L. Rettig, M. Buzzi, A. Alberca, Y. W. Windsor, P. Beaud, U. Staub, D. Zhu, S. Song, J. M. Glownia, and S. L. Johnson. The ultrafast einstein-de haas effect. *Nature*, 565(7738):209–212, 2019.

[71] M. Wietstruk, A. Melnikov, C. Stamm, T. Kachel, N. Pontius, M. Sultan, C. Gahl, M. Weinelt, H. A. Dürr, and U. Bovensiepen. Hot-electron-driven enhancement of spin-lattice coupling in Gd and Tb $4f$ ferromagnets observed by femtosecond x-ray magnetic circular dichroism. *Phys. Rev. Lett.*, 106:127401, Mar 2011.

[72] Y. Zhou, Y. Saad, M. L. Tiago, and J. R. Chelikowsky. Self-consistent-field calculations using chebyshev-filtered subspace iteration. *Journal of Computational Physics*, 219(1):172 – 184, 2006.

[73] Y. Zhou, Y. Saad, M. L. Tiago, and J. R. Chelikowsky. Parallel self-consistent-field calculations via chebyshev-filtered subspace acceleration. *Phys. Rev. E*, 74:066704, Dec 2006.

[74] S. Goedecker. Linear scaling electronic structure methods. *Rev. Mod. Phys.*, 71:1085–1123, Jul 1999.

[75] C. Herring. *Magnetism: Exchange interactions among itinerant electrons.* Magnetism (Ed. G. Rado and H. Suhl). Academic Press, 1966.

[76] L. M. Sandratskii. Energy band structure calculations for crystals with spiral magnetic structure. *Physica Status Solidi (b)*, 136(1):167–180, 1986.

[77] T. Müller, S. Sharma, E. K. U. Gross, and J. K. Dewhurst. Extending solid-state calculations to ultra long-range length scales. *Phys. Rev. Lett.*, Accepted, 2020.

[78] M. Weinert. Solution of poisson's equation: Beyond Ewald-type methods. *Journal of Mathematical Physics*, 22(11):2433–2439, 1981.

[79] K. Fan and A. J. Hoffman. *Some Metric Inequalities in the Space of Matrices*, pages 121–126. 2003.

[80] E. Sjöstedt and L. Nordström. Noncollinear full-potential studies of $\gamma-$Fe. *Phys. Rev. B*, 66:014447, Jul 2002.

[81] L. M. Corliss, J. M. Hastings, and R. J. Weiss. Antiphase antiferromagnetic structure of chromium. *Phys. Rev. Lett.*, 3:211–212, Sep 1959.

[82] V. N. Bykov, V. S. Golovkin, N. V. Ageev, V. A. Levdik, and S. I. Vinogradov. The Magnetic Structure of Chromium. *Soviet Physics Doklady*, 4:1070, March 1960.

[83] A. W. Overhauser. Spin density waves in an electron gas. *Phys. Rev.*, 128:1437–1452, Nov 1962.

[84] V.L. Moruzzi, J.F. Janak, and A.R. Williams. *Calculated Electronic Properties of Metals.* Pergamon, 1978.

[85] J. Kübler. Spin-density functional calculations for chromium. *Journal of Magnetism and Magnetic Materials*, 20(3):277 – 284, 1980.

[86] H. L. Skriver. The electronic structure of antiferromagnetic chromium. *Journal of Physics F: Metal Physics*, 11:97, Nov 1981.

[87] N. I. Kulikov and E. Kulatov. Self-consistent band structure calculation of chromium: Pressure influence. *Journal of Physics F: Metal Physics*, 12:2291, Nov 1082.

[88] N. I. Kulikov, M. Alouani, M. A. Khan, and M. V. Magnitskaya. Self-energy corrections to the ab initio band structure: Chromium. *Phys. Rev. B*, 36:929–938, Jul 1987.

[89] J. Chen, D. Singh, and H. Krakauer. Local-density description of antiferromagnetic Cr. *Phys. Rev. B*, 38:12834–12836, Dec 1988.

[90] V. L. Moruzzi and P. M. Marcus. Antiferromagnetic ground state of bcc chromium. *Phys. Rev. B*, 46:3171–3174, Aug 1992.

[91] D. J. Singh and J. Ashkenazi. Magnetism with generalized-gradient-approximation density functionals. *Phys. Rev. B*, 46:11570–11577, Nov 1992.

[92] K. Hirai. Magnetism in spin-density-wave chromium from first-principles calculation. *Journal of the Physical Society of Japan*, 66(3):560–563, 1997.

[93] G. Y. Guo and H. H. Wang. Calculated elastic constants and electronic and magnetic properties of bcc, fcc, and hcp Cr crystals and thin films. *Phys. Rev. B*, 62:5136–5143, Aug 2000.

[94] G. Bihlmayer, T. Asada, and S. Blügel. Electronic and magnetic structure of the (001) surfaces of V, Cr, and V/Cr. *Phys. Rev. B*, 62:R11937–R11940, Nov 2000.

[95] J. Schäfer, E. Rotenberg, S.D. Kevan, and P. Blaha. Energy gap of the spin density wave at the Cr(110) surface. *Surface Science*, 454-456:885 – 890, 2000.

[96] R. Hafner, D. Spisák, R. Lorenz, and J. Hafner. Does density-functional theory predict a spin-density-wave ground state for Cr? *Journal of Physics: Condensed Matter*, 13:L239, Mar 2001.

[97] S. Cottenier, B. De Vries, J. Meersschaut, and M. Rots. What density-functional theory can tell us about the spin-density wave in Cr. *J. Phys.: Condens. Matter*, 14:3275–3283, Apr 2002.

[98] R. Hafner, D. Spišák, R. Lorenz, and J. Hafner. Magnetic ground state of Cr in density-functional theory. *Phys. Rev. B*, 65:184432, May 2002.

[99] C. Pellegrini, T. Müller, J. K. Dewhurst, S. Sharma, A. Sanna, and E. K. U. Gross. Density functional theory of magnetic dipolar interactions. *Phys. Rev. B*, 101:144401, Apr 2020.

[100] T. Lahaye, C. Menotti, L. Santos, M. Lewenstein, and T. Pfau. The physics of dipolar bosonic quantum gases. *Reports on Progress in Physics*, 72(12):126401, Nov 2009.

[101] C. Fiolhais, F. Nogueira, and M. Marques. *A Primer in Density Functional Theory (Lecture Notes in Physics) (v. 620)*. Springer, 2003.

[102] G. Giuliani and G. Vignale. *Quantum Theory of the Electron Liquid*. Cambridge University Press, 2005.

[103] E. Engel and S. H. Vosko. Wave-vector dependence of the exchange contribution to the electron-gas response functions: An analytic derivation. *Phys. Rev. B*, 42:4940–4953, Sep 1990.

[104] Z. Qian. Static dielectric function with exact exchange contribution in the electron liquid. *Journal of Mathematical Physics*, 56(11):111901, 2015.

[105] M. L. Glasser. Exchange corrections to the static Lindhard screening function. *Physical Review B*, 51(11):7283–7286, March 1995.

[106] W. Kutzelnigg. Origin and meaning of the fermi contact interaction. *Theoretica chimica acta*, 73(2):173–200, Mar 1988.

[107] I. Lindgren. *Atomic Many-Body Theory*. Springer Berlin Heidelberg, 1986.

List of Publications

Part of this thesis

Spin flips versus spin transport in nonthermal electrons excited by ultrashort optical pulses in transition metals, V. Shokeen, M. Sanchez Piaia, J.-Y. Bigot, T. Müller, P. Elliott, J. K. Dewhurst, S. Sharma, E. K. U. Gross
Phys. Rev. Lett. 119, 107203 (2017) (first author theory)

Competing spin transfer and dissipation at Co/Cu(001) interfaces on femtosecond timescales, J. Chen, U. Bovensiepen, A. Eschenlohr, T. Müller, P. Elliott, E. K. U. Gross, J. K. Dewhurst, S. Sharma
Phys. Rev. Lett. 122, 067202 (2019) (first author theory)

Density functional theory of magnetic dipolar interactions,
C. Pellegrini, T. Müller, S. Sharma, E. K. U. Gross, J. K. Dewhurst
Phys. Rev. B 101, 144401 (2020)

Extending solid-state calculations to ultra long-range length scales,
T. Müller, E. K. U. Gross, S. Sharma, J. K. Dewhurst
Phys. Rev. Lett, Accepted, (2020)

During the time at the Max-Planck-Institute

Ultrafast laser induced local magnetization dynamics in Heusler compounds,
P. Elliott, T. Müller, J. K. Dewhurst, S. Sharma, E. K. U. Gross
Sci. Rep. 6, 38911 (2016)

Ultrafast demagnetization in bulk versus thin films: an ab initio study,
K. Krieger, P. Elliott, T. Müller, N. Singh, J. K. Dewhurst, E. K. U. Gross, S. Sharma
J. Phys. Condens. Matter, Vol. 29, Num. 22 (2017)

Other publications

Intrinsic magnetization of antiferromagnetic textures,
E. G. Tveten, T. Müller, J. Linder, A. Brataas
Phys. Rev. B 93, 104408 (2016)

A micro-SQUID with dispersive readout for magnetic scanning microscopy,
F. Foroughi, J.-M. Mol, T. Müller, J. R. Kirtley, K. A. Moler, H. Bluhm
Appl. Phys. Lett. 112, 252601 (2018)

Acknowledgments

First of all, I would like to thank my advisor Hardy Gross for giving me the opportunity to write my PhD thesis at the MPI in Halle. Specifically, I thank him for a very nice working atmosphere, much scientific freedom and the opportunity to visit many highly interesting national and international conferences.
I would also like to thank Sangeeta Sharma and Kay Dewhurst. Sangeeta managed to acquire the initial funding for my (very well-funded) position and has helped me a lot with her detailed knowledge about ultrafast demagnetization. Kay was very helpful in the ultra long-range project. Besides helping with fundamental questions, he also had many good suggestions for optimizing and benchmarking the approach and the code.
I thank Peter Elliott for always being easy to talk to. He was always open for discussions about physics, even if the topic was unrelated to his work.
Of course I also want to thank our external experimental colleagues for fruitful collaborations. I want to thank Vishal Shokeen and Jean-Yves Bigot from Strasbourg. Jean-Yves Bigot sadly passed away in 2018, which is certainly a big loss for the ultrafast community. I also gratefully acknowledge our collaboration with Jinghao Chen, Andrea Eschenlohr and Uwe Bovensiepen from the University of Duisburg-Essen.
Finally I would like to thank the rest of the group for a friendly atmosphere. In particular I would like to thank Arkady Davidov and Eli Kraisler for a fun but also stimulating office.

Schließlich möchte ich meinen Eltern und meinem Bruder für den anhaltend guten Support in allen Belangen außerhalb der Physik danken, der meine Ausbildung bis hin zur Promotion erst ermöglicht hat.

Angaben zur Person und Ausbildung

Person

Vor-, Familienname:	Tristan Müller
Geburtsdatum, Ort:	07.08.1991, in Simmern/Hunsrück
Staatsangehörigkeit:	deutsch
Geschlecht:	männlich
Akademischer Grad:	M.Sc Physik
Fachgebiet der Promotion:	Physik

Ausbildung

11/2015 - 09/2019:	Doktorand am MPI für Mikrostrukturphysik, in der Gruppe von Prof. Eberhard K. U. Groß
09/2014 - 09/2015:	M.Sc. in Physik an der RWTH Aachen, Masterarbeit in der Gruppe von Prof. Hendrik Bluhm
08/2013 - 05/2014:	Erasmusstudent an der NTNU Trondheim
10/2010 - 08/2013:	B.Sc. in Physik an der RWTH Aachen, Bachelorarbeit in der Gruppe von Prof. Stefan Schael
08/2002 - 03/2010:	Herzog-Johann-Gymnasium Simmern

Eidesstattliche Erklärung

Hiermit erkläre ich gemäß §5 der Promotionsordnung der Naturwissenschaftlichen Fakultät II der Martin-Luther-Universität Halle-Wittenberg vom Juli 2016, dass ich die vorliegende Arbeit selbstständig und ohne fremde Hilfe verfasst habe. Ich habe keine anderen als die von mir angegebenen Quellen und Hilfsmittel verwendet und die den benutzen Werken wörtlich sowie inhaltlich entnommenen Stellen kenntlich gemacht. Ich habe keine vorherigen Promotionsversuche unternommen, weder an dieser noch an einer anderen Fakultät. Darüberhinaus bin ich nicht vorbestraft und es ist kein Ermittlungsverfahren gegen mich eingeleitet.

Halle (Saale),

gez. Tristan Müller